LBL-10957

Lawrence Berkeley Laboratory
UNIVERSITY OF CALIFORNIA

Presented at the Nuclear Physics Workshop, Tandar Project,
Comision Nacional de Energia Atomica, Argentina, April 7-18, 1980

NUCLEAR STRUCTURE AT HIGH ANGULAR MOMENTUM

F. S. Stephens

June 1980

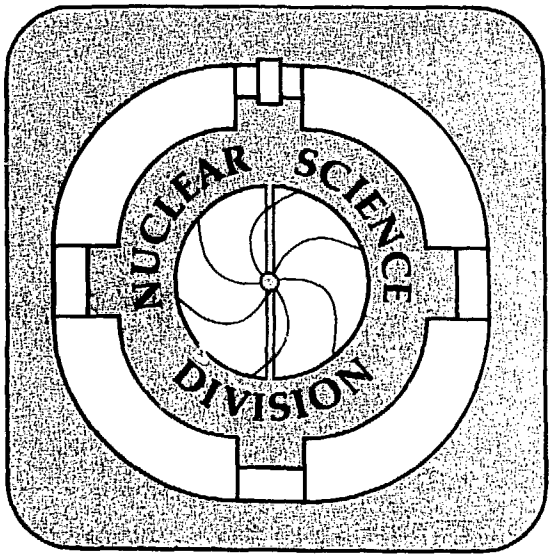

Prepared for the U.S. Department of Energy under Contract W-7405-ENG-48

NUCLEAR STRUCTURE AT HIGH ANGULAR MOMENTUM*

CONTENTS

* This work was supported by the Nuclear Science Division of the U. S. Department of Energy under contract No. W-7405-ENG-48.

NUCLEAR STRUCTURE AT HIGH ANGULAR MOMENTUM

F. S. Stephens

Nuclear Science Division
Lawrence Berkeley Laboratory
University of California
Berkeley, CA 94720

1. INTRODUCTION

Studies of nuclei at high angular momenta are popular just now. I believe this is because we are reaching some overview of the physics at very high spins, and I will try to describe this overview for you. The schecule, as written above, indicates that this will come in the second lecture, which means that this perspective can be compared against the emerging data which will be the subject of the last four lectures. Today I want to discuss first the limits we face in trying to get nuclei to hold very high angular momentum. I will then describe the method presently used for producing nuclei with the maximum angular momentum.

1.1. Angular Momentum Limits. The phrase "high angular momentum," as applied to nuclei can mean several things. In the very light nuclei it refers generally to the maximum angular momentum that can be generated by valence nucleons; for example, it would be arount 4ħ for the p-shell nucleus ^{7}Be, and 8ħ for the sd-shell nucleus ^{20}Ne. This limit exceeds 100ħ for nuclei around mass 170, and is effectively replaced by lower limits, most generally the instability against fission. Between these regions, for $40 \leq A \leq 100$, the highest angular momentum that can be conveniently studied is limited by what can survive the particle evaporation cascade that follows production of

the compound nucleus. The present lectures will be limited to the highest of these mass regions, $A \gtrsim 100$. Even with this limitation, "high angular momentum" is used at the present time to refer to two spin ranges: The highest spins accessible (~60ħ) or the highest spins that have been well studied (~20ħ). The latter of these ranges has been exciting, with the discovery of backbending and its subsequent interpretation in terms of band crossing (Johnson and Szymanski 1973; Sorensen 1973). Indeed, a spectroscopy of band crossings is currently developing, and will be discussed in the third lecture. The last three lectures will aim at considering the highest spins it is possible to study.

It is not possible to specify a maximum angular momentum for nuclei without specifying a time scale. For example, a target and projectile nucleus may be in contact momentarily with as much as 500ħ in the system. The way angular momentum is transferred into the internal degrees of freedom of the two nuclei is one of the fascinating aspects of deep-inelastic collisions, but such a system cannot fuse, and the angular momentum is largely returned to the external degrees of freedom as the system separates. In order to live longer than $\sim 10^{-20}$ sec, a system must have a non-vanishing barrier against fission, and the point at which this occurs can be readily estimated using the liquid-drop model (Bohr and Kalckar 1937). This model considers the nucleus as an incompressible fluid with volume, surface, Coulomb and rotational (based on the equilibrium shape) energies. Its success in giving average nuclear potential energies under various conditions has been

impressive from the earliest days of nuclear physics. The angular momentum for which the fission barrier vanishes has been calculated by Cohen, Plasil and Swiatecki (1974) and is shown as a function of mass number (along the line of β-stability), by the solid curve in Fig. 1. This represents the maximum angular momentum that a "cold" idealized nucleus could contain, and is about 100ħ for A ~ 130. It is lower both for higher mass numbers (because of the increasing Coulomb repulsion) and for lower mass numbers (because of the lower surface energy and the higher rotational frequencies required by the smaller moments of inertia).

If cold nuclei could be produced at these angular momenta, spectroscopic studies might be possible up to near this limit. But the heavy-ion fission reactions that bring in this much angular momentum also bring in of order 40 MeV of excitation energy (or more), greatly increasing the fission probability. In order to prevent fission (where most of the angular momentum goes into the relative motion of the fragments), another process must de-excite the nucleus, and at such excitation energies this can only be particle evaporation. The time scale for particle evaporation (at these excitation energies and for normal binding energies) is 10^{-17} to 10^{-18} sec, and in order to slow the fission down to such times, a fission barrier of the order of the neutron binding energy (~8 MeV) is required. The dashed line in Fig. 1 is a line corresponding to an 8 MeV fission barrier, below which particle evaporation should dominate. Between these lines, or in the time range 10^{-17}-10^{-21} sec, essentially

only fission of the system can be studied, and there is little information about this region. When the decreasing level density slows the particle evaporation sufficiently (~10^{-15} sec), or the excitation energy is below the neutron binding energy, γ-ray emission takes over and de-excitates the nucleus to its ground state. The angular momentum removed by the particle evaporation is small if neutrons or protons are evaporated (~1$\hbar$ per particle) but can be quite large (up to 20$\hbar$) for α-particles. An estimate of the maximum angular momentum surviving the particle evaporation has been made based on γ-ray and α-particle emission probabilities, and is shown as the dotted line in Fig. 1. Between the dashed and dotted lines (10^{-17}-10^{-15} sec) the states can be studied by means of the evaporated particles--a method more sensitive to the nuclear structure than fission, but much less sensitive than γ-ray decay. The present lectures will cover only the γ-ray studies of high angular momentum studies, which have access to the region below the dotted line in Fig. 1. It is easy to understand why these sutdies have centered first around the region A ~ 140, where spins up to ~70$\hbar$ are accessible.

1.2. Production of High-Spin States. The method used for producing "high-spin states" depends on what kind of high-spin states is meant. In the light elements one would probably choose a transfer reaction with an appropriately high ℓ-window. In the spin 20-30$\hbar$ region of the heavier elements considered here (A > 100), Coulomb excitation would be an extremely important method. However, the present interest is centered on the very highest spins, 60-70$\hbar$, and only the heavy-ion

fusion reactions have been used to study such states. it is not out of the question that other methods could be found. The deep inelastic collisions can populate such spins, but so far the information flow has been the other way--our knowledge of high-spin states has been used to estimate the angular momentum transfers in these collisions. The present discussion will, therefore, deal only with heavy-ion fusion reactions.

The idea that a target and projectile nucleus fuse to form a compound system, whose subsequent decay is independent of its formation, goes back to Niels Bohr (1936). Independent decay means that the system remembers nothing of the entrance channel, except that required by conservation laws, notably here, angular momentum. No evidence contrary to this idea has been found, though we now know that "composite" systems can be formed which, for various reasons, live for a much shorter time than the compound systems ($\sim 10^{-17}$–10^{-18} sec), and consequently remember more about the entrance channel. In this section the formation and decay of the compound system will be discussed, not in depth, but rather to understand how angular momentum gets into and out of such a system.

An essential feature of heavy-ion collisions, for the present purposes, is that they are quite classical. The heavy-ion wave lengths are considerably smaller than the dimensions of the colliding systems. Thus, considering the nuclei as charged black spheres:

$$\sigma_R = \pi(R_1 + R_2)^2(1 - E_{CB}/E_{CM}) = \pi\lambda\!\!\!^{-2}\ell_{max}(\ell + 1) \quad , \qquad (1)$$

where σ_R is the reaction across section, R_1 and R_2 the target and projectile radii, E_{CM} the center-of-mass bombarding energy, E_{CB} the Coulomb barrier height, $\lambda\!\!\!^{-}$ the de-Broglie wavelength in the center-of-mass system, and ℓ_{max} the maximum angular momentum leading to a reaction. From Eq. (1), ℓ_{max} can be evaluated to be:

$$\ell_{max} = 0.219(R_1 + R_2)[\mu(E_{CM} - E_{CB})]^{1/2} \quad , \tag{2}$$

with R_1 and R_2 in femtometers, μ is the reduced mass in mass units, and E_{CM} and E_{CB} are in MeV. The more distant collisions, involving the highest ℓ-waves, lead to transfer reactions and deep inelastic collisions, so that the evaporation residue cross section, σ_{er}, is given by the right side of Eq. (1), but with a lower ℓ-value, ℓ_{er}, replacing ℓ_{max}. Thus a measured fusion cross section implies an ℓ_{er} given as:

$$\ell_{er}^2 = 1.5\ \sigma_{er}\mu E_{CM} \quad , \tag{3}$$

where σ_{er} is in barns and the other units are as above. These equations are approximate and fail for high projectile velocities ($E_{CM}/E_{CB} > 2$) and, of course, for angular momenta in excess of that which the compound system can hold. Nevertheless, they are excellent for orientation, and Eq. (2) shows, for example, that 200 MeV ^{40}Ar projectiles on a ^{124}Sn target involve angular momenta up to 96$\hbar$, more than the $^{164}Er^*$ compound nucleus can hold. The distribution of angular momenta is given by:

$$\sigma(\ell) = \pi\lambda^2(2\ell + 1)\, T_\ell \quad , \tag{4}$$

where T_ℓ is a transmission coefficient; that for the black sphere (or "sharp cut-off" model) is unity up to ℓ_{max} and zero above that. This gives the familiar "triangular" distribution of cross section with ℓ, where, fortunately, the larger angular momenta have the greater cross section. Nevertheless, this is a broad spin distribution, and we are trying many different ways to isolate narrower regions of very high spins.

The results from a statistical model calculation for the decay of an evaporation residue are shown in Fig. 2 (Hillis, et al., 1979). The system is 147 MeV ^{40}Ar projectiles and a ^{124}Sn target to give $^{164}Er^*$ as the compound nucleus. The initial excitation energy and angular momentum distribution are shown at the top of Fig. 2 and the contour lines on the main excitation energy vs angular momentum plot show the region populated following each neutron evaporation. After the third neutron evaporation, part of the population is left to γ decay (shaded) and part goes on to emit a fourth neutron (white). This repeats for the fourth neutron, producing a small cross section for emitting five neutrons. There is a reasonably clear line about one neutron binding energy above the yrast line, separating the γ-emitting region from the particle-evaporation region. Two types of correlation are shown in the side and bottom plots. The side one shows that the total γ-ray energy is correlated with the reaction channel, higher total energies being associated with fewer neutrons

evaporated. The bottom plot shows that higher angular momenta are also associated with fewer neutrons evaporated, often referred to as a "fractionation" of angular momentum among the products. It is apparent from these plots, or the main E vs I plot, that higher total γ-ray energies are associated with higher spin values. These correlations all come about because the energy that is tied up carrying the angular momentum of the system is not available for evaporating neutrons, but later appears as γ-ray energy. All these correlations are used in studies of very high angular momentum in such nuclei.

The remainder of the lectures will be devoted to studies of γ-rays de-exciting the evaporation residues from heavy-ion reactions. The present discussion is aimed only at introducing the general pattern of this de-excitation. The previous discussion has established that the γ decay occurs in the region between the yrast line* and a line roughly one neutron binding energy above it. This region is illustrated in Fig. 3, and the decay path is sketched for four different spin inputs. Two types of γ-rays occur: those that cool the nucleus to or toward the yrast line, called "statistical;" and those that are more or less parallel to the yrast line and remove the angular momentum, called "yrast-like." At each point there is a competition between these two types. The statistical γ-rays depend only on average matrix

*The yrast line traces out the lowest energy level in the nucleus for each spin value.

elements and level densities, and will be discussed somewhat more in a few moments. The yrast-like γ-rays can be collective or not, and are the main subject of these lectures. The competition between these types depends on the excitation energy, which affects the level densities, and also on the degree of collectivity, which produces faster (enhanced) yrast-like transitions.

There is another division for the γ-rays, into those that are resolved in the spectrum and those that are not. In order to be resolved, a transition must have a sufficiently large population (as a rough estimate, one percent), and this is not generally the case for the higher excitation energies since there are thousands of possible pathways. Only up to spins 20 or 30$\hbar$ (heavy arrows in Fig. 3) does enough population collect in the yrast or near-yrast states, to produce resolved lines. In just two or three cases this has gone as high as 36 or 37$\hbar$, and these will be discussed in Lecture 4. For the higher spin transitions, and for all the statistical transitions one must work with unresolved, or "continuum" spectra. The many techniques being developed for this purpose are discussed in Lectures 5 and 6.

The shape of the statistical component of the emitted γ-rays may be approximated by an expression of the form:

$$N_\gamma \propto E_\gamma^n e^{-E_\gamma/T} \quad , \tag{5}$$

where n and T are constants to be fixed by the spectrum above the edge of the yrast bump. Generally n is around 2 (though theoretical estimates would be nearer 4) and T is around 1 MeV. These transitions are probably mostly E1 and there are about 4 per cascade. Their angular distribution is essentially isotropic. It appears that the statistical γ-rays do not give much information about the structure of very high spin states, but rather represent a background against which we must look for that information.

A final problem in conection with the production of very high spin states has to do with the region of the periodic chart where they can be made. Consider proton and neutron evaporation from nuclei with A ~ 150 around the region of β-stability where the binding energies are about the same. Then for similar final product nuclei, the excitation energy would be ~8 MeV lower for proton evaporation due to its Coulomb barrier. This has such a large effect on the level density that only neutrons are evaporated. On the other hand, as one moves off the line of β-stability toward the neutron-deficient side, the neutron binding energy goes up and the proton (and alpha) binding energy goes down until with about 15 percent fewer neutrons, the neutron binding energy is equal to the proton binding energy plus its Coulomb barrier. At this point neutrons and protons are evaporated with equal probability, and if one goes further neutron deficient, protons are preferentially evaporated, driving the system back toward the equal probability line. Since it is not possible to make neutron excess nuclei in heavy-ion fusion reactions (no sufficiently

neutron-rich targets and/or projectiles exist) the accessible region is from the β-stability line to a line having about 15 percent fewer neutrons. Alpha binding energies vary with neutron number like those for protons, so that by producing nuclei as neutron rich as possible, evaporation of both can be essentially completely avoided, conserving the angular momentum and reducing the number of open channels. These reactions, the so called HI,xn reactions, are currently the best method for producing states of the highest angular momentum.

2. PHYSICS OF HIGH SPIN STATES

Nuclei are composed of a small (but not too small) number of nucleons. As a result of this they display both collective and single-particle (non-collective) features. In the rare-earth and actinide regions, the low-lying rotational bands represent an almost pure collective motion, with energies following the $I(I + 1)$ rotor formula to within a percent or two, and E2 transition probabilities nearly 200 times larger than a single proton would have. On the other hand, near the closed shells the energy levels are almost completely determined by the motion of a single nucleon. Most nuclear levels display both collective and non-collective features, and high-spin states are no exception. To approach the physics of these states I will first describe some properties of a purely collective, classical rotor, and then consider the effects of coupling single particle motion to this. Our ideas about high spin states have undergone important developments recently that now make possible a reasonably simple description of this subject, which I will try to describe in this lecture.

The collective limit is one we must understand, and the basic nuclear system here has been found to be an axially symmetric rotor with quadrupole deformation. For a more complete discussion of this subject see Bohr and Mottelson (1975). Such a system with two equivalent axes 1,2 about which it can rotate has a Hamiltonian of the form:

$$H_{rot} = \frac{h^2}{2\mathcal{J}} (I_1^2 + I_2^2) \quad , \tag{6}$$

where $\mathcal{J}_1 = \mathcal{J}_2 \equiv \mathcal{J}$ is a moment of inertia that is taken here to be constant, but whose value depends on the internal structure of the system. The energy of a rotor of this type can be expressed either in terms of the angular momentum:

$$E_{rot}(I) = \frac{h^2}{2\mathcal{J}} I(I + 1) \quad , \tag{7}$$

or in terms of the rotational frequency, ω:

$$E_{rot}(\omega) = \frac{1}{2}\mathcal{J}\omega^2 \tag{8}$$

Deviation from rigid-rotor behavior can be expressed as an expansion either in $I(I + 1)$, or in ω^2; the latter generally converges better. The relationship between these is just:

$$\mathcal{J}\omega = \hbar[I(I + 1)]^{1/2} \tag{9}$$

To relate ω to rotational transition energy, E_γ, we have:

$$\hbar\omega \approx \frac{\partial E_{rot}}{\partial I} \approx 1/2[E_{rot}(I + 1) - E_{rot}(I - 1)] = E_\gamma/2 \tag{10}$$

where the right side is specifically for the collective stretched $(I + 1 \rightarrow I - 1)$ quadrupole transitions. This last relationship, that

the rotational frequency is about one-half the γ-ray transition energy, is often used because the transition energy is a readily measured quantity. It can also be related to the angular momentum:

$$E_\gamma = \frac{\hbar^2}{2\mathcal{J}}(4I - 2) \quad . \tag{11}$$

These relationships are for perfect rotors; whereas in real nuclei the moment of inertia is not completely constant, introducing complications to all these expressions.

The moment of inertia of a classical rotor depends on both the shape and the flow pattern, the latter of which is expected to be rigid in nuclei at high spins. The pairing correlations modify this significantly at low spins values, but should be completely quenched by spins of 30ħ or so. The shape of a rigid ellipsoid can be expressed in terms of the parameters, σ and γ, defined so that the semi-axes r_i are related to the mean radius R by; $r_i = a_i R$, where:

$$\begin{aligned} a_1 &= e^{\sigma\cos\left(\gamma - \frac{2\pi}{3}\right)} \\ a_2 &= e^{\sigma\cos\left(\gamma + \frac{2\pi}{3}\right)} \\ a_3 &= e^{\sigma\cos\gamma} \quad . \end{aligned} \tag{12}$$

For small deformation this gives $\Delta R/R \approx \varepsilon \approx 1.5\sigma$ and $\beta \approx 1.6\sigma$. Such an ellipsoid has moment of inertia:

$$\mathcal{I}_1 = \frac{1}{5} M\left(r_2^2 + r_3^2\right) = \frac{1}{2}\left(a_2^2 + a_3^2\right)\mathcal{I}_0 \quad , \tag{13}$$

where $\mathcal{I}_0$ is the rigid sphere value, and the axes may be permuted cyclically. Values of $\mathcal{I}_0$ can be obtained from the expression for a rigid sphere given by Myers (1973). From the equivalent sharp radius for the matter distribution (Blocki, et al., 1977):

$$R_s = 1.28\ A^{1/3} - 0.76 + 0.8\ A^{-1/3}\ \text{fm} \quad ; \tag{14}$$

the value for a sphere is:

$$\frac{2\mathcal{I}_0}{\hbar^2} = \frac{4MR_s^2}{5\hbar^2} = 0.01913\ A\ R_s^2(\text{fm}) \quad \text{MeV}^{-1} \quad . \tag{15}$$

The effect of a diffuse surface can be added simply by:

$$\mathcal{I}_{\text{diff}} = \mathcal{I}_{\text{sharp}} + 2Mb^2 \quad , \tag{16}$$

where b is the width of the diffuse region, normally around 1 fm. For orientation one can use the simpler expression:

$$R = 1.16\ A^{1/3}\ \text{fm} \quad , \tag{17}$$

which leads to:

$$\frac{\hbar^2}{2\Im_0} = 36\ A^{-5/3} \quad \text{MeV} \quad . \tag{18}$$

For an oblate ($\gamma = 60^\circ$) or a prolate ($\gamma = 0^\circ$) shape, rotating around the symmetry axis, $\parallel$, or perpendicular to it, $\perp$, the lowest order expansions of Eq. (13) are illustrated in Fig. 4. Triaxial shapes will fall between these limits, and for this reason are not considered explicitly here. These expansions begin to deviate significantly from the exact expressions around $\beta = 0.3$, and for β values near 0.8, the exact P-$\perp$ moment of inertia becomes larger than the O-$\parallel$ one, in contrast to the situation shown in Fig. 4. It is interesting that the liquid-drop shapes of minimum energy as a function of spin reflect this behavior, being moderately deformed and oblate through most of the spin range and becoming prolate in the A = 150 region when β reaches values around 0.8, just prior to fission. The energy trajectories based on these four cases of classical rigid rotation and Eq. (7) are shown in the right part of Fig. 4 for $\beta = 0.3$. The lowest energies are for an oblate shape rotating about the symmetry axis, corresponding to its largest moment of inertia. The earth is oblate for precisely this season; however, real rotating nuclei are generally not oblate due to the shell effects, as will be discussed shortly.

For systems where the quantal aspects are important, the preceeding discussion has to be clarified, since these systems cannot rotate collectively about a symmetry axis—there is no way to orient them with

respect to such an axis. It was understood for some time that this meant these degrees of freedom were contained in the single-particle motion. However, when Bohr and Mottelson (1975) considered aligning particle angular momentum along a symmetry axis, they realized that on the average the energy was the same as rotating the system classically about that axis. They have strictly shown this only in the Fermi gas approximation, but it is generally believed to be true, or approximately so, for realistic nuclear systems. Particle angular momenta aligned along a nuclear symmetry axis are then viewed as an effective rotation of the system about that axis. Thus the trajectories sketched in the right part of Fig. 4 all have meaning for nuclei; the solid ones are true collective rotations, having smooth energies and strongly enhanced E2 transition probabilities, whereas the dashed lines are the average location of irregularly spaced states having single-particle character. Both features of the latter-type states suggest that isomers should be reasonably probable, and these expectations have led to a number of searches for them, as discussed in Lecture 4.

To this picture the microscopic aspects of nuclear structure must be added. Nuclear levels in a potential well are grouped together into shells in very much the same way electrons are in an atom. Certain nucleon numbers ("magic numbers") complete shells and have extra stability in a analogy to the noble gas electronic structures. However, when nuclei deform, the shells change, so that the number to complete a shell is different. Thus, in general, a given nucleon number will prefer that shape which makes it look most nearly like a

closed shell. These "shell effects" can be as large as 10-12 MeV (the double closed spherical shell at ^{208}Pb), but on the average might be 3-4 MeV. Comparing with the right side of Fig. 4, it is apparent that 3-4 MeV is larger than the full spread of liquid-drop shapes up to $I \approx 30$. Thus below this spin (for $A \sim 160$) the nuclear shape is determined mainly by shell effects. Around $I = 60$, however, the spread in Fig. 4 is ~10 MeV, considerably larger than the normal shell effects, so that here one expects only oblate shapes rotating around the symmetry axis (non-collective behavior with isomers) or prolate shapes rotating collectively (smooth bands and no isomers). Since these behaviors appear quite different experimentally, there is hope to learn about the shapes and dynamics of nuclei at these spin values. Neither the exact evaluation of Eq. (13) nor the consideration of larger deformations changes this pattern. The P-$\perp$ and O-$\parallel$ shapes become closer in energy with increasing deformation, and even cross, but they remain well separated from the other types.

In order to understand how single-particle and collective motion might be combined in nuclear states at high spins, I will start with a collective rotational nucleus, and couple to this first one and then more single particles. The rotational angular momentum is necessarily perpendicular to the nuclear symmetry axis (or discussed above) and the particle angular momentum j, can couple either along the symmetry axis as illustrated in the top part of Fig. 5, or along the rotation axis as in the bottom part of Fig. 5. The former situation is that

considered by Bohr (1952) and the projection of j along the symmetry axis is a constant of the motion called Ω. In this case the collective angular momentum, R, and the projection of j along the rotation axis are not constants of the motion. In the lower part of Fig. 5, the projection of j along the rotation axis, called α (or i), is sharp, and here R and Ω are not constants of the motion. It seems rather clear that a perpendicular relationship between R and j will be much less favorable for producing low-energy high-spin states than a parallel one. This is borne out by the fact that as the nucleus rotates there is a Coriolis force which tends to align j with the rotation axis. The backbending phenomenon, and a number of other related effects, are now known to be connected with such "rotation-aligned" states. In the remainder of this lecture I want to try to trace how the inclusion of such states can effect a smooth transition between fully collective and fully non-collective regions of nuclear behavior.

In the upper left portion of Fig. 6 a completely collective behavior is illustrated. The nucleus is taken to be prolate, as indicated by the small β-γ plot, and each intrinsic state (angular momentum along the symmetry axis is ignored) has a collective rotational band corresponding to rotation about the axis perpendicular to the symmetry axis. The total angular momentum is just that of the collective motion, $\omega\theta_{coll}$.

In the upper right portion of Fig. 6 a small amount of single particle angular momentum, aligned along the rotation axis, j_a, has been added. The orbits of these particles are roughly in the plane

perpendicular to the rotation axis, and will cause a bulge in the otherwise prolate nucleus. Thus the nucleus necessarily becomes slightly triaxial as indicated in the small β–γ plot. The total angular momentum is now the sum of the collective part, $\omega\theta_{coll}$, and a single particle part, $\Sigma\, j_a$. The energy of the bands is given by:

$$E(I) = \frac{R^2}{2\theta_{coll}} + E(j_a) = \frac{(I - j_a)^2}{2\theta_{coll}} + E(j_a) \quad , \tag{19}$$

where $E(j_a)$ is a band-head energy. These are just parabolas whose horizontal displacement from the axis is j_a and whose vertical displacement is $E(j_a)$. The solid lines in Fig. 6 represent these bands. If one assumes j_a and θ_{coll} to be fixed in each band, then the collective E2 γ-ray energy is just twice the slope of these bands and is given by:

$$E_\gamma = 2 \left.\frac{dE(I)}{dI}\right|_{J_a,\theta} = \frac{4(I - j_a)}{2\theta_{coll}} \quad . \tag{20}$$

The assumption of constant j_a and θ, need not be valid, since these quantities could change gradually within a given band, however, there are now both experimental and theoretical reasons to believe this is a reasonable assumption. The usual form of writing Eq. (20) is:

$$E_\gamma = \frac{4I}{2\Theta_{eff}} \quad , \tag{21}$$

where Θ_{eff} is defined by this relationship. There is no displacement, j_a, in this expression, so that it corresponds to the envelope curve (dashed) in Fig. 6. The average slope, and thus E_γ, are the same for this envelope and for the populated portion (near the envelope) for the real bands, so that one cannot distinguish the real band structure this way. From the γ-ray energies, one gets the proporties of the envelope, which should be compared with those for the rigid classical rotors discussed in connection with Fig. 4. The fact that there is aligned angular momentum inevitably reduces the collective (band) moment of inertia, as a given particle cannot contribute fully to both the alignment and the moment of inertia. Thus the curvature of the real bands in the upper right part of Fig. 6 is larger than that of the envelope. To measure this curvature, one must look for <u>differences</u> between consecutive γ-ray energies:

$$\Delta E_\gamma = 2\,\frac{dE_\gamma}{dI} = \frac{4d^2E(I)}{dI^2}\bigg|_{j_a,\Theta_{coll}} = \frac{8}{2\Theta_{coll}} \quad . \tag{21}$$

Note that this difference must be between two (correlated) γ-rays within the same band, and cannot be a difference of average γ-ray energies. There are now experiments sensitive to this curvature, and I will discuss them in the last lecture. The pattern illustrated in this portion of Fig. 6 has considerable experimental support. The

sketched band crossings correspond to backbends, the first of which in the yrast sequence is very well studied, and the second in this sequence has been seen in several cases. In a few nuclei, as many as four or five backbends have been observed in bands above the yrast line. This behavior will be discussed in the next lecture. It is clear that rotational nuclei generally behave this way.

In the lower left part of Fig. 6, the alignment process is assumed to continue. The nucleus is moving toward an oblate shape as more particles align and thereby move in roughly circular orbits perpendicular to the rotation axis. The total angular momentum is now mostly aligned, Σj_a, with only a modest collective contribution. The band head energies are indicated as dots, and they have moved out rather close to the envelope line. As sketched (somewhat arbitrarily), there is only an average of 6 or 8$\hbar$ of collective angular momentum in the bands at the spins where they are likely to be populated (along the envelope). The band heads were not indicated in the previous panel (upper right); where they were rather far from the envelope line—15-20$\hbar$ on the average—corresponding to a considerably larger collective contribution to the total angular momentum. The curvature of the bands is much larger now since the shape is becoming more oblate, and the rotation axis will then become a symmetry axis. Another way to view this is that most of the reasonably high-j particles are aligned and thus can no longer contribute to the collective moment of inertia. These bands show a much higher rate of crossing, and although the slope, Θ_{eff}, behaves regularly, the detailed band structure will be

quite irregular. We will see in the last lecture that there is some evidence for behavior like this.

Finally in the lower right part of Fig. 6 the nucleus has acquired an axially symmetric oblate shape—the rotation axis has become the symmetry axis and collective rotations cannot exist about this axis. The band heads now scatter around the envelope line and are purely single-particle states. At $\beta = 0$ these would be the usual spherical shell-model states, but reasonably large β values may also occur. Such states are observed in several regions and will be discussed in Lecture 4. We have thus followed the motion from collective to non-collective in a continuous way by aligning more and more particles.

Several comments about this transition should be made. First, the general pattern as more angular momentum is added would be to progress through the panels aligning more and more particles. However, this can be altered at any point by shell effects, just as the starting prolate shape is due to a shell effect. Furthermore, at some high spin the liquid drop model suggests that the nuclear structure will be dominated by shapes with very large deformations—prior to fission. These will produce a "bending over" of the envelope curve and probably also a shift to less alignment. Finally, in the last panel, and the next-to-last one, there can be important collective rotations about the perpendicular axis, provided β is not too small. At high spins, however, these rise rather steeply off the yrast line, and it is not clear what role they will play. In the lower left panel, these

combine with the bands shown to give the well known behavior of a triaxial rotor.

This sequence of events is not the only one possible. There can be prolate nuclei rotating about their symmetry axis (band heads in the first panel), or the collective rotation of oblate nuclei (mentioned above). However, the sequence discussed traces a transition between the two situations strongly favored by the liquid drop model. One expects these to be the most common combinations of collective and non-collective motion at high spins. Furthermore there is good evidence that nuclei do exist with behavior like that shown in the first, second, and fourth panels. In the remainder of these lectures I will try to tell you what we know about such nuclei and how we are trying to learn more.

3. BACKBENDING

Backbending refers to an irregularity in the rotational energy levels of a nucleus (Johnson, et al., 1971). An example of this effect is shown in Fig. 7. The main plot of E vs I shows that the effect on the energy levels is quite small--barely visible. However, in the conventional backbending plot (insert) it is a large effect. This plot is of moment of inertia (Eq. (11)) against the square of rotational frequency (ω), which can be taken as about half of the collective γ-ray energy (Eq. (10)). In fact, since it is the γ-ray energies that are directly measured, the observed effect is large and thus easy to study.

Backbending in and around the rare earth region of deformed nuclei is shown in Fig. 8, each section of which is a plot similar to the insert in Fig. 7. It is clear that the light rare-earth region has strong backbenders, as does the region around Os. However, the neutron-rich nuclei in the middle of the region seem to backbend much less, if at all. The only other large strongly deformed region in the periodic chart, the actinides, has no known backbenders. Thus it seems that the effect comes and goes in different regions, and can even show considerable variation from nucleus to nucleus within a region.

3.1. The Cause of Backbending. One of the best studies backbending nuclei is ^{164}Er (Lee, et al., 1976; Johnson, et al., 1978). Part of the level scheme of this nucleus is shown in Fig. 9. The levels on the right are those of the ground band, those in the center belong to

a band that is seen to cross the ground band at spin 16, and the ones one the left are those of the so called γ vibrational band, or γ-band. A plot of these level energies against spin is shown in the lower part of Fig. 10. the ground band (squares) is crossed first at spin 14 by the band labeled "yrare even," and then again at the very highest observed spins (22) by a band labeled "yrast even." The γ-band is crossed around spin 10 by the extension of the yrast-even band, and at about spin 14 by the yrare-even and yrast-odd bands.

The backbending plots of these bands are shown in Fig. 11. Those for the ground and yrast-even bands are on the left, and one sees that individually they are reasonably smooth lines. However, the yrast levels switch at spin 14 from the ground band to the yrast-even band, using one interband transition. This sequence forms the usual backbend, which is now seen to result from pieces of two different bands. At the crossing point there is an interaction between the bands which perturbs a few of the levels. This causes some scatter in the level energies at just this point, as can be seen in the solid points in Fig. 11. A constant interaction matrix element of 45 keV between levels in the two bands results in unperturbed level positions given by the open circles in Fig. 11. These are quite smooth. The E2 branching ratios can also give a value for the mixing and thus the interaction matrix elements. This analysis gives 50 keV, in excellent agreement with the above value form the energies. The interpretation of this backbend as a crossing of two bands seems very convincing.

The right side of Fig. 11 shows the backbending plot for the γ-band in ^{164}Er. The odd spin members are smooth up to spin 13, where the backbend occurs. The even spin members, however, show a perturbation at spin 10. A shift of 25 keV in the 10^+ member of this band (open circles) just removes this perturbation, and is what one might expect from the intersection with the yrast-even band, although its 10^+ member has not been observed. The absence of a similar effect in the odd-spin members is good evidence that the yrast-even band has no such states (hence the name). The fact that the bands may have only even or odd spins is an expected result of strong Coriolis interaction at high rotational frequencies and is referred to as the "signature." The backbend around spin 14 occurs in both the even and odd spin states showing the presence of both of these in the crossing bands (yrast odd and yrare even). This entire behavior is very well reproduced in simple calculations as is shown in the top part of Fig. 10. In this interpretation the two upper bands, together with the yrast-even band, all are 2-quadiparticle states where the two particles correspond to $i_{13/2}$ neutrons whose angular momentum has been largely aligned along the rotation axis. Finally the yrare-even band is seen in Fig. 10 to be likely to intersect the ground band (vacuum) at the highest spins observed (22$\hbar$), and this probably causes the upbend in this band shown in Fig. 11. This nucleus is one of the most favorable for observing backbending behavior, though there are some other excellent examples. It is clear that backbending is the result of a band crossing, and the interesting question then has to do with the nature of the crossing band.

The observed blocking effects can give rather strong clues about the nature of the band causing backbending. The idea behind blocking is that one studies a band in an odd-mass nucleus where the odd particle occupies some particular orbital, say an $i_{13/2}$ neutron orbital. If, then, the crossing band involves this $i_{13/2}$ neutron as one of its components, the crossing will not occur in the odd-mass nucleus since that orbital is already occupied and not available. Exactly this is seen to occur in Fig. 12, where the $i_{13/2}$ band in ^{157}Er is plotted together with the ground bands of both ^{156}Er and ^{158}Er (Grosse, et al., 1973). Whereas the even-even nuclei backbend at $(\hbar\omega)^2 \approx 0.08$, the $i_{13/2}$ band in ^{157}Er clearly does not. This is evidence that this particular orbital is indeed involved in the crossing band. The $h_{11/2}$ proton orbital can also be tested by studying this band in odd-mass Ho nuclei. Figure 13 shows the data (Grosse, et al., 1974), which indicate clearly that the $h_{11/2}$ band does backbend like the adjacent even-even nuclei, and is therefore not involved inthe crossing band. Many tests of this type have shown the crossing band to be composed of two aligned $i_{13/2}$ neutrons in the light rare-earth region. In the heavier region (around Os) this may also be the case, but that is not so clear yet.

A second backbend has been observed in the yrast sequence of a few nuclei. In Fig. 14 data for ^{158}Er are shown (Lee, et al., 1977) together with the level scheme of this nucleus above spin 22. The corresponding backbending plot is shown in Fig. 15, where a usual backbend is seen around $(\hbar\omega)^2 \approx 0.08$, and in addition a strong

upbend at $(\hbar\omega)^2 \approx 0.18$. This upbend indicates another band crossing, whose origin is not clear since the appropriate blocking experiments are difficult to do at such high spins. Calculations suggest this (second) pair of quasi-particles correspond to aligned $h_{11/2}$ protons.

3.2. A New Spectroscopy. I have tried up until now to give a brief summary of the well known features of backbending. Referring back to Fig. 6, one sees that these features are very much like the upper right section, where many of the lowest indicated band crossings have been seen in these backbending nuclei. There is developing a much more detailed examination of band crossing properties, and I want to try to give you the general idea of this development. I shall have to begin by considering the calculations of high-spin properties.

It is not my purpose to discuss in detail the calculations of nuclear properties at high angular momentum. However, a brief summary will be given to provide some references for easy access to more details, and to give some background for results that will be needed later. The whole shell-model concept involves calculating the individual nucleon orbits in the average potential generated by the rest of the nucleons. It was the introduction in 1949 (Mayer) of a large spin-orbit ($\underline{\ell}\cdot\underline{s}$) term to a harmonic oscillator or square well potential that made the shell model work so well for spherical nuclei. By 1955 Nilsson had introduced a r^2Y_{20} deformation term to the harmonic oscillator potential (and an ℓ^2 term to flatten it) and calculated the levels of deformed nuclei. Since this "ad hoc" potential did not have the proper behavior for large deformations, Strutinsky (1966)

devised a procedure to normalize its average behavior to that of the liquid-drop model. Pairing could be added in a reasonably simple (BCS) approximation (Bohr, et al., 1958). This modified harmonic oscillator (MHO) model has been enormously successful for deformed nuclei. It was reasonably straightforward to "crank" this potential round the x axis by adding a term, $-\omega j_x$, and calculate the orbits in a potential rotating with frequency ω (Bengtsson, et al., 1975; Neergaard, et al., 1975, 1976; Andersson, et al., 1976). Some result of this procedure will be shown below. A variation to this approach is to use a Wood-Saxon (WS) potential (Neergaard, et al., 1977). This removes some problems in the average moment of inertia having to do with the ℓ^2 term in the MHO potential, but on the whole seems to give very similar results. A basic improvement has been the introduction of the Hartree-Fock (HF) potential, where self consistency between the potential and calculated orbits is required. Pairing can be included in a more fundamental way in the Hartree-Fock-Bogulubov (HFB) method, making this approach very promising (Mang, 1975; Faessler, et al., 1976; Goodman, 1979). Results are now becoming available for the high-spin region and again they seem not to differ much from the MHO or WS potential. At the present time the greater development of, and experience with, the MHO potential makes it still quite competitive with the others.

The first output of results from any of these calculations is the behavior of individual orbitals with increasing rotational frequency. In the spherical shell model there is a $(2j + 1)$ degeneracy of levels

in a j-shell, which is largely lifted by deforming the potential, as is indicated in Fig. 16. This is a portion of the so-called Nilsson diagram and shows the energy of levels as a function of deformation, ε, where $\varepsilon = 0$ is the spherical shape. The energy is given in units of the oscillator energy

$$\hbar\omega_0 = 41/A^{1/3} \quad \text{MeV} \quad . \tag{22}$$

The resulting levels are two-fold degenerate corresponding to time reversal symmetry of the nucleon motion, and are characterized by their projection on the symmetry axis, Ω. If a given deformation, say $\varepsilon = 0.2$, is chosen, the resulting system can be cranked, and Fig. 17 shows a portion of the levels in Fig. 16 at $\varepsilon = 0.2$ as a function of cranking frequency ω, given in units of the oscillator frequency, ω_0. The energy $e'(\omega)$ is in the rotating frame and in units of $\hbar\omega_0$. The time reversal degeneracy of the levels is lifted, and the slope of these levels $de'(\omega)/d\omega$ is proportional to the aligned angular momentum. The strongly aligned high-j orbits are the steeply down-sloping ones, with a limiting slope corresponding to their maximal alignment. Figure 18 is a diagram of this same type, except that pairing is included, and it covers only a very restricted region, the five states nearest the Fermi level. The $e'(\omega) = 0$ line is the Fermi level, and each state is relected around this line, so that it appears twice. A rough way to think about this is that in one case ($e'(\omega) < 0$ for low ω) the level is included in the pairing correlations, and in the other

($e'(\omega) > 0$ for low ω) it is not included, so that it is a quasiparticle. If particles are placed in the levels labeled A and B (thereby necessarily emptying those labeled -A and -B), a two-quasiparticle excited band is formed which corresponds (at $\omega \gtrsim 0.02$) to the most-aligned $i_{13/2}$ components. As the frequency increases the energy of this band drops relative to the fully paired vacuum ($e' = 0$) until at the point leveled ω_1 it crosses the vacuum and becomes lowest in energy. This crossing has been observed in many nuclei and corresponds to the first "backbend." If one follows only the lowest band, then this process may be expressed as AB unpairing (or aligning) at frequency ω_1. The important point is that AB will unpair in essentially every band at this frequency. For example, the two-quasiparticle band EF will be crossed by the four-quasiparticle band ABEF, again at ω_1, and for EF one could substitute CD, or CDEF, etc. The frequency is a measurable quantity ($\sim E_\gamma/2$), and the above argument says that at certain transition energies many bands at widely different excitation energies will experience a backbending (band crossing). However, a complication occurs if state A has a quasiparticle in it (either a single one in an odd-mass nucleus or one of a pair such as AE in an even-even nucleus). Then AB cannot unpair--A is blocked--and this backbending will not occur. The frequency then increases normally with spin to about $\omega = 0.36$ MeV, the point marked ω_2, where BC will unpair and align. Again this band crossing can happen in many bands. It is worth noting that at about this same

frequency—0.36 MeV—AD unpairs, so that if B rather than A is blocked, then AD can unpair and cause a band crossing.

The experimental data that support such a picture are shown in Fig. 19 (Riedinger, et al., 1980). Here the aligned angular momentum i is plotted vs the frequency ω. The aligned angular momentum is obtained from the experimental data by subtracting the spin of the ground band (no quasiparticles) from the spin of the band of interest at the same rotational frequency (transition energy). The upbends or backbends in Fig. 19 correspond to band crossings, and the sharp backbend in the ground band at frequency 0.27 MeV is in reasonable agreement with the AB unpairing frequency of 0.23 MeV in Fig. 18. The remarkable feature of Fig. 19 is the coincident upbending of six bands at frequencies around ω_2, 0.36 MeV. These include three bands where A is blocked (AE and AF in ^{160}Yb and A itself in ^{161}Yb), two where B is blocked (BF in ^{160}Yb and B itself in ^{161}Yb), and the pairing vacuum as an excited band above the point where AB crossed. The yrast band has a second band crossing at frequency ω_3 around 0.42 MeV which is probably due to a pair of protons and thus is not shown in Fig. 18.

Some important new features emerge from this study which suggest a new "spectorscopy" of bands and backbends at these high spin values. Bands can be characterized by their signature (odd or even spin members) and their alignment, i, in addition to the usual properties, parity and excitation energies. Backbends can be characterized by the

frequency, ω, at which they occur, the alignment change, Δi, and the amount of interaction between the bands. From these properties it should be possible to identify the observed features with those of calculations such as one shown in Fig. 18. It will be very interesting to see how far one can develop such analyses of high-spin bands and backbends.

4. NON-COLLECTIVE BEHAVIOR

Non-collective states occur when the nuclear angular momentum is carried by a few high-j particles and is aligned along a symmetry axis. This leads to an irregular yrast line, along which there are no collective transitions as has been discussed in connection with Figs. 4 and 6. One result of this behavior is that the statistical transitions compete better against the (non-collective) yrast-like ones and cool more of the population intensity to the yrast line at relatively high spin. Thus, not only is there the possibility of isomers, the "yrast traps" (Bohr and Mottelson 1974) but there is an enhanced probability to populate them at very high spins. Both for this reason and because of the complexity of the non-collective level schemes, these studies have been made essentially only on resolved spectra.

4.1. Lead Region. The region around doubly-magic ^{208}Pb has good examples of non-collective high-spin states. The nuclei here are nearly spherical so that every axis is a symmetry axis. One example in this region is ^{212}Rn, with four protons beyond the double closed shell. The levels up to I = 19 at 5.7 MeV appear to be rather pure proton shell-model configurations, as shown in Fig. 20 (Horn, et al., 1977). Above this spin, the neutron core is excited and the higher spin states involve both neutrons and protons, as indicated by the g-factors of the isomeric states. These states have the non-collective behavior described in Section 2. Such a near-spherical (slightly oblate) nucleus, however, may be considered to rotate "effectively" with an effective moment of inertia, whose value can be

obtained from a plot of excitation energy vs $I(I + 1)$, that is,

$$2\mathcal{J}/\hbar^2 = d[I(I + 1]/dE \ . \qquad (23)$$

Such a plot for ^{212}Rn is shown in Fig. 21, where two regions of differing slope are apparent; one below ~6 MeV where only protons are excited, and the other above 6 MeV where both protons and neutrons are involved. If collections of independent particles under rotation do behave, on average, like a rigid rotor, as has been suggested, the high-energy region should have approximately the rigid-body moment of inertia. The rigid-sphere value has been drawn in as the dashed line (arbitrarily normalized vertically), and it can be seen that the slopes are similar. This is taken to indicate a general validity to the idea of effective rotation about a symmetry axis; however, shell effects are expected to be large, and it is not clear to what extent the close agreement with the rigid-body value in Fig. 21 is accidental.

4.2 Hafnium Region. In the discussion of rigid deformed rotating shapes in Lecture 2, the rotation of an oblate nucleus around its symmetry axis had the lowest energy for a given deformation (at moderate spins), while that of a prolate nucleus around its symmetry axis had the highest energy and so would not be expected to occur very often. Nevertheless it does occur in the region of the stable Hf nuclei, in particular in ^{176,178}Hf. These are strongly prolate nuclei with well-formed rotational bands. For such prolate deformation ($\beta \sim 0.3$) in this region of N and Z, the $g_{7/2}$ and $h_{11/2}$ proton

orbitals and the $h_{9/2}$ and $i_{13/2}$ neutron orbitals are nearly full, so the fermi level comes nearest to their high-Ω projections. These projections, then, lie lowest in excitation energy and can form high-K states (where angular momentum is aligned along the symmetry axis) without as large an expenditure of energy as required by the collective rotation.

The partial level scheme for ^{176}Hf is shown in Fig. 22 (Khoo, et al., 1976). The four-quasiparticle (14^-, 15^+,16^+) and six-quasiparticle (19^+,20^-,22^-) bandheads are well described by the Nilsson model, and their projections on the symmetry axis, K, appear to be reasonably good quantum numbers, as is evidenced by the K-forbidden transitions from the 14^- and 19^+ bandheads. The fact that the 16^+ isomer drops below all other I = 16 states has been reproduced in a calculation using the cranked modified oscillator potential at a fixed deformation and taking into account pairing as well as the hexadecapole degrees of freedom (Åberg 1978). This is simply a shell effect. The calculation further suggests that around spin 40$\hbar$ collective rotation again becomes lowest in energy. Qualitatively similar behavior is indicated for all the even-even Hf nuclei from mass 172 to 180. The interpretation of these high-K states as effective rotations about a symmetry axis is in no way contrary to the conventional interpretation based on Nilsson assignments for them. However, it adds a perspective both on their competition with the purely collective states and on their relationship to states in spherical (and oblate) nuclei.

4.3 N = 82 Region. Most of the presently known examples of effective (non-collective) rotation at high spins come from the region just above 82 neutrons. The various theoretical calculations mentioned in Lecture 3 predict slightly oblate nuclei for this region, consistent with this behavior. The calculations also predict that a few nuclei in this region will become rather strongly oblate (non-collective) at very high spin (>40ħ). This implies the existence of isomeric traps along the yrast line at high spin, providing a challenge for experimentalists.

The first systematic search for high-spin isomers was performed by Pedersen, et al. (1977) using targets from Ba (Z = 56) to Bi (Z = 83) irradiated by pulsed beams of ^{40}Ar, ^{50}Ti, and ^{65}Cu. The recoiling evaporation residues were caught on a thin lead foil which was viewed by 16 NaI(Tl) counters operated in coincidence. An event in the Pb foil that triggered several detectors would indicate a high-spin isomer with quite high sensitivity. Isomers below 35ħ were found to occur systematically in a fairly small region of non-rotational nuclei, as shown in Fig. 23. A second study of this region with a total-energy γ-ray spectrometer in coincidence with Ge(Li) detectors (Borggreen, et al., 1980), has determined the excitation energies of the isomers as well as their halflives and γ-ray multiplicities. Twenty-two isomers were found or confirmed, and the island of isomers was shown to be limited to the region with $82 \leq N \leq 86$ and $Z \leq 68$. The isomeric states have excitation energies ranging from 3 to 12.2 MeV and spins (determined by an empirical relationship) up to

$(33 \pm 2)\hbar$. The structure of the isomers can be ascribed to the alignment of a small number (2-8) of shell-model particles in a spherical or slightly oblate potential (Døssing, et al., 1977, Andersson, et al., 1978, Cerkaski, et al., 1977, Faessler, et al., 1976a). There was no indication of isomeric states at very high spins within the limitations set by the experimental arrangement, 20 ns < $T_{1/2}$ < 500ns, indicating no strongly oblate shapes there.

Two of the best studied nuclei in this non-collective group are ^{152}Dy (Khoo, et al., 1978, Merdinger, et al., 1979, Haas, et al., 1979) and ^{154}Er (Baktash, et al., 1979); the level scheme of the former is shown in Fig. 24. Both nuclei show the irregular level spacing and the existence of isomeric states which are characteristic of this non-collective mode of excitation. But the transition energies are not completely random; with very few exceptions they fall within the limits (700 ± 200) keV. Also, there are no E3 transitions, as might be expected from a pure spherical Nilsson potential, and indeed are seen in the nuclei above ^{208}Pb (^{212}Rn for example, Fig. 20). Another aspect, especially apparent in ^{154}Er, is that there are sequences of γ-rays of almost constant intensity which are electric quadrupole. These two- or three-step sequences have transitions of (600 ± 100) keV with lower-energy lines connecting the different sequences. So there are certainly elements of weak collectivity present, waiting for a more detailed understanding. Also at higher spins (>40$\hbar$) there is evidence for still greater collectivity as will be described shortly.

A striking feature of these level schemes is illustrated in the plot of excitation energy vs I(I + 1) for ^{152}Dy in Fig. 25. Initially the experimental data rise rapidly due to a decrease in the pairing, and then at about spin 16$\hbar$ turn over into an approximately straight line up to the highest spin, 36$\hbar$. The slope of this long straight portion of the curve leads to the determination of an effective moment of inertia through Eq. (23). For ^{154}Er this yields $2\mathcal{J}/\hbar^2$ = ~140 MeV^{-1} and for ^{152}Dy, ~142 MeV^{-1}. These values are 10-15 percent greater than those of a rigid diffuse sphere of the appropriate mass. This increase could be considered an indication of deformation, and if so taken, would correspond to $\beta \approx 0.2$ for a deformed oblate shape, a rather large deformation. Certainly where collective rotation is considered, the slope of the curve, and hence the effective moment of inertia, is thought to bear a connection to the deformation of the nucleus. But here, near a magic number, where the angular momentum is being carried largely by a few particles aligned along the rotation axis, it seems more likely that shell effects will be large and might affect this slope. Results of several recent calculations support this view. For example, Fig. 26 shows curves calculated for several nuclei with neutron numbers around N = 82 using a cranked spherical Nilsson potential and BCS pairing (L. Moretto, unpublished work 1979), and it can be seen that due to shell effects even larger differences in slopes appear than are seen in experiment. Similar results are found by Leander, et al. (1979), and these authors point out the importance of pairing in calculating these moments of inertia

and the configurations of states along the yrast line. Thus, at the present time, it seems likely that slopes such as that in Fig. 25 cannot be used very directly to indicate deformation. Values for these nuclei must be determined by another method.

The measurement of the static quadrupole moment of a state gives clear information about deformation, and such measurements can in principle be made on nanosecond isomers using perturbed angular distribution techniques. The first such determination at high spin for nuclei in this region has been performed on the ($I \sim 49/2^+$) 500 ns isomer in ^{147}Gd (Hausser, et al., 1980). The quadrupole moment obtained was ($|3.14| \pm 0.17$) b, from which a deformation β of -0.18 was derived (the negative sign was assumed). This is a reasonably large deformation, two or three times that implied by the aligned particles alone. Thus, it is the first real indication that sizeable oblate deformations might exist in this region. Nevertheless, these are very difficult experiments, and more such data are badly needed.

It no longer seems very likely that isomers will be found at spins significantly above these examples (~30). This is due in part to the steepness of the slope of the yrast line at the higher spin values, but also might be an indication that the strongly oblate shapes are not quite so stable as the present calculations indicate. There is some information that bears on this point from the studies of unresolved γ-ray spectra.

A group at Orsay has recently studied ^{154,155}Er in comparison with ^{159,160}Er by bombarding targets of ^{119}Sn and ^{124}Sn with ^{40}Ar beams of appropriate energy (Deleplanque, et al., 1979). The ^{159,160}Er

nuclei have a γ-ray spectrum showing the characteristic collective yrast bump below 1.6 MeV (see Lecture 5). The ^{154,155}Er nuclei give a very different spectrum showing two bumps below 1.6 MeV separated by a valley at about 1 MeV. The low-energy bump contains all the known discrete transitions in ^{154,155}Er around 0.7 MeV connecting states with spins up to 36$\hbar$. The higher bump starts at ~1 MeV, and above its maximum at 1.3 MeV resembles the upper part of the rotational bump in the ^{159,160}Er product nuclei. This second bump develops very strongly with increasing multiplicity, showing that it comes from high-spin states. The multipole composition of the γ-ray spectra, deduced from the 0° and 90° intensities (with the assumption of only stretched dipole and quadrupole transitions), shows that the upper bump in ^{154,155}Er consists mainly of stretched quadrupole transitions. This is not true for the lower peak, which has a large fraction of dipoles, in agreement with the known discrete lines in ^{154,155}Er. The calculated spin at the top of the cascade is ~60$\hbar$ and the moment of inertia is ~150 MeV^{-1}. The evidence seems quite good that, at about spin 40$\hbar$, the products ^{154,155}Er switch from weakly oblate nuclei, to rather strongly deformed (most likely rotational) nuclei. The experimental results do not determine whether these shapes are oblate or prolate, but the similarities with the heavier Er nuclei suggest the latter.

5. COLLECTIVE BEHAVIOR

The highest spin states that exist in nuclei can be populated following heavy-ion reactions, as discussed in Lecture 1. The γ-ray cascades deexciting evaporation residues from such reactions have been illustrated in Fig. 3 and generally go through hundreds or even thousands of different pathways. Only below ~30$\hbar$ does the population concentrate sufficiently in the lowest few bands to permit observation of individual γ-ray transitions. Above this spin there is only an unresolved spectrum—loosly called the "continuum." To study the highest spin states in nuclei one must study these unresolved spectra, and I will try to convince you that this represents a challange not a curse.

Many different kinds of studies have recently been made on the continuum spectra. In the present section I will discuss just a few of these; first, to demonstrate that some kind of collective rotation is involved, and secondly to evaluate the effective moments of inertia for this rotation. In the last Lecture I will describe the γ-ray energy correlation studies currently being developed. It should be clear that this is not a comprehensive review of all the work done on continuum γ-ray spectra, but only some selections which I hope will give you the flavor and general progress of work in this area.

5.1. Evidence for Rotation. The γ-ray spectrum from a rotational nucleus is highly correlated in time, spatial distribution, and energy. Part of a rotational energy-level diagram is shown on the left side of Fig. 27, and the corresponding γ-ray spectrum on the

right side. This spectrum is seen to be composed of equally spaced lines, up to some maximum energy corresponding to the decay of the state with highest angular momentum, I_{max}. There are at least two kinds of correlation in this spectrum. One is of the maximum γ-ray energy with I_{max}, and in the present section this correlation will be used, first to identify rotational behavior and then to evaluate the effective moments of inertia associated with the rotation. In the next section, another correlation will be discussed, that between γ-ray energies.

I will begin with an early example of continuum γ-ray studies, and then consider some of the more recent work. Figure 28 (Simon, et al., 1977) shows the de-excitation spectra of ^{162}Yb from the reaction (181 MeV) $^{40}Ar + ^{126}Te \rightarrow ^{166}Yb^*$, taken with three NaI detectors. The events were selected by requiring a coincidence with a known ^{162}Yb transition identified in a Ge(Li) detector. The yrast bump ($E_\gamma \lesssim$ 1.5 MeV) and statistical regions ($E_\gamma \gtrsim 1.5$ MeV) can be distinguished even in the pulse-height spectrum (open squares). However, if this is "unfolded" (Mollenauer 1961), that is, corrected for the NaI response function to give the primary γ-ray spectrum (filled circles), the components are considerably clearer. The latter curve has been corrected for counter efficiency to give the absolute number of γ-ray transitions per event per transition-energy interval (40 KeV). Summing the whole curve gives the average γ-ray multiplicity (minus the gate transition in the Ge(Li) detector), in this example, 24.

The top of Fig. 28 shows the ratio of events at 0° to those at 90° in the unfolded spectra for this case. Although for $E_\gamma > 2$ MeV this ratio is near unity, in the region of the yrast bump between 0.8 and 1.5 MeV it is considerably larger, with ratios as high as 1.5 ± 0.15. This is the value expected in such a beam-gamma correlation for nearly pure stretched E2 transitions. However, there is some ambiguity; similar, or larger, ratios could be obtained from $\Delta I = 0$ dipole transitions. Fortunately, these can be ruled out as a major component of the cascades because the number of γ-rays measured per event, the γ-ray multiplicity, would otherwise be too small to carry off the angular momentum in the nucleus. The majority of the transitions must be "stretched", either dipoles or electric quadrupoles. (Magnetic quadrupole and higher multipolarities are ruled out by lifetime considerations, as discussed below.) At transition energies less than 0.8 MeV the 0°/90° intensity ratio falls, and below 0.4-0.5 MeV, it goes below one (not shown in Fig. 28), suggesting mainly stretched dipole transitions. Although different techniques have been employed, similar results have been obtained for the continuum cascades in other strongly deformed nuclei (Simon, et al. 1979, Hagemann, et al., 1979, Trautmann, et al., 1979, Vivien, et al., 1979).

At the bottom of Fig. 28, a full line has been drawn to represent schematically the unfolded continuum spectrum (filled circles above) from the 181 MeV ^{40}Ar irradiation of ^{126}Te to make ^{162}Yb by a 4n reaction. The long-dashed line is a similar representation of the unfolded spectrum from a 157 MeV ^{40}Ar bombardment. The former

reaction brings, on average, about 40ħ to the γ-ray cascade, while the latter brings only 25-30ħ. It is clear that the higher spin causes additional γ rays (the difference in area of the curves is about six transitions) with higher transition energies, and so moves the edge of the yrast-like transitions to higher energy. This movement (E_γ,I correlation) was one of the earliest indications that rotation was involved in many of these de-excitation cascades. The dotted and short-dashed lines in the same figure are representations of the unfolded spectra from the reactions (331 MeV) $^{86}Kr + ^{80}Se$ and (87 MeV) $^{16}O + ^{150}Sm$, respectively, to yield the same products, $^{162}Yb + 4n$, and both reactions involve, on average, about the same angular momentum (25-30ħ) as the 157 MeV ^{40}Ar case. It can be seen that these three spectra are almost identical, illustrating that angular momentum is the important variable rather than some other property of the system.

Perhaps the most important method so far used to determine the multipolarity of the unresolved γ-rays is based on angular distributions. A recent development in this direction involved beam-gamma-gamma angular correlation measurements. One such measurement used an array of six NaI counters to select the observed nuclei so that the sensitivity to different types of radiation was enhanced (Deleplanque, et al.,1978a). The angular distribution of the selected events was measured with additional detectors, and depended on both the number and angle of the array detectors that fired. The percentage of different multipolarities for each transition energy (channel) in the γ-ray spectrum was deduced by comparing the experimental and

calculated spectra for a given set of conditions. The results for several compound systems are given in Fig. 29. Five types of transitions were considered in the calculations; quadrupoles with ΔI = 0,1,2 and dipoles with ΔI = 0,1. The results, however, are presented only in terms of plots of stretched quadrupole and stretched dipole transitions. This is because the experimental results showed there was rather little (<10 percent) ΔI = 0,1 quadrupole radiation in the spectrum. The ΔI = 0 dipole type cannot be ruled out this way, since it resembles too closely the stretched quadrupoles, but the argument has already been made that the experimental γ-ray multiplicity and the estimated average spin of the nuclei do not allow many ΔI = 0 transitions. One or two ΔI = 0 transitions are not excluded, and in the high-energy statistical region there is some evidence for them from conversion coefficient data. Thus the stretched quadrupole component for E_γ > 2 MeV, where there are very few transitions, could be partly or entirely ΔI = 0 dipole instead.

The spectra in Fig. 29 are composites of up to four very similar individual spectra. The location of the most probable product is given by the appropriate symbol on the section of the nuclide chart shown in the insert; the mass region from A ~ 90 to A ~ 170 is covered. (One region of nuclei, just above the 82 neutron shell, is omitted from this plot and was discussed separately in Section 4) The results show that the stretched dipole component of the yrast-like transitions occurs at the lower energies. It is a relatively weak component in the good rotational nuclei and occurs there only at energies <0.5 MeV. In the non-rotational nuclei the dipole component runs up to 1 MeV and

is much stronger (~50 percent of all transitions); it seems clear that these are associated with non-collective behavior. The higher energy part of the yrast-like transitions is invariably seen to be composed of stretched quadrupole transitions. In the region of deformed nuclei these are no doubt rotational E2 transitions, and the systematic behavior of these transitions in Fig. 29 suggests this may generally be the case. The regular decrease in height of these spectra, together with the edge that moves to higher energies is just what would be expected for maximum spin values like those of Fig. 1 and roughly rigid-body moments of inertia.

Another type of information which shows more directly the collectivity of the continuum cascades is the average transition lifetime. An upper limit can be set by measuring the feeding time to a particular discrete transition near the bottom of the cascade. Dividing this time by the average number of transitions in the cascade gives the average transition lifetime. In early recoil-distance Doppler-shift studies to measure the lifetimes of the discrete transitions, these feeding times were determined as a by-product. The upper limit on the feeding times for a dozen nuclei ranging from ^{120,122}Xe, through some rare-earth nuclei, to ^{184}Hg have all been determined to be <15 ps, and generally ~5 ps (Diamond, et al.,1969, Kutschera, et al., 1972, Newton, et al., 1973, Ward, et al., 1973, Rud, et al., 1973, Bochev, et al., 1975). Since there are ~20 transitions per cascade, an individual transition, on the average, takes a fraction of a picosecond. The average γ-ray energy is ~1 MeV, so

that only a dipole transition or a strongly enhanced electric quadrupole transition is fast enough to satisfy this requirement. Magnetic quadrupole and higher multipole radiation are ruled out. This conclusion applies to the bulk of the transitions; slower ones of low intensity (a few percent) cannot be excluded.

A more detailed measurement can be made by comparing the spectrum from a thin target with that from a similar target backed with lead or gold (Hubel, et al., 1978). States whose lifetimes are short compared to the stopping time in the backing will show Doppler-shifted transitions, while those levels whose lifetimes are longer than the stopping time will not be shifted. To increase the magnitude of the effect, inverse reactions were used. That is, Xe projectiles bombarded targets of ^{27}Al and ^{28}Si to make compound nuclei $^{163}Ho^*$ and $^{164}Er^*$ with velocities 8-9 percent of light. These spectra are shown at the top of Fig. 30. The differences appear quite small, but are magnified when the thin-target spectrum is divided by the backed-target one, as in Fig. 30b for the raw data and in Fig. 30c for the unfolded spectra. The scheme of analysis assumed a rotational cascade decay along the yrast region and depended upon a single parameter, the intrinsic quadrupole moment, Q_0, of the deformed nucleus, or alternatively, the corresponding enhancement factor over single-particle decay. The value of this parameter was obtained from a fit to the ratio of the unfolded spectra, which is shown in Fig. 30c as a solid curve. The enhancement factors found in several experiments are of the order of

200 ± 75, showing that in the spin range 30-50ħ these nuclei are strongly deformed rotors.

A quite different, but powerful, technique to study the spin-E_γ correlation is the measurement of average γ-ray multiplicity as a function of transition energy. Such "multiplicity" spectra for the system $^{40}Ar + ^{124}Sn \rightarrow ^{164}Er^*$ at several bombarding energies are shown in Fig. 31 (Deleplanque, et al., 1978b). There is a pronounced peak at all bombarding energies, and it comes at the upper edge of the yrast-like transitions in the γ-ray spectrum shown above. This multiplicity peak shows clearly that the highest energy yrast-like transitions are associated with the highest spins populated. The right side of Fig. 31 shows γ-ray spectra and multiplicity spectra calculated using a very simple model; a purely rotational yrast-like cascade is assumed. All the significant observed features are reproduced. This provides a rather direct confirmation of the collective rotor picture for this nucleus, all the way from the discrete transitions near the ground state to the highest spins observed, about 60ħ. The moment of inertia used in the calculation was roughly the rigid-body value and was constant over the whole spin range. This suggests that the deformation of ^{160}Er remains prolate, $\beta \sim 0.3$, over the spin range that is heavily populated.

These measurements, and others I do not have time to describe, show rather clearly that many, if not all, nuclei have rotational features at the highest spin values. I now want to go on and show how the moments of interia of such rotors can be determined.

5.2. Effective Moments of Inertia. An early method for determining the effective moment of inertia was based on the energy of the yrast-bump edge (the highest energy transition in the cascades) and an estimate of the corresponding maximum spin (Banaschik, et al., 1975, Simon, et al., 1976). However this involves first estimating a maximum spin and then relating it to the appropriate point on the bump edge. While this can certainly be done approximately, it cannot lead to very precise values.

Recently there has appeared a somewhat more objective method for determining the edge of the yrast-like transitions as a function of angular momentum input. This involves measuring the total γ-ray de-excitation energy by placing the target inside a large NaI crystal with only narrow channels to admit the beam and to let some external counters view the target. The coincident spectrum in the external counters can then be measured for different energy "slices" in the sum spectrum. The top of Fig. 32 shows the spectra taken by an external NaI detector in coincidence with ~4 MeV wide slices of summed energy from such a crystal (Körner, et al.,1979). In the first few spectra the increase in average angular momentum associated with higher sum energy causes an increased yield of essentially all γ-rays. After about slice 5 the yield of the lower energy transitions ($E_\gamma < 0.6$ MeV, $I < 20$) is saturated because the feeding occurs at higher spin. The movement of the yrast-bump edge to higher energy then becomes noticeable, and by subtracting the spectrum of one slice from the next one,

the curves in the bottom of the figure are obtained. Their centroids can be considered to be the average edge, E_γ, for the spectra of the two consecutive slices. The corresponding spin, I, can be obtained from the average multiplicity for the two spectra determined in the same measurement. Using $\bar{I}$ and $\bar{E}_\gamma$ in the relation:

$$\frac{2\mathfrak{I}}{\hbar^2} = \frac{4\bar{I} - 2}{\bar{E}_\gamma} \quad , \tag{24}$$

gives an effective moment of inertia for that γ-ray energy, and values so determined for the compound system ^{164}Er* are shown in Fig. 33. An important advantage of this method is that the "average" edge and the multiplicity are both determined objectively and correspond to the same input distribution of angular momentum. Also no extrapolation from average to maximum angular momentum is required.

A type of differential method can also be applied to the spectra obtained in coincidence with slices of the total-energy spectrum. The area of each difference peak (bottom of Fig. 32) gives the incremental number of rotational transitions (half the angular momentum increase ΔI) and the difference in the centroids of two consecutive peaks gives the average increase in transition energy, ΔE_γ. Use of the relation:

$$\frac{2\mathfrak{I}}{\hbar^2} \approx 8/\Delta\bar{E}_\gamma \quad ,$$

then gives effective moments of inertia which depend essentially on the difference in multiplicities rather than on the multiplicities themselves, and so provides a partially independent evaluation of $\mathcal{J}$. As can be seen in Fig. 33, the integral and differential methods are in good agreement.

This sum-crystal method probably provides the most reliable values presently available for moments of inertia at very high spin. They are in rather close agreement with the liquid-drop model—about 10 percent or so above the rigid-sphere values. A few measurements have been made for comparable spin ranges outside the rare-earth region. They also seem to be near the liquid-drop value. Very careful studies are underway at present to look for the large increase in moment of inertia at the very highest spins that has been predicted by the liquid-drop model, and is reinforced in some regions by shell effects. There is some evidence, both in the A ~ 90 and the A ~ 160 regions, for such a "giant backbend," or at least for moments of inertia well beyond the rigid-sphere value. This is one of the most active and exciting areas of high-spin studies at the present time.

6. GAMMA-RAY ENERGY CORRELATIONS

There are several kinds of correlations in the γ-ray spectrum from a rotational nucleus. In the last lecture it was the correlation between γ-ray energy and spin that was used, both to identify rotational behavior and to evaluate effective moments of inertia. It is the correlation between two (or more) γ-ray energies that will be discussed now. One illustration of this correlation, which is immediately obvious from Fig. 27, is that no two γ-rays have the same energy.

It is easy to illustrate the kind of correlation under consideration. A schematic two-dimensional spectrum of one γ-ray energy against another for a rotational nucleus is shown in Fig. 34. The dots represent the location of coincidences between γ-rays de-exciting states up to I = 14 in a perfect rotational band with moment of inertia $\mathcal{J}$. However, different bands might have somewhat different moments of inertia, and the lines through the dots represent bands having moments of inertia differing by ±10 percent from $\mathcal{J}$. It is also well known that nuclei align angular momentum at relatively low spin values, and the crosses in Fig. 34 are coincidences between transitions from spins 16 to 26$\hbar$ in a band having 11$\hbar$ aligned, also with a moment of inertia $\mathcal{J}$. The light lines through the crosses again represent aligned bands differing in $\mathcal{J}$ by ±10 percent. It is clear that even if bands are populated that differ considerably in moment of inertia and aligned angular momentum, a strong pattern remains in the two dimensional γ-γ coincidence spectrum. The valley along the diagonal, representing the absence of transitions of the same energy, is not at all filled, and the first

ridge adjacent to it is rather clear. (Notice, however, that a single band with a changing moment of inertia or alignment has not been considered.) It is then of considerable interest to know whether these correlations are present in real spectra at very high spins.

To perform such correlation experiments requires good statistics and a method to reduce the number of uncorrelated events. The first successful experiment was made by Andersen, et al. (1979). They used four detectors, resulting in six independent pairs, and, after equalizing the gains, plotted every coincidence on a single two-dimensional spectrum. A background of uncorrelated events, $\tilde{N}_{ij}$, was subtracted from the γ-γ matrix. Basically this background is calculated for the point ij from the projections of the row, $\sum_k N_{ik}$, and the column, $\sum_l N_{lj}$, on the assumption that every observed γ-ray is equally probably in coincidence with every other observed one. The correlated two-dimensional spectrum is then:

$$\Delta N_{ij} = N_{ij} - \tilde{N}_{ij} = N_{ij} - \sum_k N_{ik} \sum_l N_{lj} / \sum_{l,k} N_{lk} \quad . \tag{26}$$

There are some problems with this subtraction method, and others are being explored, but it seems clear that the results discussed here are not much affected by these problems. The original experiments were limited by beam energies to rather low angular momenta. I will discuss a later study (Deleplanque, et al., 1980) applying this method to a system where the maximum angular momentum the nucleus can hold was brought in.

The correlated spectrum for the system $^{124}Sn + {}^{40}Ar \rightarrow {}^{164}Er^*$ at 185 MeV ^{40}Ar energy is shown in Fig. 35. Three features, believed to be general, have been pointed out. First, there is a distinct valley along the diagonal up to about 1 MeV (spin 40ħ) having a measurable width, and there is some possibility this valley also exists in the region above 1.1 MeV. Second, there are a few bridges across this valley beginning as low as 0.55-0.60 MeV, and continuing as far up as the valley persists. Also there are irregularities in the ridges alongside this valley. Finally, there is a general filling of the valley above ~1 MeV, which is rather complete around 1.1 MeV. There are many other features in Fig. 35 that one would hope to understand; however, thus far only these three have been carefully considered.

The interpretation that has been placed on these data is somewhat speculative, but quite interesting. The type of decay pathway envisioned is illustrated in Fig. 36. The scalloped pattern represents successive rotational bands through which the population flows to the ground state. The transition between bands might be a simple band crossing as shown, or might occur via a statistical transition from a higher band (change of temperature, also shown); the assumption is that the band character is not a strong function of temperature. (This is not known to be the case, but represents the simplest starting assumption, and there is no evidence to the contrary.) The mathematical description of such a band structure is reasonably straightforward, and has been given in Eq. (19), and discussed in

Lecture 2. One possible assumption is that $\mathcal{J}_{coll}$ and j_a change smoothly with spin in a band; however, that is not what happens at low spins in the backbending region and it is not suggested by the irregularity of the observed correlation spectrum at high spins. The other limiting assumption is that taken in Fig. 36 (and Fig. 6); that $\mathcal{J}_{coll}$ and j_a are approximately constant in a band and change sharply between bands. In fact, $\mathcal{J}_{coll}$ is also taken to be constant in Fig. 36, and only j_a and $E(j_a)$ change between bands. As discussed in Lecture 2, Eq. (19) describes a parabola, displaced from the origin horizontally by j_a and vertically by $E(j_a)$, and the bands in Fig. 36 are sections of these parabolas. The γ-ray transition energy within one of these bands, holding $\mathcal{J}_{coll}$ and j_a constant, has been given in Eq. (20), and is related to the effective moment of inertia as described in Lecture 2. This relationship has been used in the previous lecture to determine experimental values for such moments of inertia.

The width of the valley in a correlation spectrum is related to the <u>difference</u> between successive transition energies, or to the curvature of the energy expression (Eq. (21)). Thus, the valley width measures $\mathcal{J}_{coll}$ and should give values considerably smaller than the $\mathcal{J}_{eff}$ determined from γ-ray energies (Section 5.2). The first results on this point (Deleplanque et al 1980), <u>suggest</u> that this is indeed the case, with values of $\mathcal{J}_{coll}$ as low as ~0.6 $\mathcal{J}_{eff}$. However, these results are tentative and more data are needed. If $\mathcal{J}_{coll}$, $\mathcal{J}_{eff}$, and I can be reliably measured, then one can obtain

j_a, which would be a very interesting quantity to know for these high-spin states.

The lowest-energy bridges in Fig. 35 are due to known backbends in the nuclei produced. The large one at 0.55 MeV ($\omega \sim 0.27$ MeV) corresponds to the first backbends in ^{158}Er and ^{160}Er (the major even-even products). Backbending or upbending behavior implies several γ rays of similar energies in the band and thus tends to fill the valley. The arguments developed in Lecture 3 have demonstrated that a given level crossing will show up in many bands at the same rotational frequency (the same γ-ray energy). This must be true for the second large bridge at ~0.8 MeV ($\omega \sim 0.42$ MeV), at the location of the second backbend in ^{158}Er, since the population of that backbend in the yrast sequence is quite weak but the bridge is a prominent feature. It is known that the first backbend in this region of nuclei involves the alignment of two $i_{13/2}$ neutrons, and the second probably the alignment of two $h_{11/2}$ protons. There are at least two more higher-energy bridges in Fig. 35, each of which must involve many bands since they have not been observed in any discrete-line studies. It is not yet clear which orbitals are involved in these higher bridges. However, the general behavior up to about 1 MeV γ-ray energy seems reasonably clear--a deep valley reflecting good rotational behavior, and a few large irregularities in both the valley and ridge structure resulting from alignment of specific high-j orbitals.

Above 1 MeV in Fig. 35 the valley is largely filled, and completely so in places. It is not really clear what causes this, but a reasonable extension of the features described above seems able to do it. The

increased band crossing shown in the lower left portion of Fig. 6 is exactly the kind of behavior that could produce such an effect. This increased crossing together with a decrease in the collective moment of inertia, is due to the alignment of additional single-particle angular momenta along the rotation axis. This implies a tendency for the nucleus to become more triaxial. It is interesting that in the region of ^{160}Er (68 protons and 92 neutrons), there may be shell effects that bring on this addition of aligned particles rather suddenly. The particle orbitals from two shells away ($i_{13/2}$ protons and $j_{15/2}$ neutrons) are approaching the Fermi level in such nuclei (which lies in the N = 4 proton and N = 5 neutron shells) at rotational frequences around 0.6 or 0.7 MeV, and deformation roughly β = 0.3. These high-j $\Delta N = 2$ orbitals will be fully aligned and might move the nuclei rather suddenly from conditions like these in the upper right panel of Fig. 6 to those like the lower left panel. It is apparent that such ideas are at present rather speculative.

These E_γ-E_γ correlation experiments certainly represent a frontier in the continuum work. There are detailed features in the low energy region of Fig. 35 that are not yet understood, and the cause for the filling of the valley at high spins represents a major effect to be studied. This kind of experiment could also be done in coincidence with an energy-sum spectrometer, in order to concentrate the observed population more on the highest spins. These correlation studies seem to offer real hope for a detailed understanding of high-spin states without resolving the spectrum.

REFERENCES

Åberg, S. 1978. Nucl. Phys. A306:89

Andersen, O., Garrett, J. D., Hagemann, G. B., Herskind, B., Hillis, D. L., Riedinger, L. L. 1979. Phys. Rev. Lett. 43:687

Andersson, C. G., Hellstrom, G., Leander, G., Ragnarsson, I., Åberg, S., Krumlinde, J., Nilsson, S. G., Szymanski, Z. 1978. Nucl. Phys. A309:141

Andersson, C. G., Larsson, S. E., Leander, G., Moller, P., Nilsson, S. G., Ragnarsson, I. Aberg, S., Bengtsson, R., Dudek, J., Nerlo-Pomorska, B., Pomorski, K., Szymanski, Z. 1976. Nucl. Phys. A268:205

Baktash, C., der Mateosian, E., Kistner, O. C., Sunyar, A. W. 1979. Phys. Rev. Lett. 42:637

Banaschik, M. V., Simon, R. S., Colombani, P., Soroka, D. P., Stephens, F. S., Diamond, R. M. 1975. Phys. Rev. Lett. 34:292

Bengtsson, R., Larsson, S. E., Leander, G., Moller, P., Nilsson, S. G., Åberg, S., Szymanski, Z. 1975. Phys. Lett. 57B:301

Blocki, J., Randrup, J., Swiatecki, W. J., Tsang, C. F. 1976. Ann. Phys. 105:427

Bochev, B., Karamyan, S. A., Kutsarova, T., Subbotin, V. G. 1975. Yad. Fiz. 22:665 as given in Sov. J. Nucl. Phys. 22:343

Bohr, A. 1952. Mat. Fys. Medd. Dan. Vid. Selsk. 26:No. 14

Bohr, A., Mottelson, B. R., Pines, D. 1958. Phys. Rev. 110:936

Bohr, A. and Mottelson, B. R. 1974, Phys. Scripta 10A:13

Bohr, A. and Mottelson, B. R. 1975. Nuclear Structure. Vol. 2. Reading, Mass: Benjamin

Bohr, N. 1936. Nature 137:344

Bohr, N. and Kalckar, F. 1937. Mat. Fys. Medd. Dan. Vid. Selsk. 14:No. 10

Borggreen, J., Bjørnholm, S., Christensen, O., Del Zoppo, A., Herskind, B., Pedersen, J., Sletten, G., Folkmann, F., Simon, R. S. 1980. Z. Phys. In press

Cerkaski, M., Dudek, J., Szymanski, Z., Andersson, C. G., Leander, G., Åberg, S., Nilsson, S. G., Ragnarsson, I. 1977. Phys. Lett. 70B:9

Cohen, S., Plasil, F., and Swiatecki, W. J. 1974. Ann. Phys. 82:557.

Deleplanque, M. A., Byrski, Th., Diamond, R. M., Hubel, H., Stephens, F. S., Herskind, B., Bauer, R. 1978a. Phys. Rev. Lett. 41:1105

Deleplanque, M. A., Husson, J. P., Perrin, N., Stephens, F. S., Bastin, G., Schuck, C., Thibaud, J. P., Hildingsson, L., Hjorth, S., Johnson, A., Lindblad, Th. 1979. Phys. Rev. Lett. 43:1001

Deleplanque, M. A., Lee, I. Y., Stephens, F. S., Diamond, R. M., Aleonard, M. M., 1978b. Phys. Rev. Lett. 40:629

Deleplanque, M. A., Stephens, F. S., Andersen, O., Ellegaard, C. Garrett, J. D., Herskind, B., Fossan, D., Neiman, M., Roulet, C., Hillis, D. C., Kluge, H., Diamond, R. M., Simon, R. S. 1980. Phys. Rev. Lett. In press

Diamond, R. M., Stephens, F. S., Kelly, W. H., Ward, D. 1969. Phys. Rev. Lett. 22:546

Døssing, T., Neergaard, K., Matsuyanagi, K., Chang H. 1977. Phys. Rev. Lett. 39:1395

Faessler, A., Devi, K. R. S., Grummer, F., Schmid, K. W., Hilton, R. R. 1976a. Nucl. Phys. A256:106

Goodman, A. L. 1979. Adv. Nucl. Phys. 11:263

Grosse, E., Stephens, F. S., Diamond, R. M. 1973. Phys. Rev. Lett. 31:840

Grosse, E., Stephens, F. S., Diamond, R. M. 1974. Phys. Rev. Lett. 32:74

Gustafson, C., Lamm, I. L., Nilsson, B., Nilsson, S. G. 1967. Ark. Fys. 36:613

Haas, B., Andrews, H. R., Hausser, O., Horn, D., Sharpey-Schafer, J. F., Taras, P., Trautmann, W., Ward, D., Khoo, T. L., Smither, R. K. 1979. Phys. Lett. 84B:178.

Hagemann, G. B. 1979. Proc. Symp. on High-Spin Phenomena in Nuclei, ANL/PHY-79-4, Argonne, IL, p. 55

Hagemann, G. B., Broda, R., Herskind, B., Ishihara, M., Ogaza, S., Ryde, H. 1975. Nucl. Phys. A245:166

Hausser, O., Mahnke, H.-E., Sharpey-Schafer, J. F., Swanson, M. L., Taras, P., Ward, D., Andrews, H. R., Alexander, T. K. 1980. Phys. Rev. Lett. 44:132

Hillis, D. L., Garrett, J. D., Christensen, O., Fernandez, B., Hagemann, G. B., Herskind, B., Back, B. B., Folkmann, F. 1979. Nucl. Phys. A325:216

Horn, D., Hausser, O., Faestermann, T., McDonald, A. B., Alexander, T. K., Beene, J. R., Herrlander, C. J. 1977. Phys. Rev. Lett. 39:389

Hubel, H., Smilansky, U., Diamond, R. M., Stephens, F. S., Herskind, B. 1978. Phys. Rev. Lett. 41:791

Johnson, A., Ryde, H., Sztarkier, J. 1971. Phys. Lett. 34B:605

Johnson, A., Szymanski, Z. 1973. Phys. Rep. 7C:181

Johnson, N. R., Cline, D., Yates, S. W., Stephens, F. S., Riedinger, L. L., Ronningen, R. M. 1978. Phys. Rev. Lett. 40:151

Khoo, T. L., Bernthal, F. M., Robertson, R. G. H., Warner, R. A. 1976. Phys. Rev. Lett. 37:823

Khoo, T. L., Smither, R. K., Haas, B., Hausser, O., Andrews, H. R., Horn, D., Ward, D., 1978. Phys. Rev. Lett. 41:1027

Körner, H. J., Hillis, D. L., Roulet, C. P., Aguer, P., Ellegaard, C., Fossan, D. B., Habs, D., Neiman, M., Stephens, F. S., Diamond, R. M. 1979. Phys. Rev. Lett. 43:490

Kutschera, W., Dehnhardt, D., Kistner, O. C., Kump, P., Povh, B., Sann, H. J. 1972. Phys. Rev. C5:1658

Leander, G., Andersson, C. G., Nilsson, S. G., Ragnarsson, I., Åberg, S., Almberger, J., Døssing, T., Neergaard, K. 1979. Proc. Symp. on High-Spin Phenomena in Nuclei, ANL/PHY-79-4, p. 197. Argonne, IL

Lee, I. Y., Aleonard, M. M., Deleplanque, M. A., El Masri, Y., Newton, J. O., Simon, R. S., Diamond, R. M., Stephens, F. S. 1977. Phys. Rev. Lett 38:1454

Lee, I. Y., Cline, D., Simon, R. S., Butler, P. A., Colombani, P., Guidry, M. W., Stephens, F. S., Diamond, R. M., Johnson, N. R., Eichler, E. 1976. Phys. Rev. Lett. 37:420

Mang, H. J. 1975. Phys. Rep. 18:325

Mayer, M. G. 1949. Phys. Rev. 75:1969

Merdinger, J. C., Beck, F. A., Byrski, T., Gehringer, C., Vivien, J. P., Bozek, E., Styczen, J. 1979. Phys. Rev. Lett. 42:23

Mollenauer, J. F., 1961. Lawrence Radiation Laboratory Report UCRL-9748

Myers, W. D. 1973. Nucl. Phys. A204:465

Neergaard, K., Pashkevich, V. V. 1975. Nucl. Phys. A268:205.

Neergaard, K., Pashkevich, V. V., Frauendorf, S. 1976. Nucl. Phys. A262:61

Newton, J. O., Lee, I. Y., Simon, R. S., Aleonard, M. M., El Masri, Y., Stephens, F. S., Diamond, R. M. 1977. Phys. Rev. Lett. 38:810

Newton, J. O., Stephens, F. S., Diamond, R. M. 1973. Nucl. Phys. A210:19

Nilsson, S. G. 1955. Mat. Fys. Medd. Dan. Vid. Selsk 29:No. 16

Pedersen, J., Back, B. B., Bernthal, F. M., Bjørnholm, S., Borggreen, J., Christensen, O., Folkmann, F., Herskind, B., Khoo, T. L., Neiman, M., Puhlhofer, F., Sletten, G. 1977. Phys. Rev. Lett. 39:990

Riedinger, L. L., Andersen, O., Frauendorf, S., Garrett, J. D., Gaardhøje, J. J., Hagemann, G. B., Herskind, B., Makovetsky, Y. V., Waddington, J. C., Guttormsen, M., Tjøm, P. O. 1980. Phys. Rev. Lett. In press

Rud, N., Ward, D., Andrews, H. R., Graham, R. L., Geiger, J. S. 1973. Phys. Rev. Lett. 31:1421

Simon, R. S., Banaschik, M. V., Colombani, P., Soroka, D. P., Stephens, F. S., Diamond, R. M. 1976. Phys. Rev. Lett. 36:359

Simon R. S., Banaschik, M. V., Diamond, R. M., Newton, J. O., Stephens, F. S. 1977. Nucl. Phys. A290:253

Simon, R. S., Diamond, R. M., El Masri, Y., Newton, J. O., Sawa, P., Stephens, F. S. 1979. Nucl. Phys. A313:209

Sorensen, R. A. 1973. Rev. Mod. Phys. 45:353

Strutinsky, V. M. 1966. Yad. Fiz. 3:614. Transl. Sov. J. Nucl. Phys. 3:449

Trautmann, W., Sharpey-Schafer, J. F., Andrew, H. R., Haas, B., Hausser, O., Taras, P., Ward, D. 1979. Phys. Rev. Lett 43:991

Vivien, J. P., Schutz, Y., Beck, F. A., Bozek, E., Byrski, T., Gehringer, C., Merdinger, J. C. 1979. Phys. Lett. 85B:325

Wakai, M., and Faessler, A. 1978. Nucl. Phys. A307:349

Ward, D., Andrews, H. R., Geiger, J. S., Graham, R. L. 1973. Phys. Rev. Lett. 30:493

FIGURE CAPTIONS

Fig. 1. The solid line indicates the angular momentum value for a given mass number A where the fission barrier just vanishes according to the liquid drop model, and the dashed line shows where it is about 8 MeV (Cohen, et al., 1974). The dotted line is an estimate of the boundary between particle evaporation (above) and γ-ray emission (below) estimated from data in Newton, et al. (1977).

Fig. 2. Statistical model calculations for the reaction $^{124}Sn(^{40}Ar,xn)^{164-x}$ Er at 147 MeV as given by Hillis, et al. (1979). The upper plot shows the angular momentum input and excitation energy (53.8 MeV), and those below it show the populations after emission of 1 to 5 neutrons. The shaded regions do not emit more particles, and deexcite by γ-ray emission. The dashed line is the entry line. The side and bottom plots show the correlation of reaction channel with excitation energy and angular momentum, respectively.

Fig. 3. Typical γ-ray deexcitation pathways to the ground state. The statistical transitions are the vertical arrows which lower the temperature of the system, whereas the yrast-like transitions are roughly parallel to the yrast line and remove the angular momentum of the system.

Fig. 4. The left side shows the lowest order estimate for the rigid-body moments of inertia of prolate and oblate shapes rotating about various axes. The right side shows the corresponding energy trajectories for $\beta = 0.3$ and mass number 160.

Fig. 5. Schematic vector diagrams illustrating the strong-coupling scheme (above) and the rotation-aligned coupling scheme (below). The 3 axis is the nuclear symmetry axis, and the vertical axis is taken to be the rotation axis, located in the 1,2 plane.

Fig. 6. Schematic excitation energy vs spin plots for various relative amounts of collective angular momentum and single-particle rotation-aligned angular momentum. Bandhead (pure single-particle) energies are shown in the lower two panels. The solid curves correspond to real bands, whereas the dashed curve is the envelope of the real bands.

Fig. 7. A plot of energy vs I for the ground-band rotational levels in ^{164}Yb. The insert shows the same data in the type of plot generally used to show backbending behavior.

Fig. 8. Typical backbending plots for even-even nuclei in the rare-earth region. The plot is of $2\mathcal{J}/\hbar^2 \approx (4I - 2)/E_\gamma(I)$ vs $(\hbar\omega)^2 \approx (E_\gamma(I)/2)^2$.

Fig. 9. Energy levels of ^{164}Er.

Fig. 10. Plot of the level excitation energies for various bands in ^{164}Er from (a) experiment and (b) the rotation-alignment model. The solid circles correspond to even-spin states and the open circles to odd-spin states.

Fig. 11. Plot of $2\mathcal{J}/\hbar^2$ vs $(\hbar\omega)^2$ for members of the ground-state band, β-vibrational band and superbands in ^{164}Er. The open circles on the ground-state and even-yrast superbands are corrections for a 45-keV interaction matrix element. The energies of the 10^+_γ and 12^+_γ states were adjusted in accord with this interaction strength. The circles represent even-spin and the squares odd-spin states.

Fig. 12. Conventional backbending plots for ^{156,158}Er, and for the decoupled band in ^{157}Er. The following expressions have been used: $2\mathcal{J}/\hbar^2 = (4I' - 2)/(E_I - E_{I-2})$ and $\hbar\omega = (E_I - E_{I-2})/2$, where $I' = I$ for the even-even nuclei and $I' = I - j$ for the decoupled band in the odd-mass nucleus.

Fig. 13. A comparison of backbending in ^{157,159,161}Ho with their even-even neighbors. The even-even curves are the usual ones of this type, and the odd-mass bands are treated as described in Fig. 12.

Fig. 14. Coincidence spectra and highest observed rotational levels of ^{158}Er.

Fig. 15. Backbending plot for ^{158}Er showing the first backbend at $(\hbar\omega)^2 \approx 0.08$ and the second backbend (upbend) at $(\hbar\omega)^2 \approx 0.18$.

Fig. 16. Energy levels as a function of prolate deformation for protons in the range $50 \leq Z \leq 82$, calculated by Gustafson, et al. (1967) using the MHO potential.

Fig. 17. Energy levels as a function of rotational frequency for protons in a prolate nucleus having $\varepsilon = 0.2$ and mass number 165 as calculated by Andersson, et al. (1976) using the MHO potential. The solid and dashed lines correspond to states having different symmetry with respect to $e^{i\pi j_x}$ (different "signatures").

Fig. 18. Cranking model calculations of energy in the rotating frame, $e'(\omega)$ vs ω for neutrons around N = 90. The levels marked A, B, C, and D are components of the $i_{13/2}$ orbital, while those labelled E, F, G, and H have negative parity (N = 5 shell). The different types of lines refer to different signatures of the levels. The figure is from Riedinger, et al. (1980).

Fig. 19. Plot of alignment, i, vs ω for bands in ^{160}Yb and ^{161}Yb. The proposed labeling of the bands is according to the nomenclature on Fig. 18. Taken from Riedinger, et al. (1980).

Fig. 20. Level scheme for ^{212}Rn [including the unobserved transition $\Delta = E(22^+) - E(20^+)$]. Energies are in keV (Horn, et al., 1977).

Fig. 21. Plot of energy vs $I(I + 1)$ for the yrast levels of ^{212}Rn. The dashed line is drawn through points above 20$\hbar$, with the rigid-body slope.

Fig. 22. Partial level scheme for ^{176}Hf showing high-spin bandheads (Khoo, et al., 1976).

Fig. 23. Region of Periodic Table searched for high-spin isomeric states. Compound systems formed via ^{40}Ar, ^{50}Ti, and ^{65}Cu beams are indicated as dashed squares. Systems with positive results have filled squares. The final nuclei probably have 3-5 fewer neutrons (Pedersen, et al., 1977).

Fig. 24. Level scheme for ^{152}Dy (Haas, et al., 1979).

Fig. 25. Plot of energy vs I(I + 1) for yrast levels of ^{152}Dy assuming I = 17 for the 60 ns isomer. For I > 14, the data lie close to a straight line with slope corresponding to $2\mathcal{J}/\hbar^2$ = 142 MeV^{-1} (Khoo, et al., 1978).

Fig. 26. Plot of energy vs I^2 for the yrast levels of nuclei with the indicated neutron number as calculated with a rotating spherical Nilsson potential [L. G. Moretto, unpublished work (1979)].

Fig. 27. Schematic energy level spectrum of a rotor on the left, and its γ-ray spectrum on the right. Each vertical line on this spectrum represents a transition between adjacent rotational levels.

Fig. 28. Sodium iodide pulse-height (squares) and unfolded (black dots) γ-ray spectra (0° + 45° + 90°) from the reaction ^{126}Te(^{40}Ar,4n)^{162}Yb at 181 MeV. The larger dots are averaged over five channels. At the top is the 0°/90° ratio for the unfolded spectra. At the bottom are schematic unfolded spectra for the same case (solid line) and for ^{80}Se(^{86}Kr,4n)^{162}Yb at 331 meV (dotted line), ^{126}Te(^{40}Ar,4n)^{162}Yb at 157 MeV (longer dashed line), and ^{150}Sm(^{16}O,4n)^{162}Yb at 87 MeV (shorter-dashed line) (Simon, et al., 1977).

Fig. 29. Plots of multipole spectra vs γ-ray transition energy for stretched quadrupole (full lines) and stretched dipole (dotted lines) components for the principal product nuclei shown by symbol in the section of the Periodic Table given as an insert. These spectra were determined from the unfolded spectra of 7.6 x 7.6 cm NaI detectors

placed at 0°, 45°, 90° to the beam. A multiplicity filter of six additional NaI counters arranged in a vertical plane helped select nuclei aligned along a particular axis, (Deleplanque, et al., 1978a).

Fig. 30. (a) Pulse-height spectra at 0° for a self-supporting (solid curve) and for a gold-backed (dotted curve) ^{27}Al target irradiated by ^{136}Xe to give $^{163}Ho^{*}$. (b) Ratio of the two spectra in (a). (c) Ratios of the unfolded spectra from (a) are given as dots. The solid curve represents the best fit of the calculated ratios (see text) to the data, giving an average B(E2) value of 270 ± 100 single-particle units. The dashed lines show these error limits (Hubel, et al., 1978).

Fig. 31. Observed (left) and calculated (right) multiplicity spectra vs E_γ for the ^{124}Sn + ^{40}Ar system at the indicated bombarding energies. One NaI γ-ray spectrum is also shown (Deleplanque, et al., 1978b).

Fig. 32. (Top) Spectra from a 7.6 cm x 7.6 cm NaI detector (number of transitions per 200 keV per event) for consecutive ~4 MeV wide slices of the coincident total γ-ray energy spectrum from 185 MeV ^{40}Ar + $^{124}Sn \rightarrow {}^{164}Er^{*}$ observed with a 33 cm x 20 cm sum crystal. (Bottom) The difference in spectra from neighboring slices as indicated in the figure (Körner, et al., 1979).

Fig. 33. Plot of $2\mathcal{J}/\hbar^2$ vs $(\hbar\omega)^2$ for the compound system $^{164}Er^{*}$ made by ^{40}Ar + ^{124}Sn. The solid circles to spin 32ħ are the known transitions in ^{158}Er. The symbols without error bars are calculated from the expression $2\mathcal{J}/\hbar^2 = 8/\Delta E_\gamma$. The pure liquid-drop prediction is indicated by the dashed line.

Fig. 34. Schematic correlation plot for a rotational nucleus. The dots locate the coincidences for a band with spins up to 14ħ and moment of inertia $\mathcal{J}$, and the heavy lines show the effect of bands where $\mathcal{J}$ differs by ±10 percent. The crosses show the location of coincidences in a band with spins 16 to 26ħ, 11ħ of aligned angular momentum, and moment of inertia $\mathcal{J}$. The light lines again show the effect of bands differing in $\mathcal{J}$ by 10 percent.

Fig. 35. Correlation spectrum from the reaction $^{124}Sn(^{40}Ar,xn)^{164-x}Er$ at 185 MeV. The data were taken on GeLi detectors and treated according to Eq. 26. The plot shows contours of equal numbers of correlated events, where the darker regions have more counts according to the scale at the right edge. These data are from Deleplanque, et al. (1980).

Fig. 36. Schematic illustration of the bands in a decay pathway (solid lines) and their envelope (dashed line). The plot parameters are somewhat arbitrary but were taken to be $2\mathcal{J}_{coll}/\hbar^2 = 50\ MeV^{-1}$, $2\mathcal{J}_{eff}/\hbar^2 = 100\ MeV^{-1}$; $j_a = 0$, 10, 18, and 24ħ for the bands, in order of increasing energy.

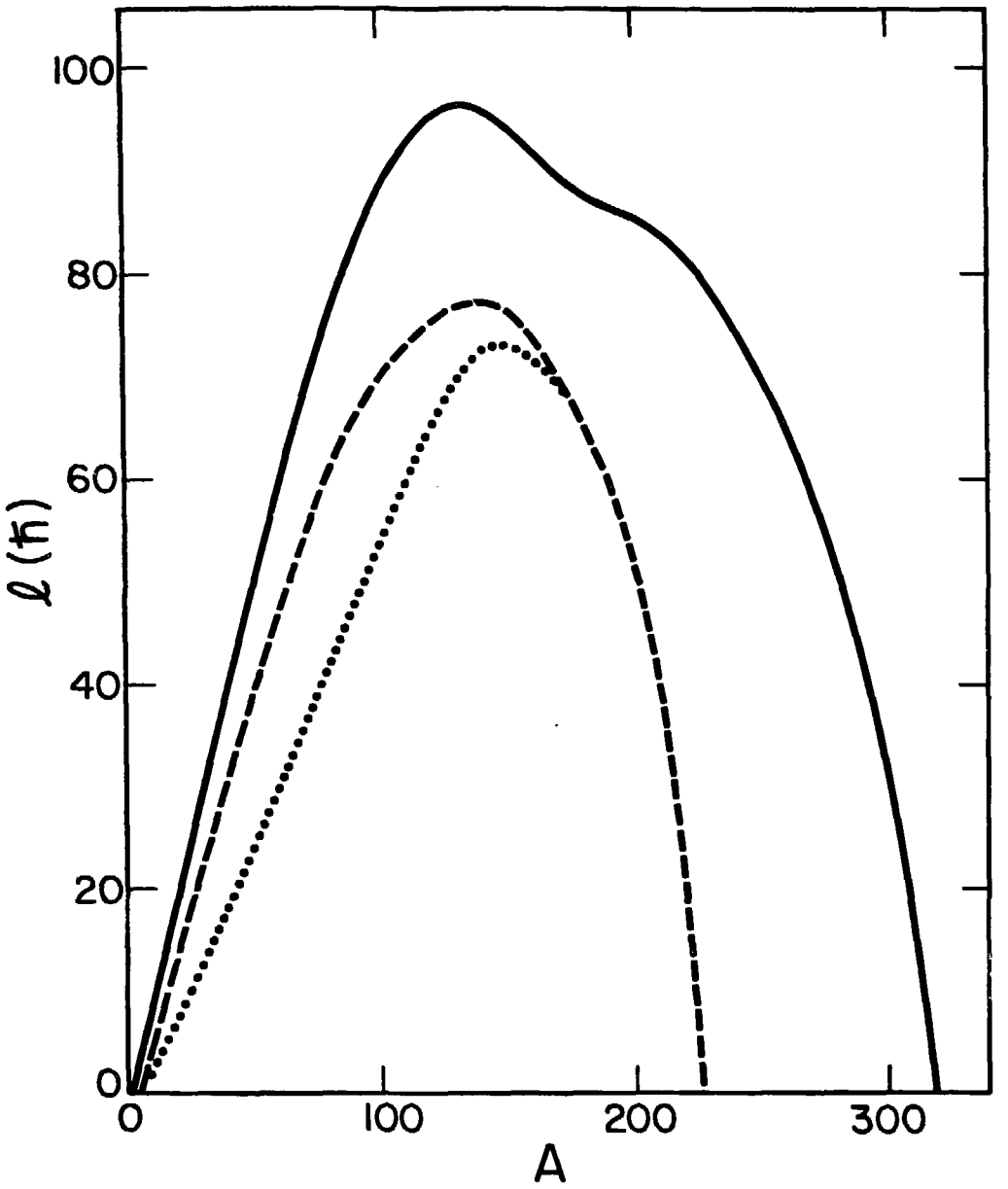

Fig. 1

STATISTICAL MODEL CALCULATIONS

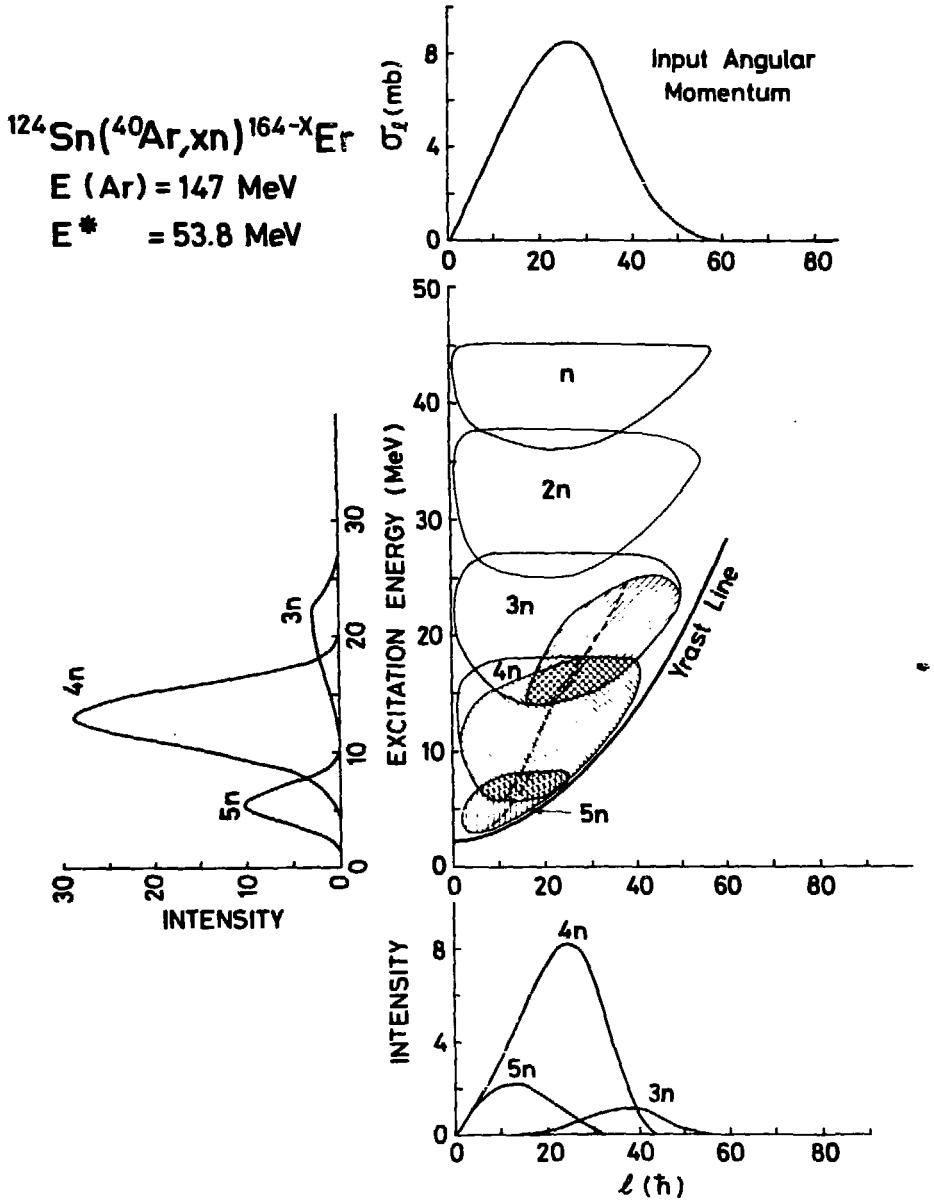

XBL 804-9161

Fig. 2

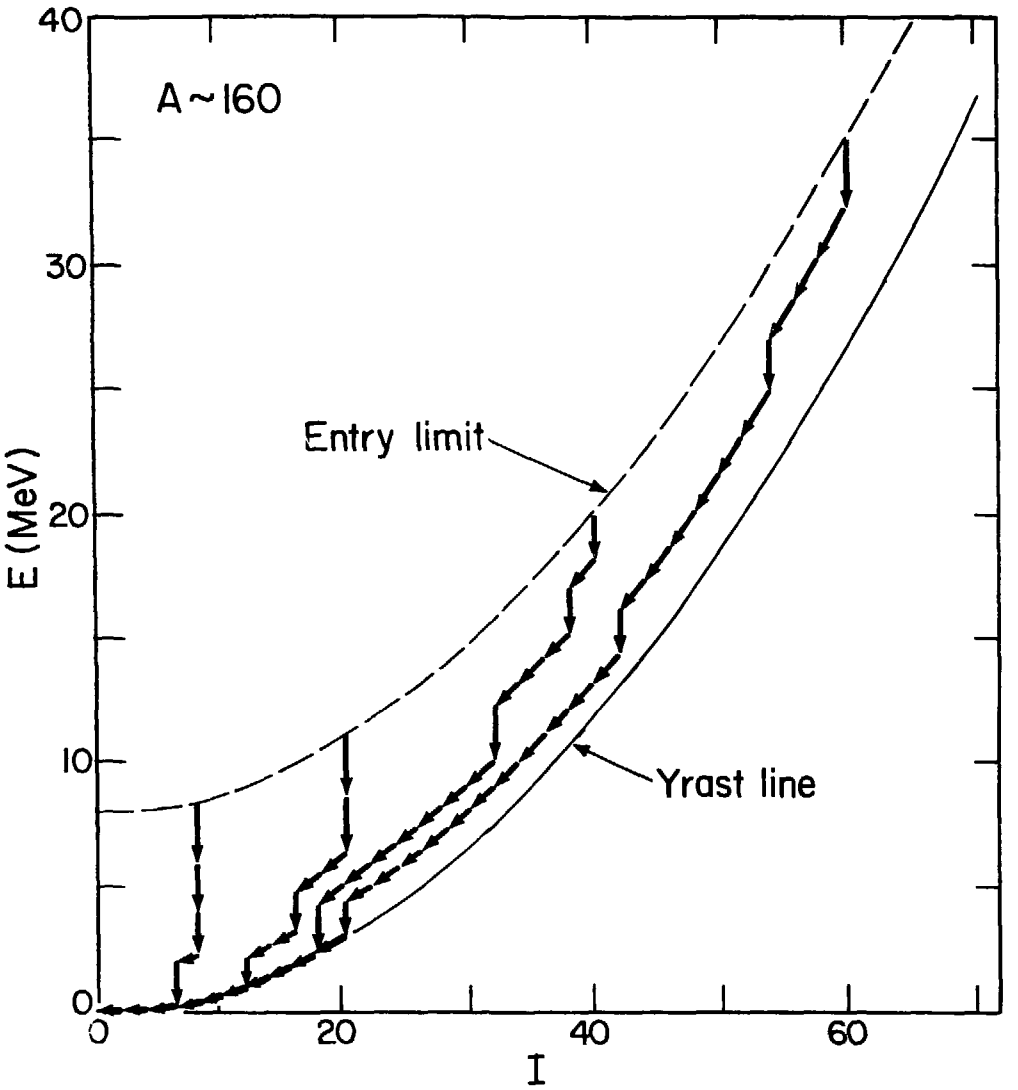

XBL 803-501

Fig. 3

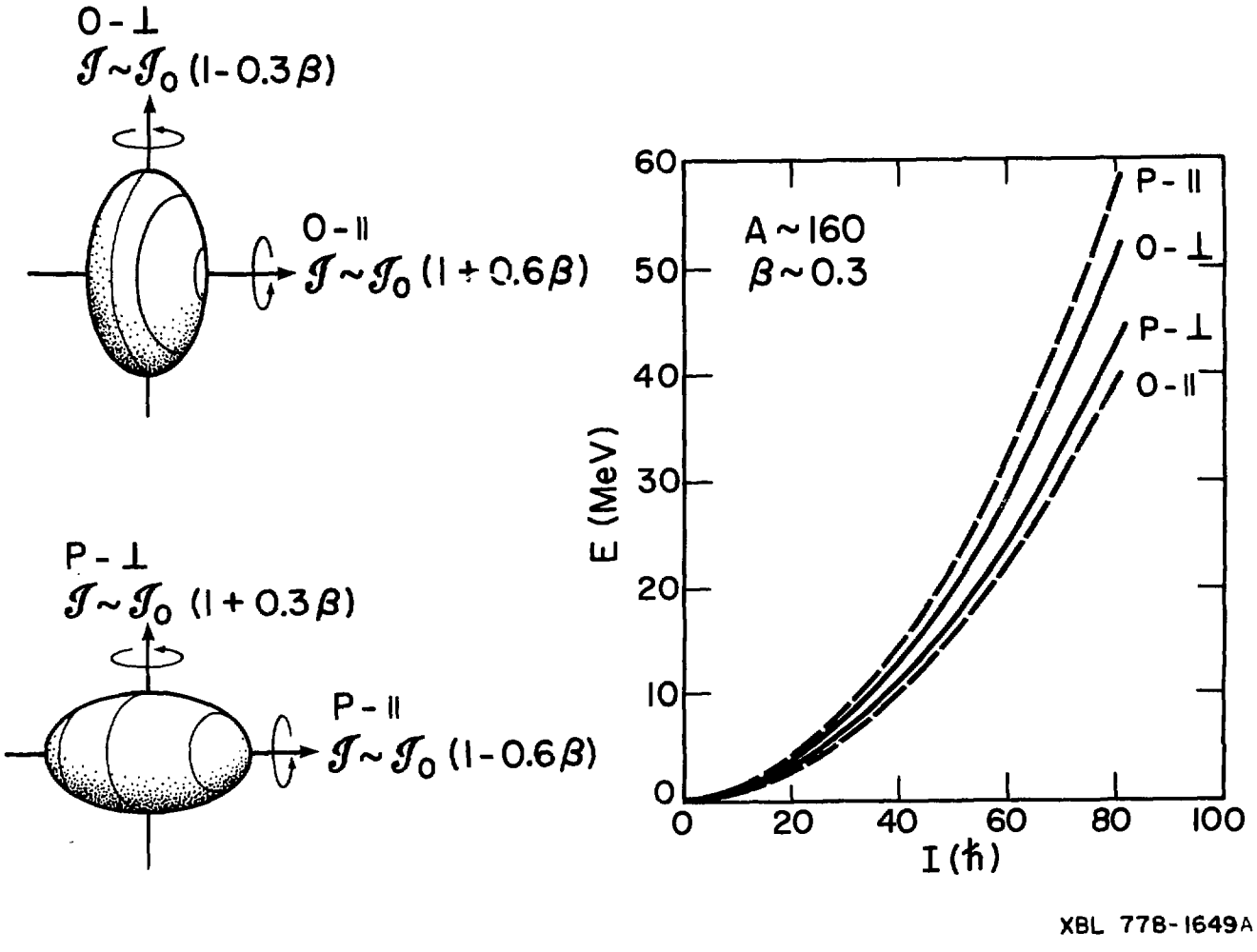

XBL 778-1649A

Fig. 4

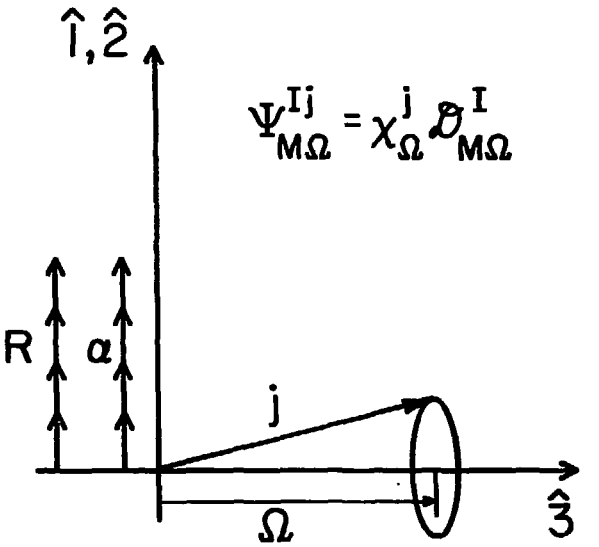

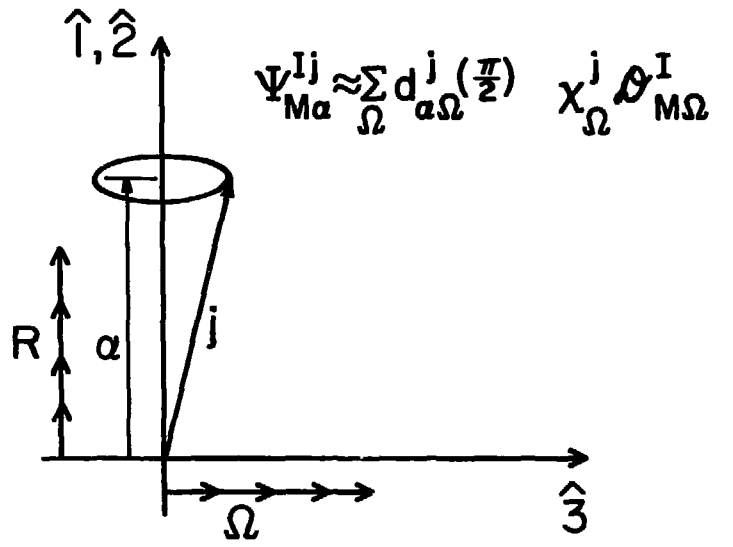

XBL737-3533

Fig. 5

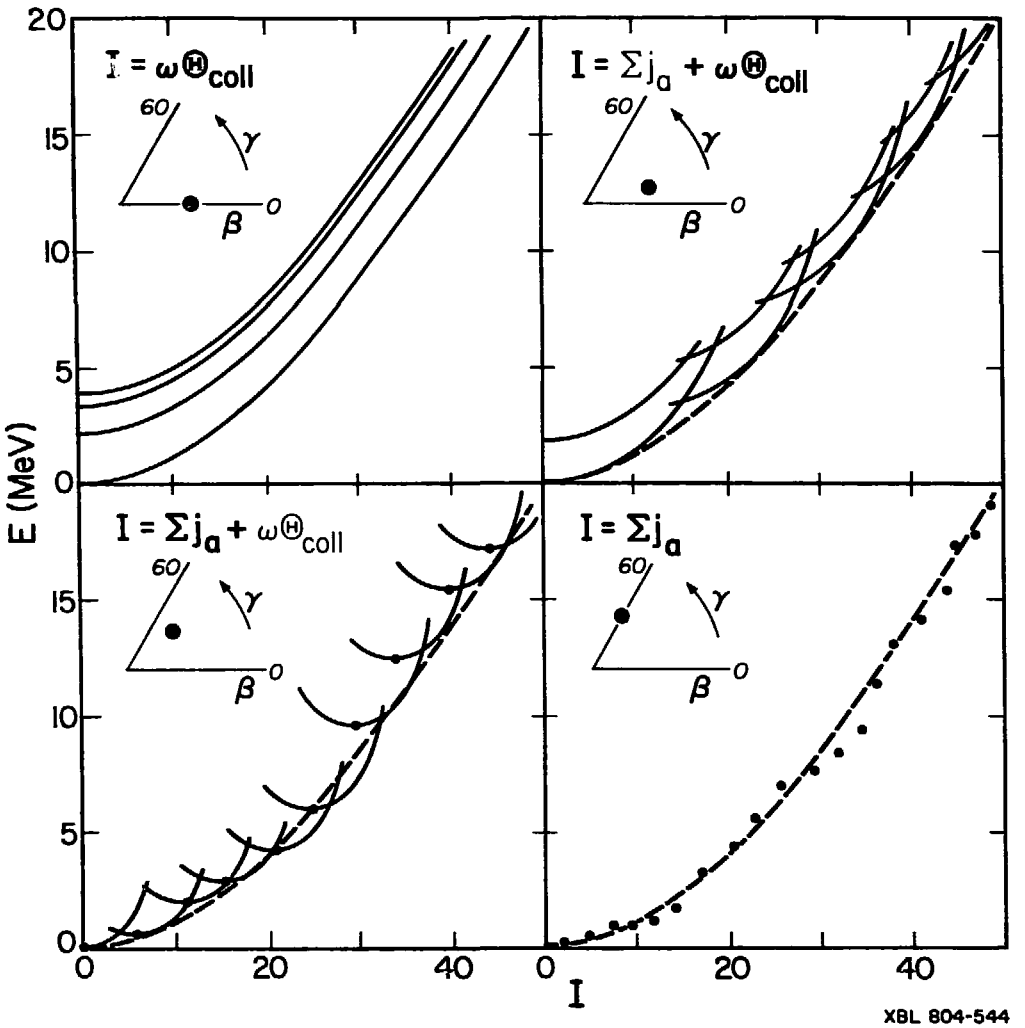
I = ω Θcoll
I = Σja + ω Θcoll
I = Σja + ω Θcoll
I = Σja
60
γ
β
0
E (MeV)
I
0
5
10
15
20
40
XBL 804-544

Fig. 6

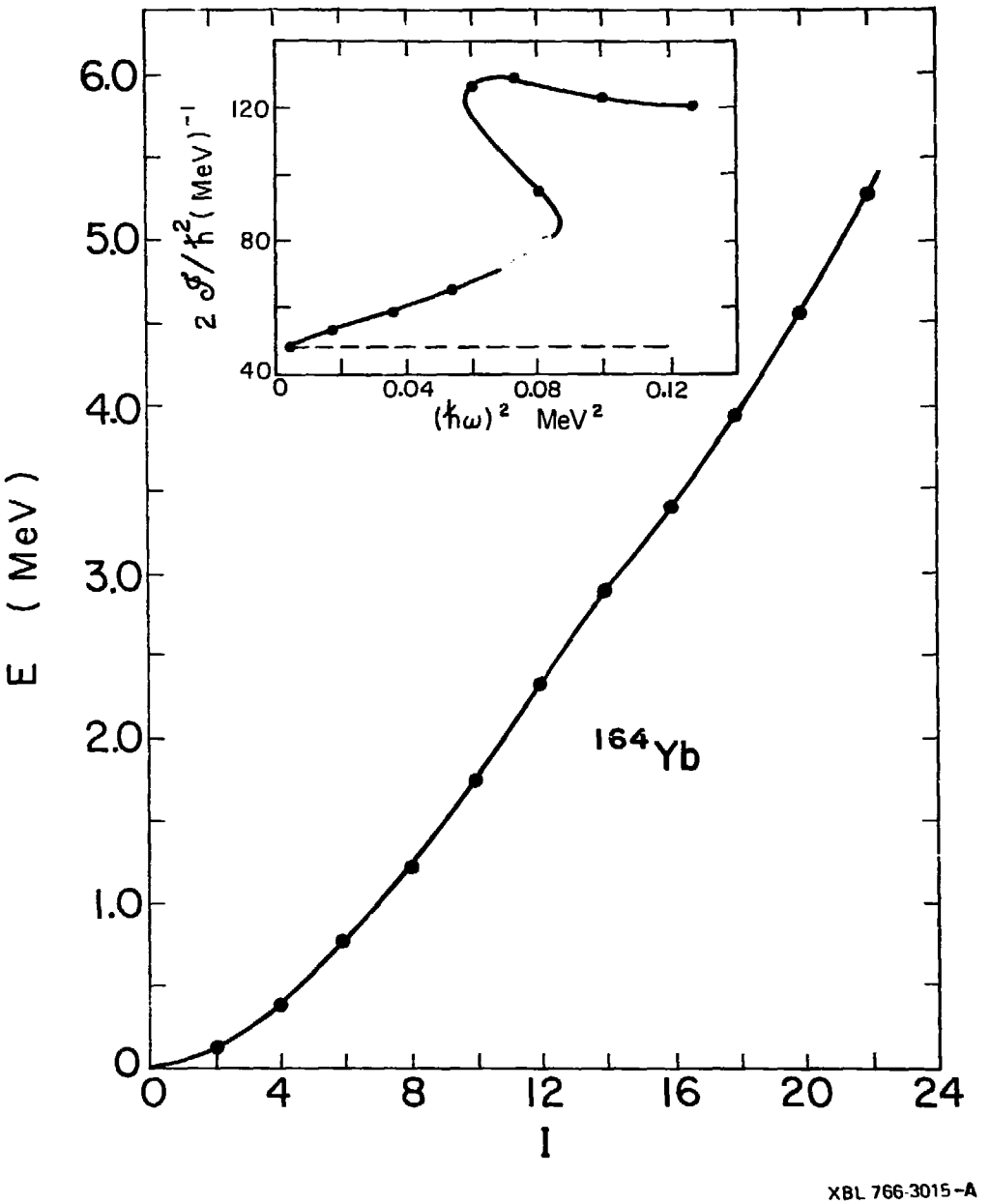
E (MeV)
I
^{164}Yb
2 $\mathcal{J}/\hbar^2$ (MeV)$^{-1}$
$(\hbar\omega)^2$ MeV^2
XBL 766-3015-A

Fig. 7

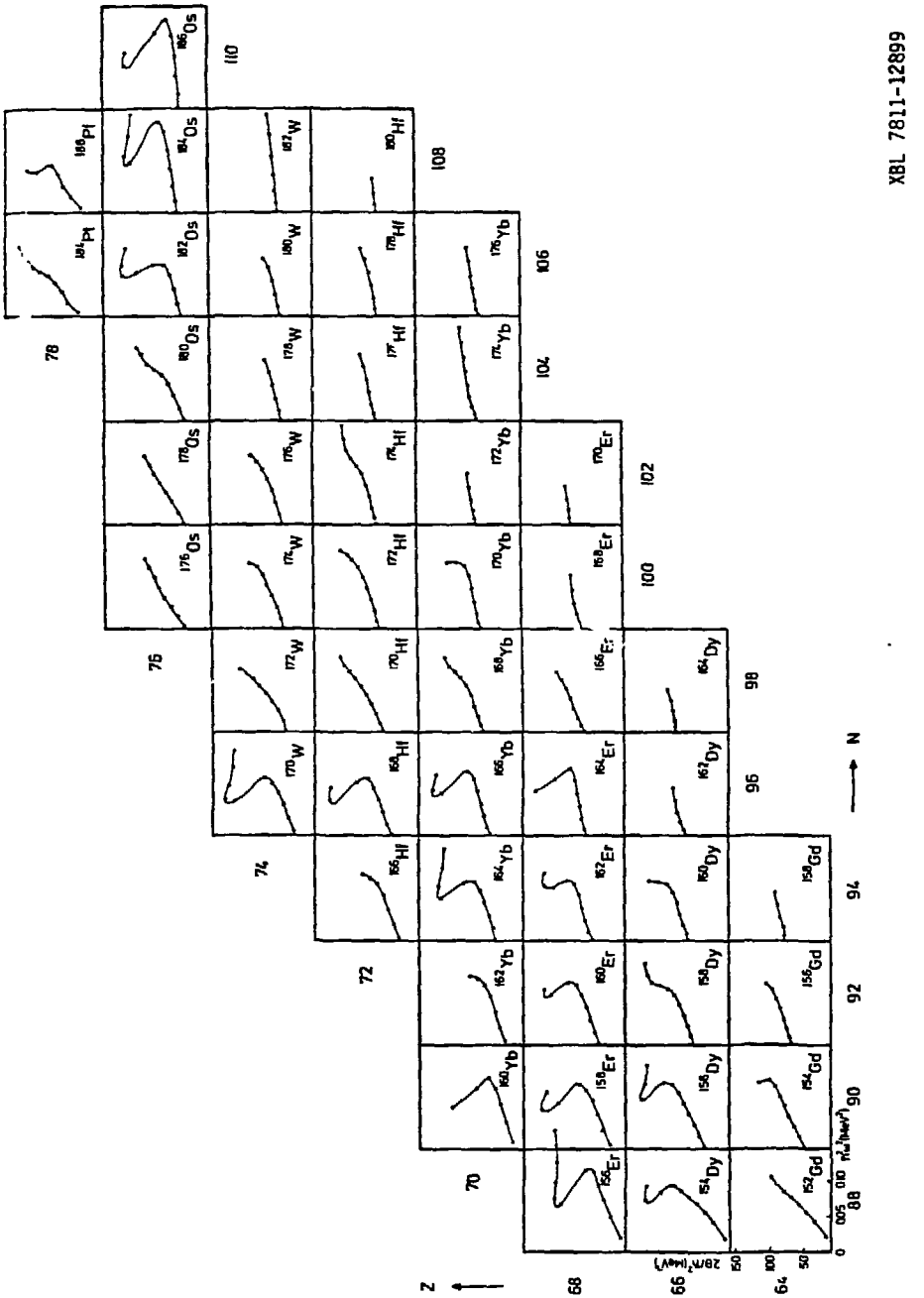

XBL 7811-12899

Fig. 8

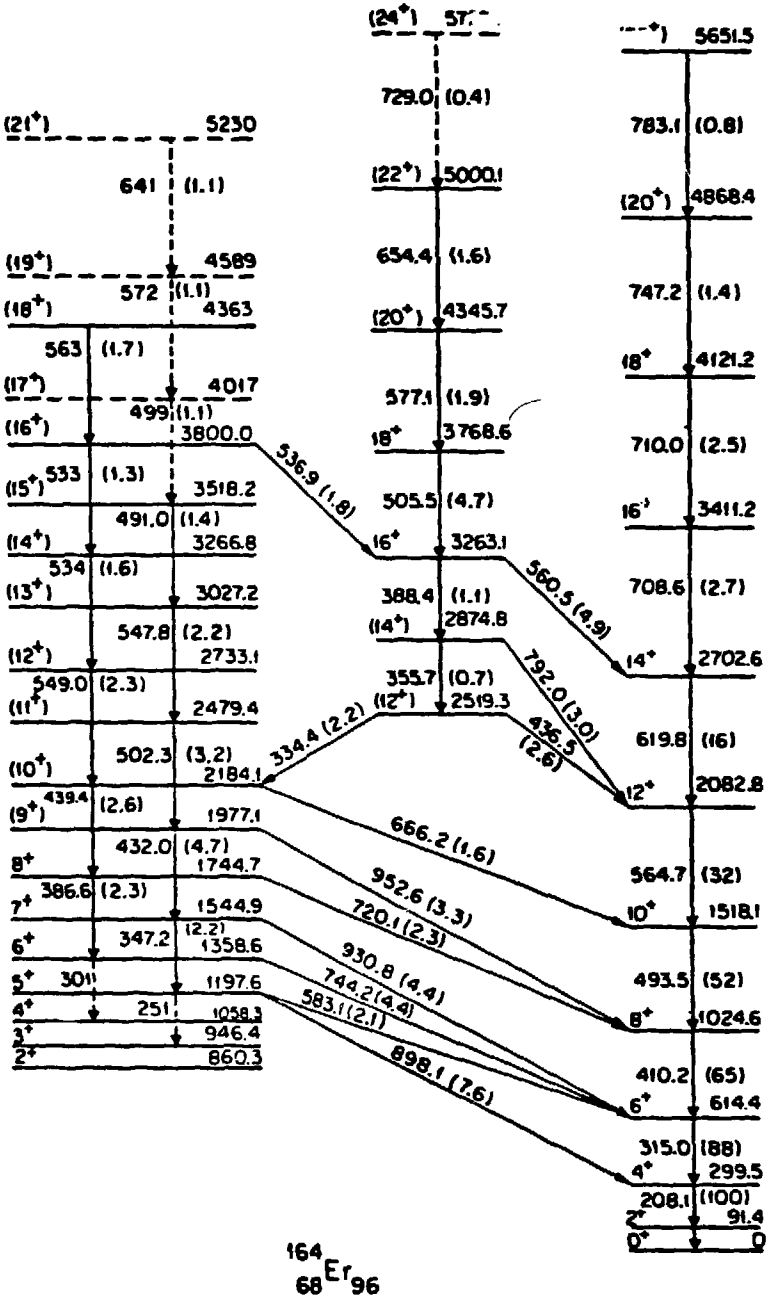
(24+) 57
729.0 (0.4)
(22+) 5000.1
654.4 (1.6)
(20+) 4345.7
577.1 (1.9)
18+ 3768.6
505.5 (4.7)
16+ 3263.1
388.4 (1.1)
(14+) 2874.8
355.7 (0.7)
(12+) 2519.3
334.4 (2.2)
2184.1
(21+) 5230
641 (1.1)
(19+) 4589
572 (1.1)
(18+) 4363
563 (1.7)
(17+) 4017
499 (1.1)
(16+) 3800.0
536.9 (1.8)
(15+) 533 (1.3) 3518.2
491.0 (1.4)
(14+) 3266.8
534 (1.6)
(13+) 3027.2
547.8 (2.2)
(12+) 2733.1
549.0 (2.3)
(11+) 2479.4
502.3 (3.2)
(10+)
(9+) 439.4 (2.6) 1977.1
432.0 (4.7)
8+ 1744.7
7+ 386.6 (2.3) 1544.9
6+ 347.2 (2.2) 1358.6
5+ 301 1197.6
4+ 251 1058.3
3+ 946.4
2+ 860.3
560.5 (4.9)
792.0 (3.0)
436.3 (2.6)
666.2 (1.6)
952.6 (3.3)
720.1 (2.3)
930.8 (4.4)
744.2 (4.4)
583.1 (2.1)
898.1 (7.6)
---+) 5651.5
783.1 (0.8)
(20+) 4868.4
747.2 (1.4)
18+ 4121.2
710.0 (2.5)
16+ 3411.2
708.6 (2.7)
14+ 2702.6
619.8 (16)
12+ 2082.8
564.7 (32)
10+ 1518.1
493.5 (52)
8+ 1024.6
410.2 (65)
6+ 614.4
315.0 (88)
4+ 299.5
208.1 (100)
2+ 91.4
0+ 0
164 68 Er 96
XBL 7811-12919

Fig. 9

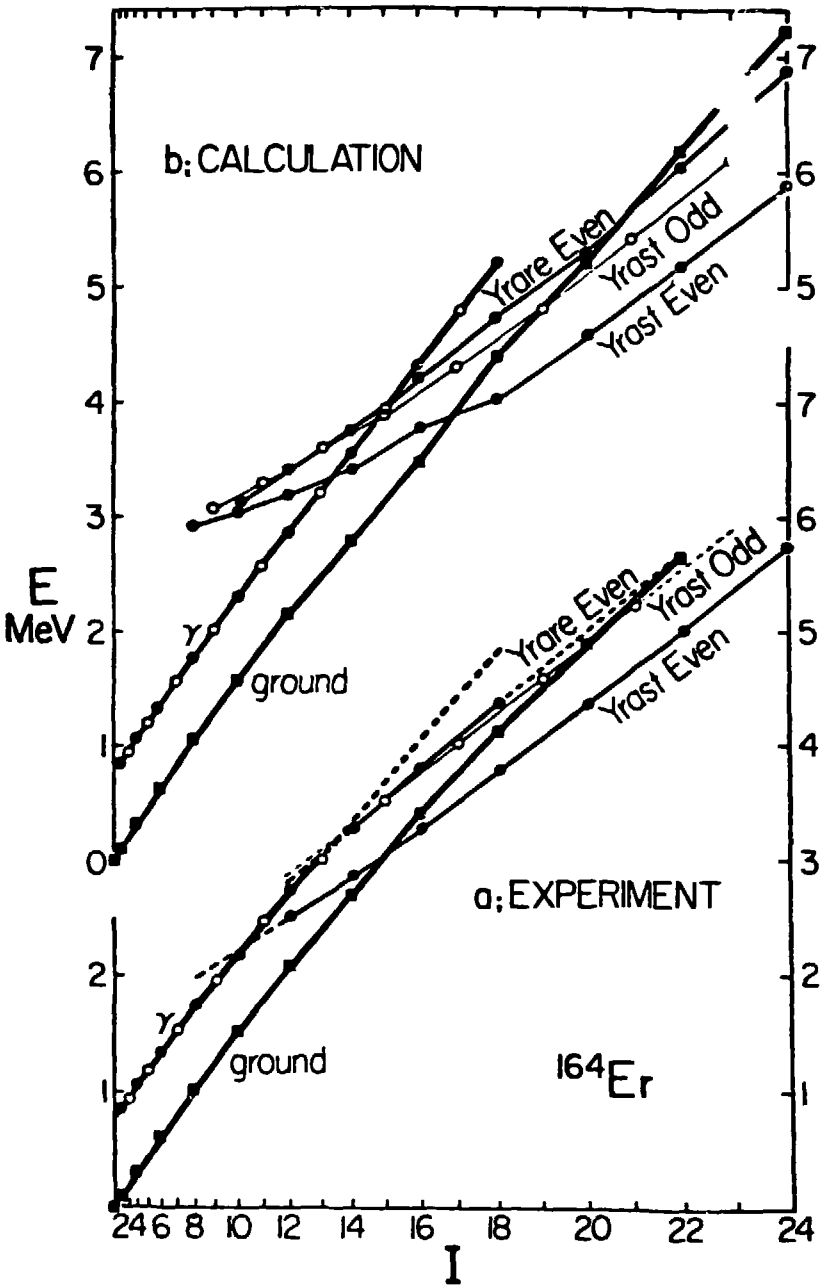
b; CALCULATION
Yrare Even
Yrast Odd
Yrast Even
γ
ground
E
MeV
a; EXPERIMENT
Yrare Even
Yrast Odd
Yrast Even
γ
ground
164Er
I
XBL 7811-12920

Fig. 10

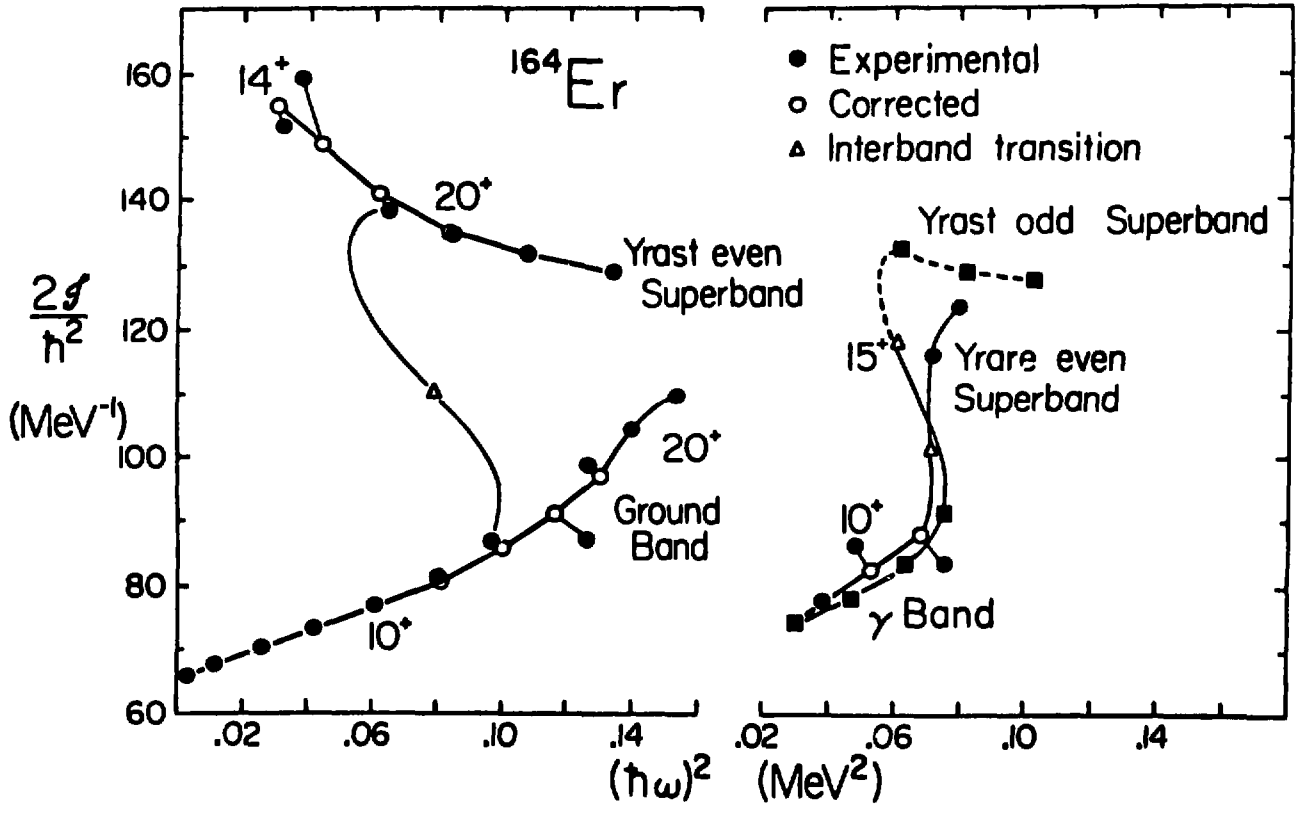

XBL 806-9889

Fig. 11

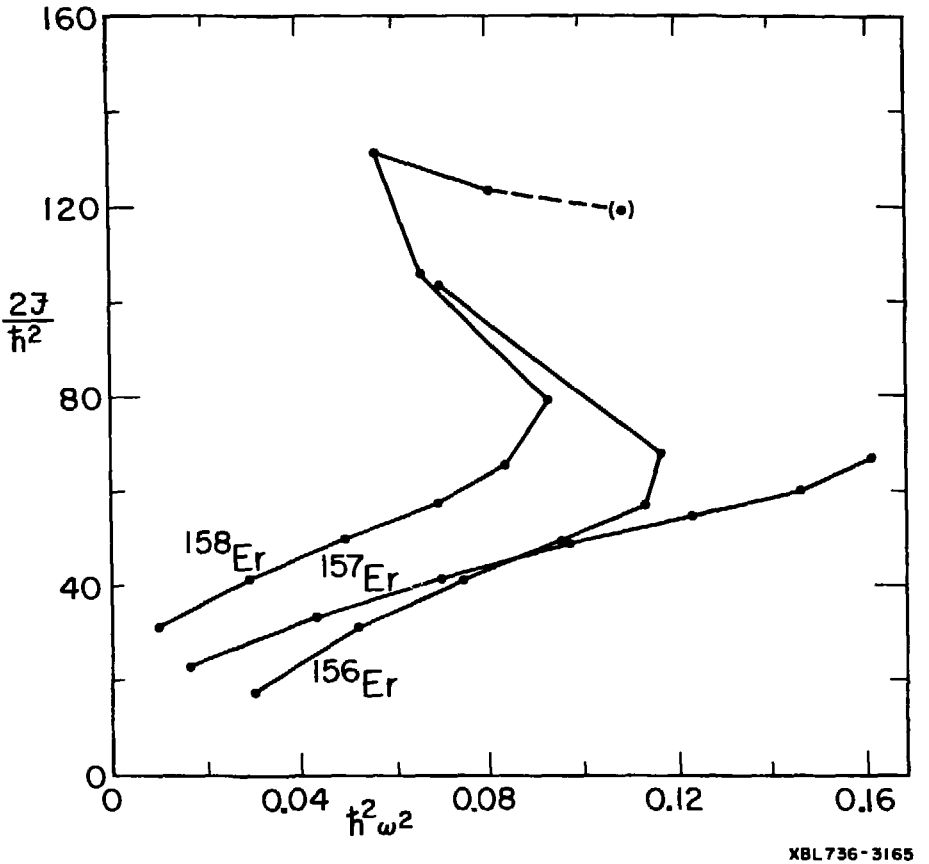
160
120
80
40
0
$\frac{2\mathcal{J}}{\hbar^2}$
0
0.04
0.08
0.12
0.16
$\hbar^2\omega^2$
(•)
^{158}Er
^{157}Er
^{156}Er
XBL736-3165

Fig. 12

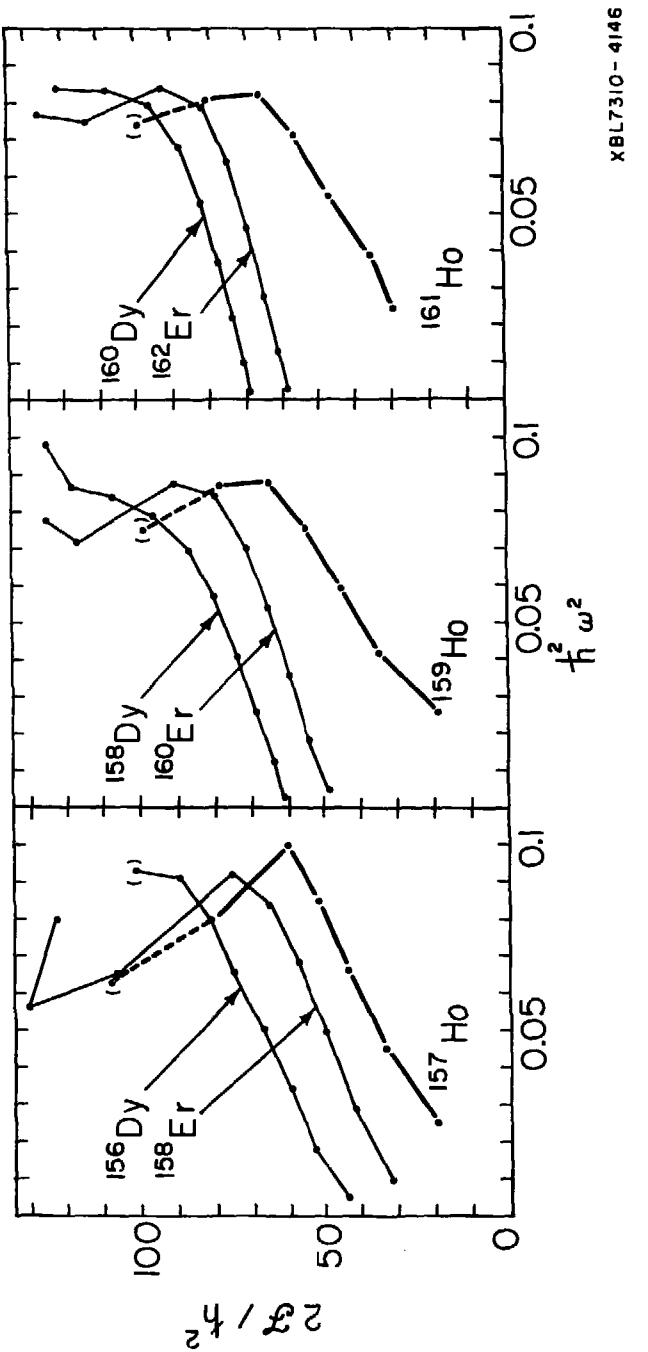
$2\mathcal{J}/\hbar^2$
100
50
0
0.05
0.1
$\hbar^2\omega^2$
^{156}Dy
^{158}Er
^{157}Ho
^{158}Dy
^{160}Er
^{159}Ho
^{160}Dy
^{162}Er
^{161}Ho
XBL7310-4146

Fig. 13

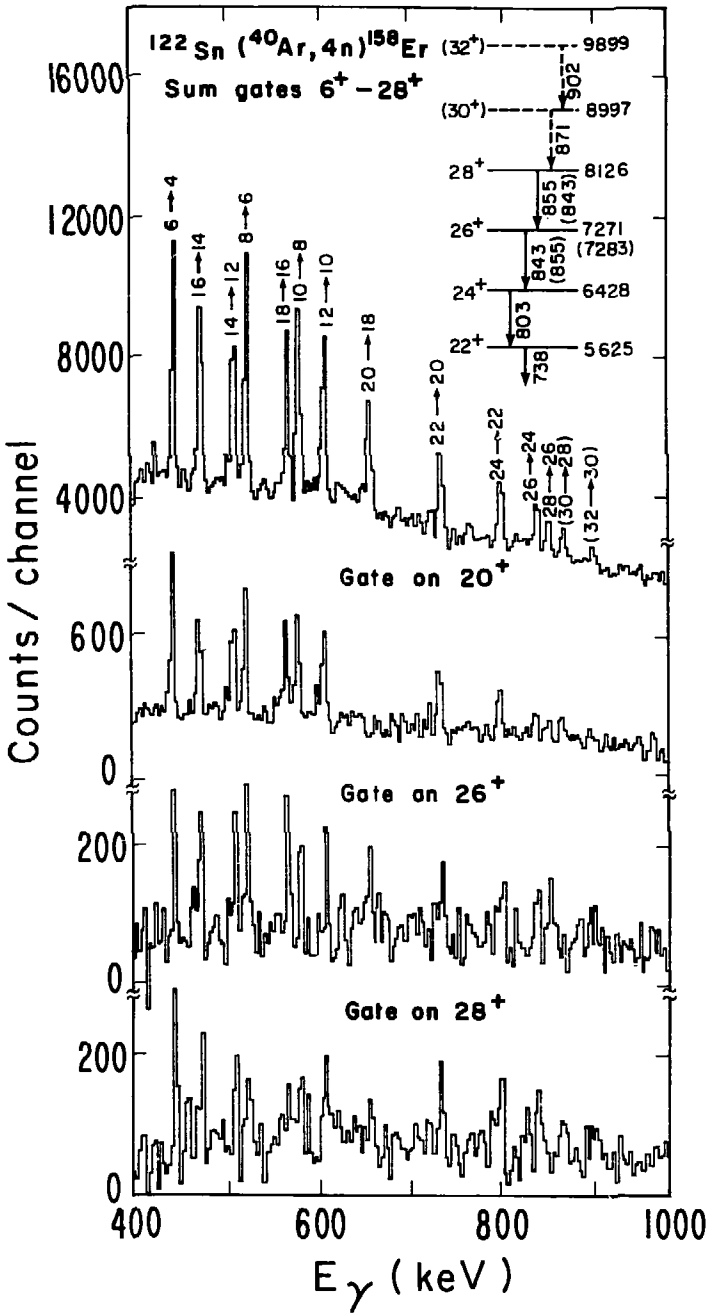

XBL774-805

Fig. 14

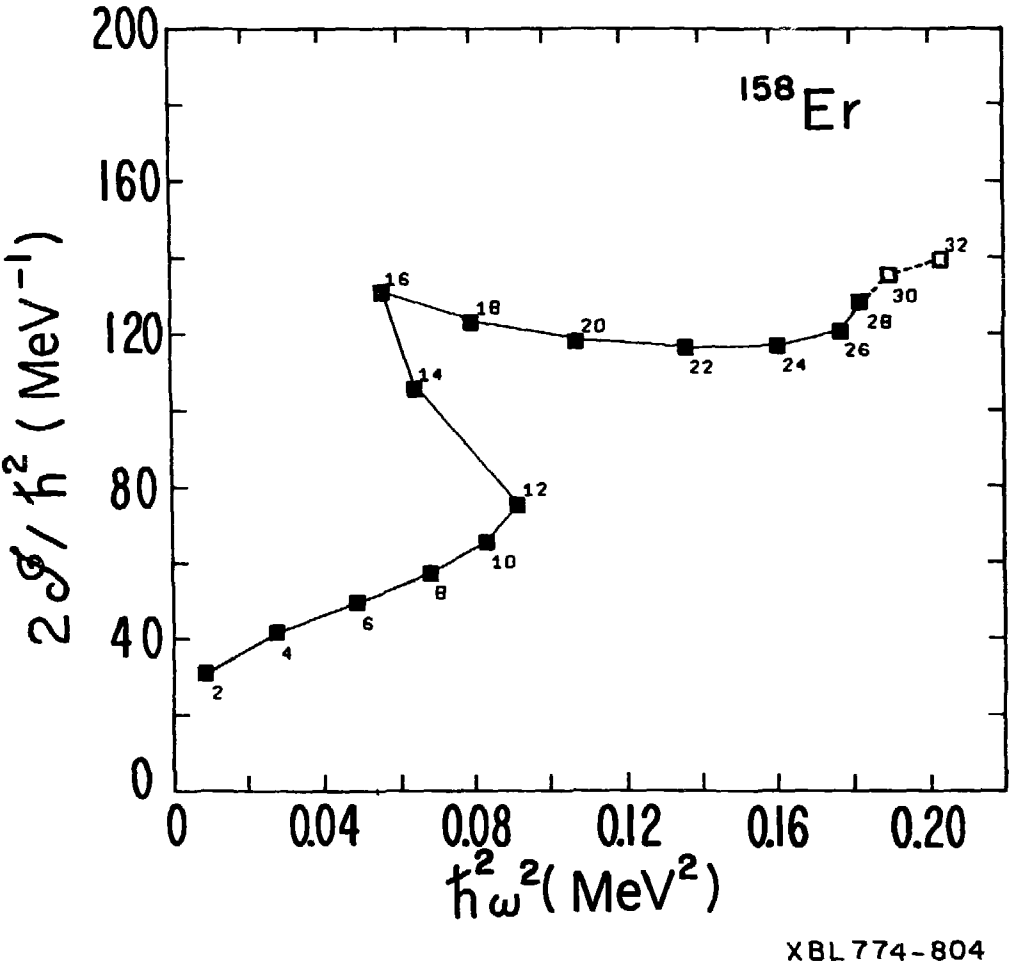
158Er
200
160
120
80
40
0
0
0.04
0.08
0.12
0.16
0.20
2ℐ/ħ² (MeV⁻¹)
ħ²ω² (MeV²)
2
4
6
8
10
12
14
16
18
20
22
24
26
28
30
32
XBL 774-804

Fig. 15

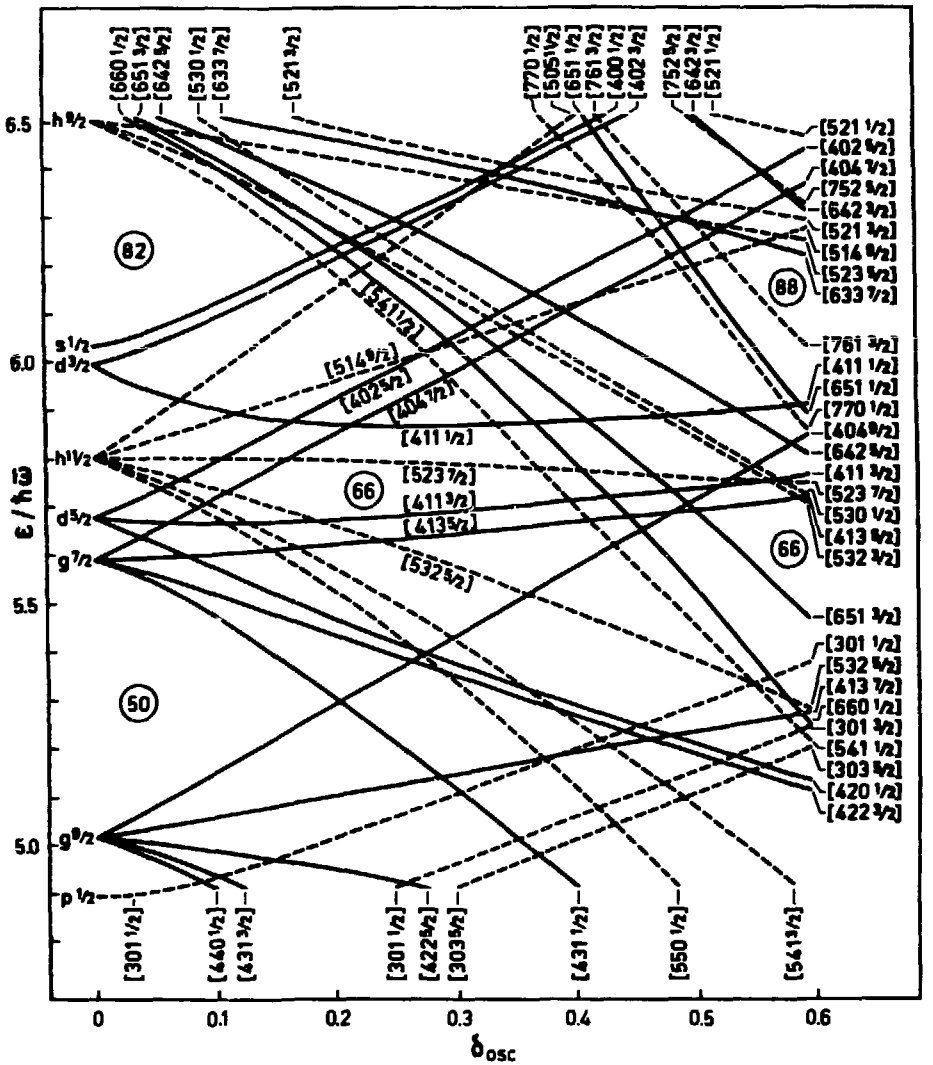

XBL 763-648

Fig. 16

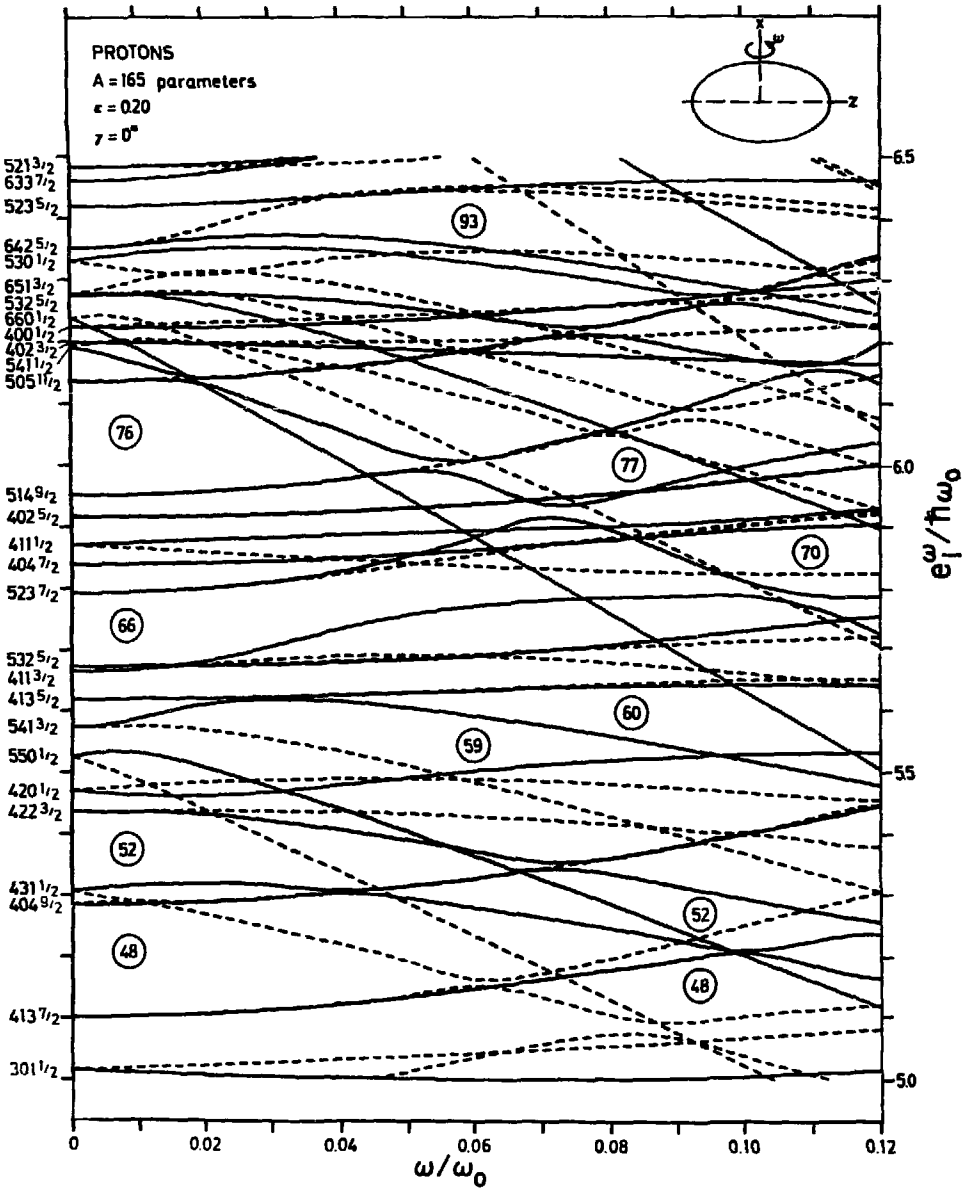
PROTONS
A = 165 parameters
ε = 0.20
γ = 0°
x
ω
z
521 3/2
633 7/2
523 5/2
642 5/2
530 1/2
651 3/2
532 5/2
660 1/2
400 1/2
402 3/2
541 1/2
505 11/2
514 9/2
402 5/2
411 1/2
404 7/2
523 7/2
532 5/2
411 3/2
413 5/2
541 3/2
550 1/2
420 1/2
422 3/2
431 1/2
404 9/2
413 7/2
301 1/2
93
76
77
70
66
60
59
52
52
48
48
6.5
6.0
5.5
5.0
0
0.02
0.04
0.06
0.08
0.10
0.12
ω/ω0
e_i^ω/ħω0
XBL 806-9888

Fig. 17

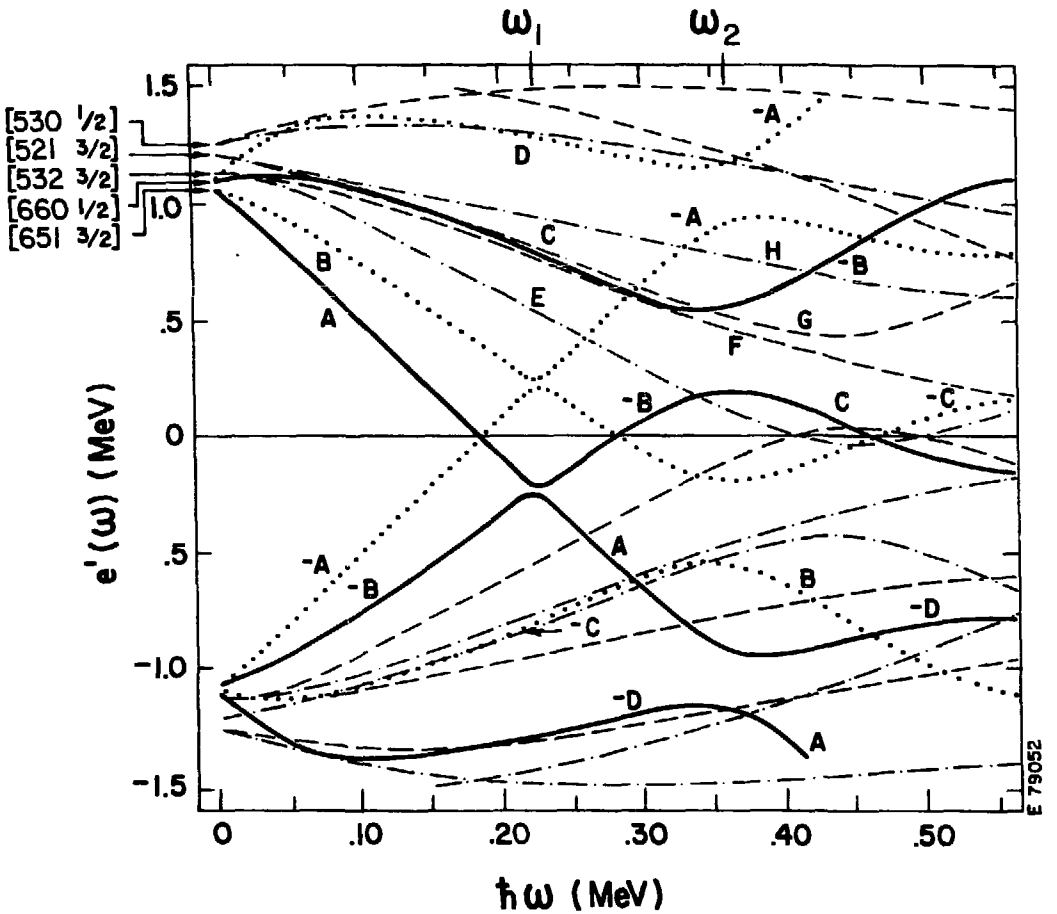

XBL 8.6-9886

Fig. 18

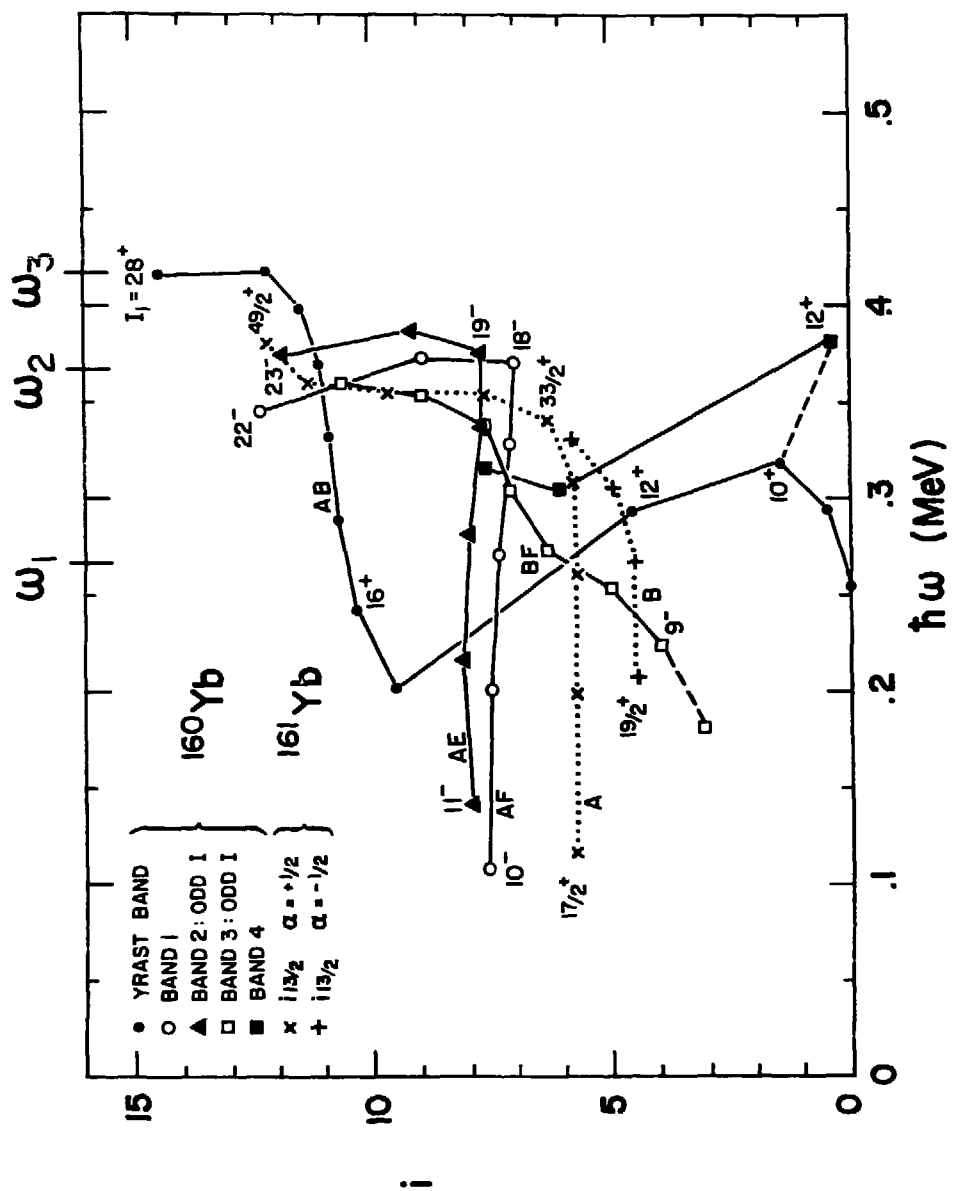

XBL 804-9229

Fig. 19

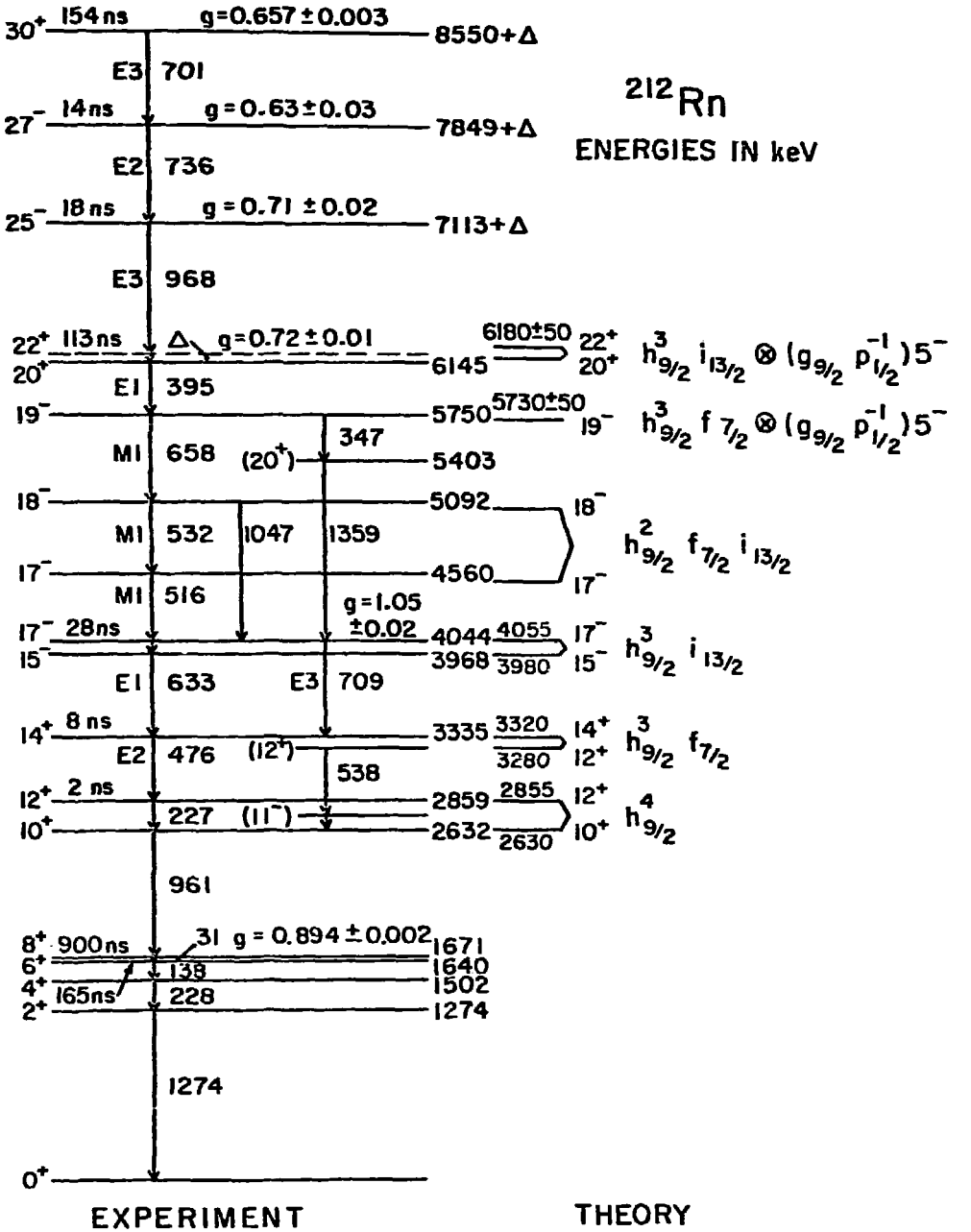

XBL 788-10150

Fig. 20

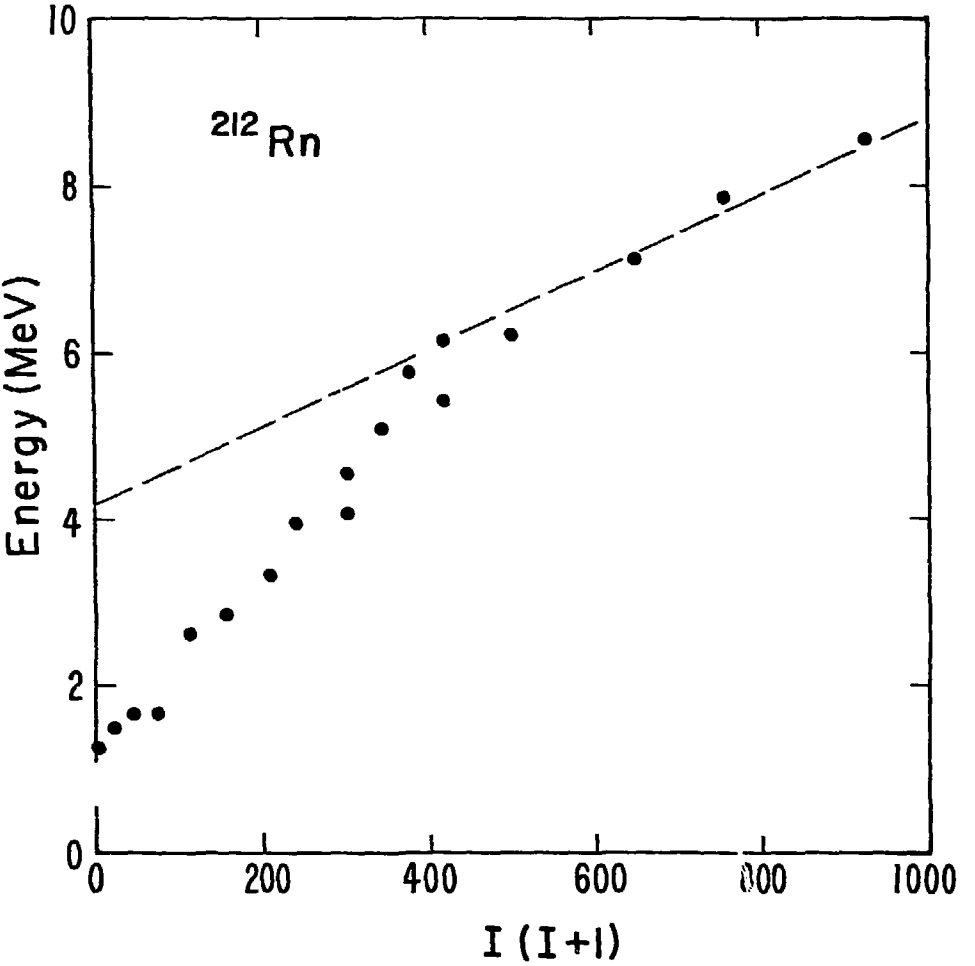

XBL 738-2643A

Fig. 21

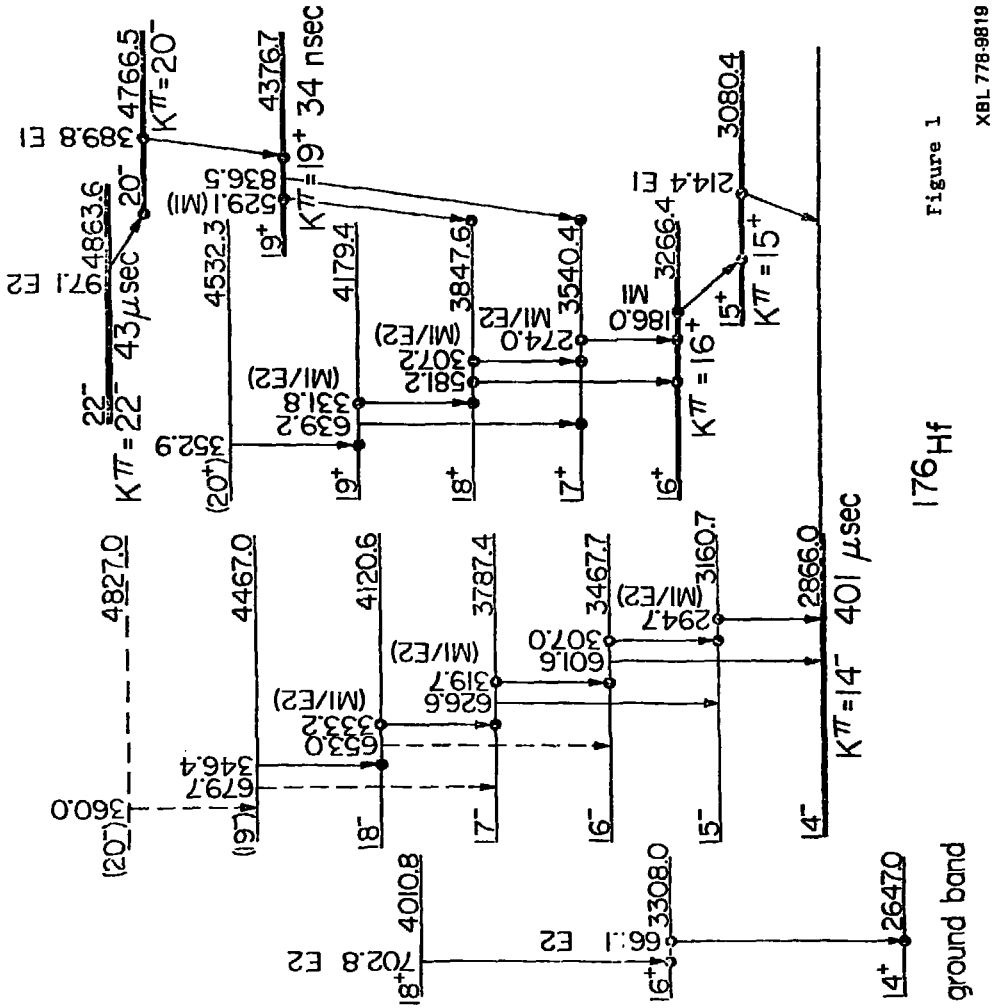

Figure 1

XBL 778-9819

Fig. 22

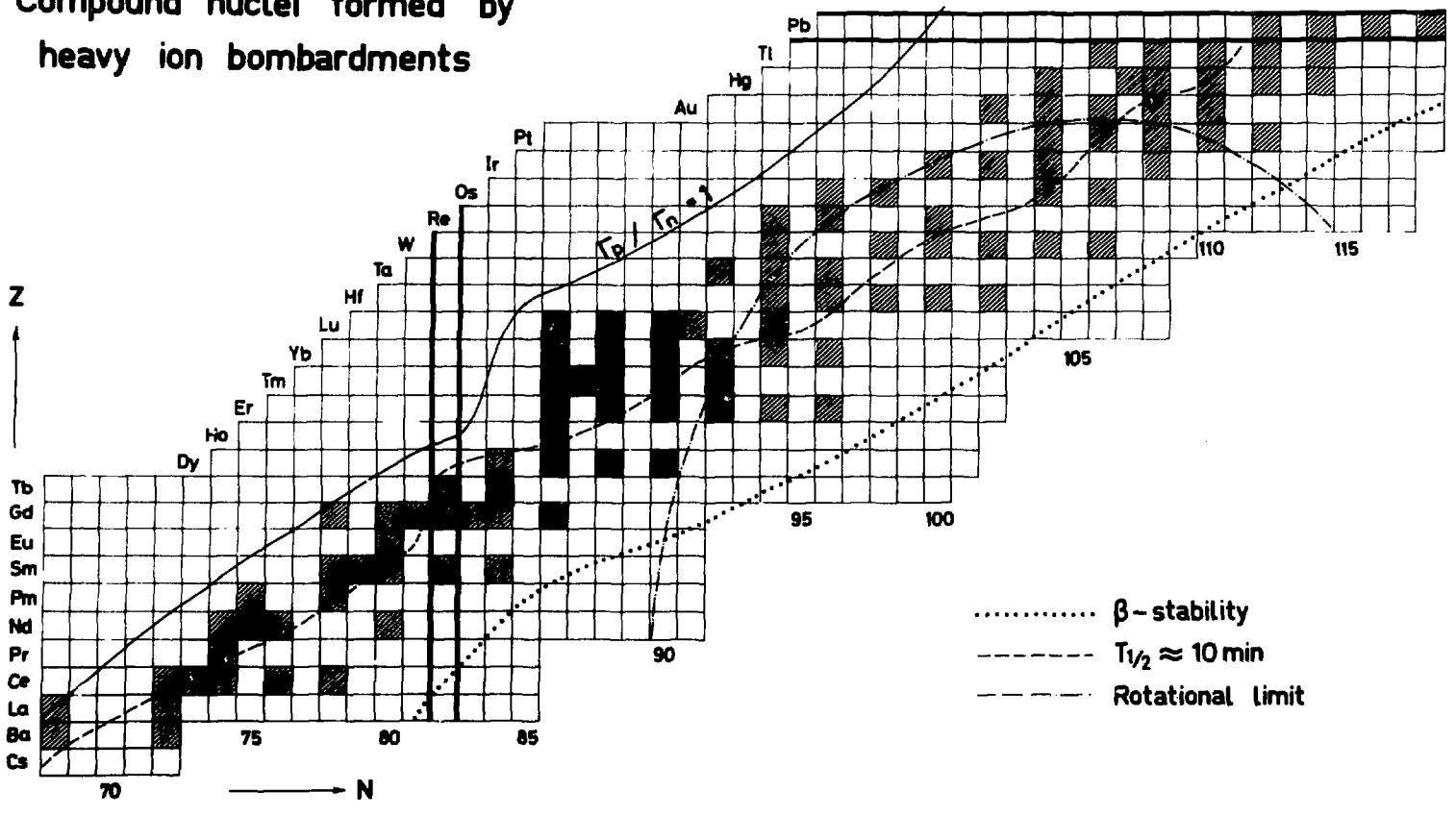
Compound nuclei formed by heavy ion bombardments
Pb
Tl
Hg
Au
Pt
Ir
Os
Re
W
Ta
Hf
Lu
Yb
Tm
Er
Ho
Dy
Tb
Gd
Eu
Sm
Pm
Nd
Pr
Ce
La
Ba
Cs
Z
N
70
75
80
85
90
95
100
105
110
115
$\Gamma_n / \Gamma_{f.s.}$
β-stability
$T_{1/2} \approx 10$ min
Rotational limit
XBL 804-9186

Fig. 23

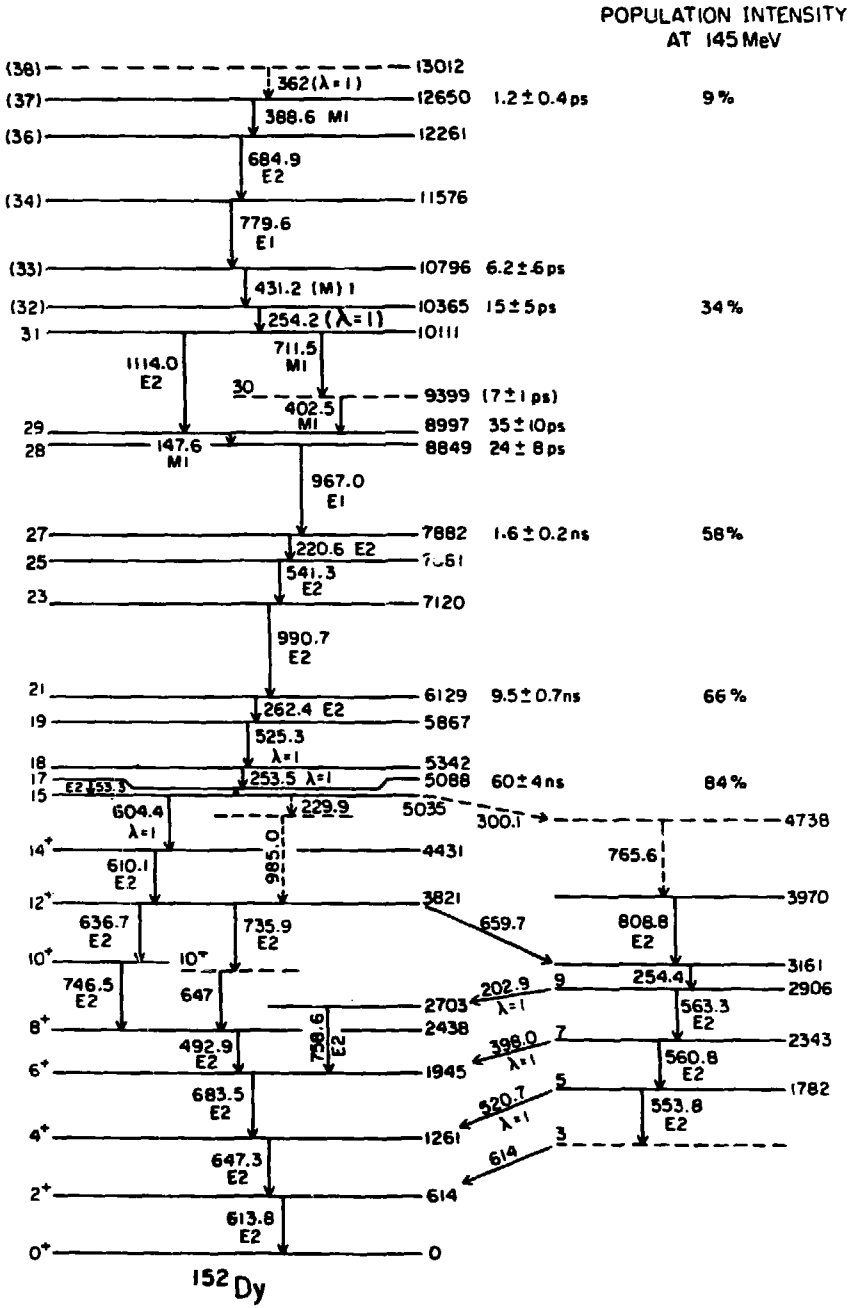

XBL 806-9887

Fig. 24

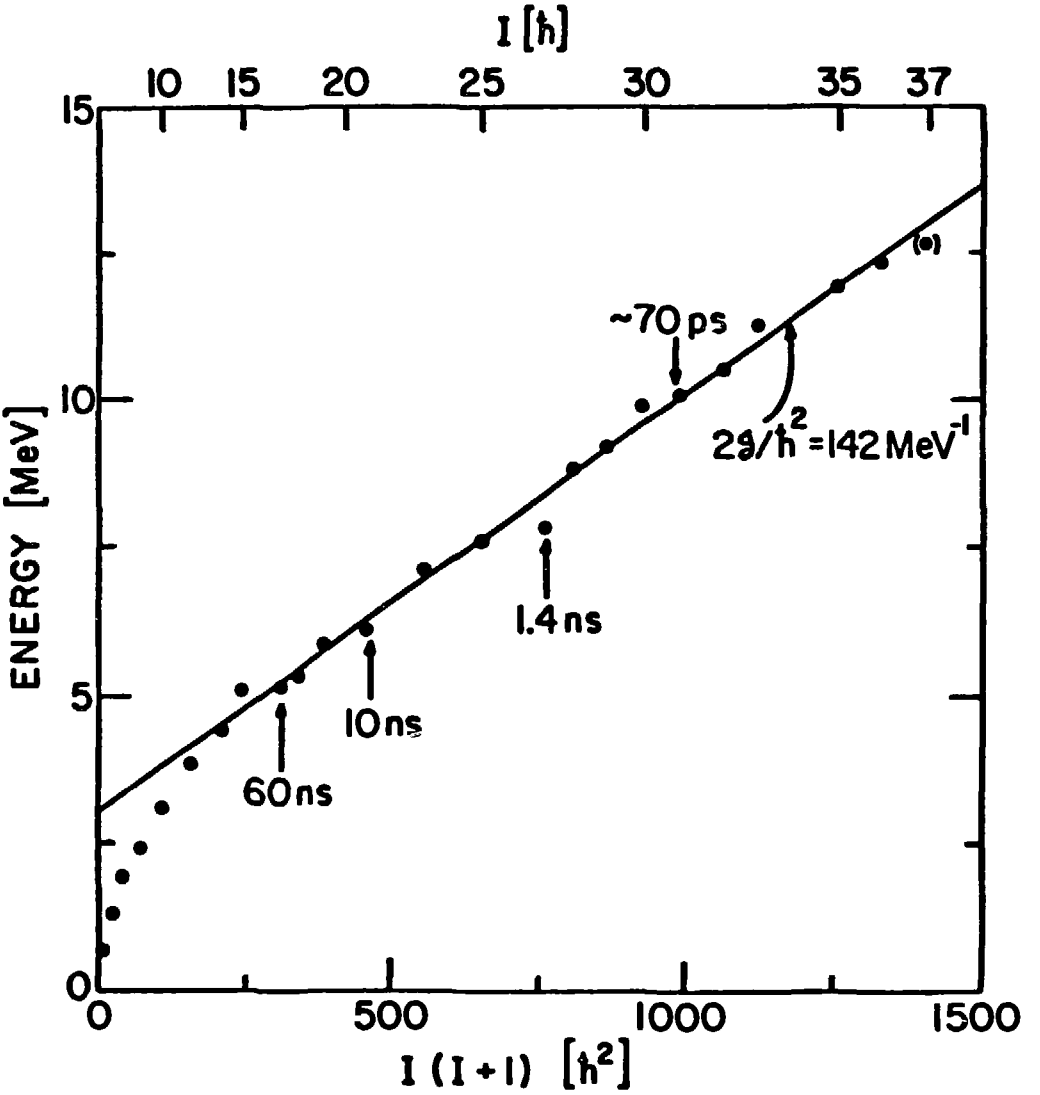
I [ħ]
10
15
20
25
30
35
37
15
10
5
0
ENERGY [MeV]
~70 ps
2ϑ/ħ²=142 MeV⁻¹
1.4 ns
10 ns
60 ns
0
500
1000
1500
I (I+1) [ħ²]
XBL 788-10388

Fig. 25

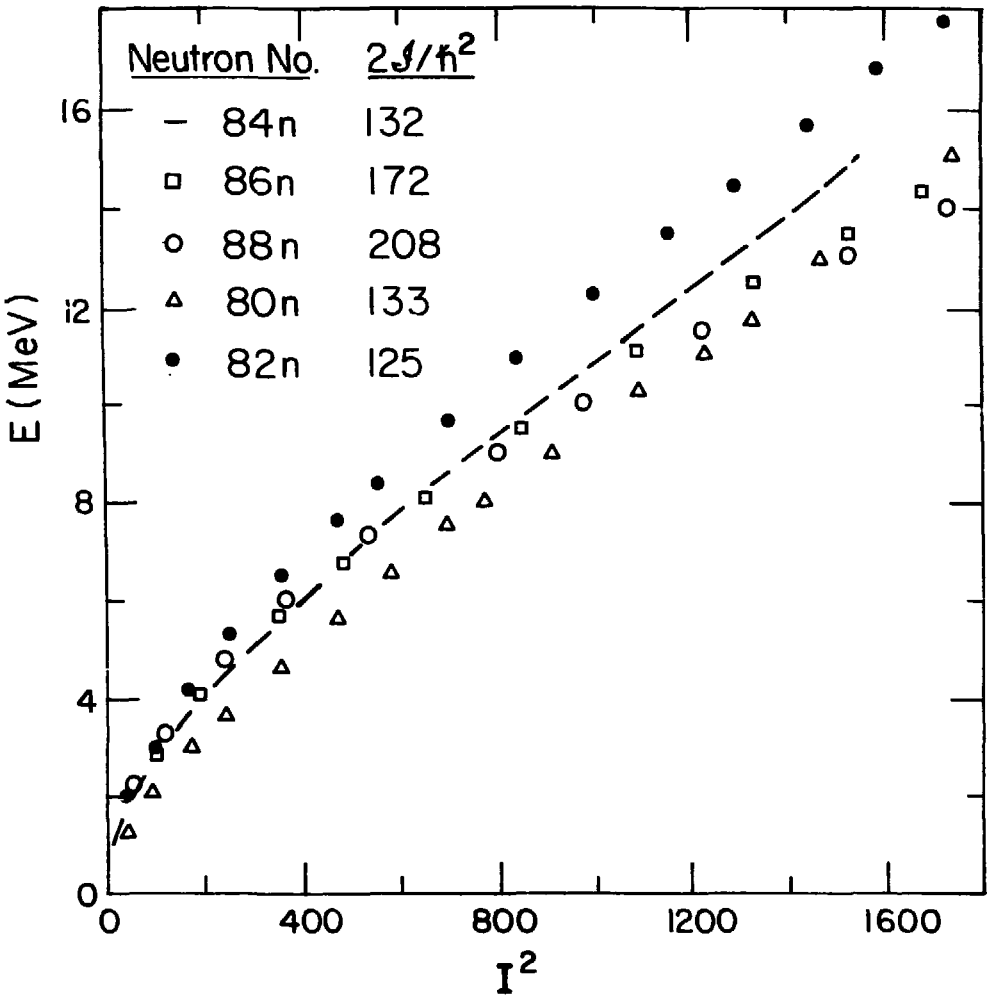

XBL 803-524

Fig. 26

$$E_I = \frac{\hbar^2}{2\mathfrak{J}} I(I+1)$$

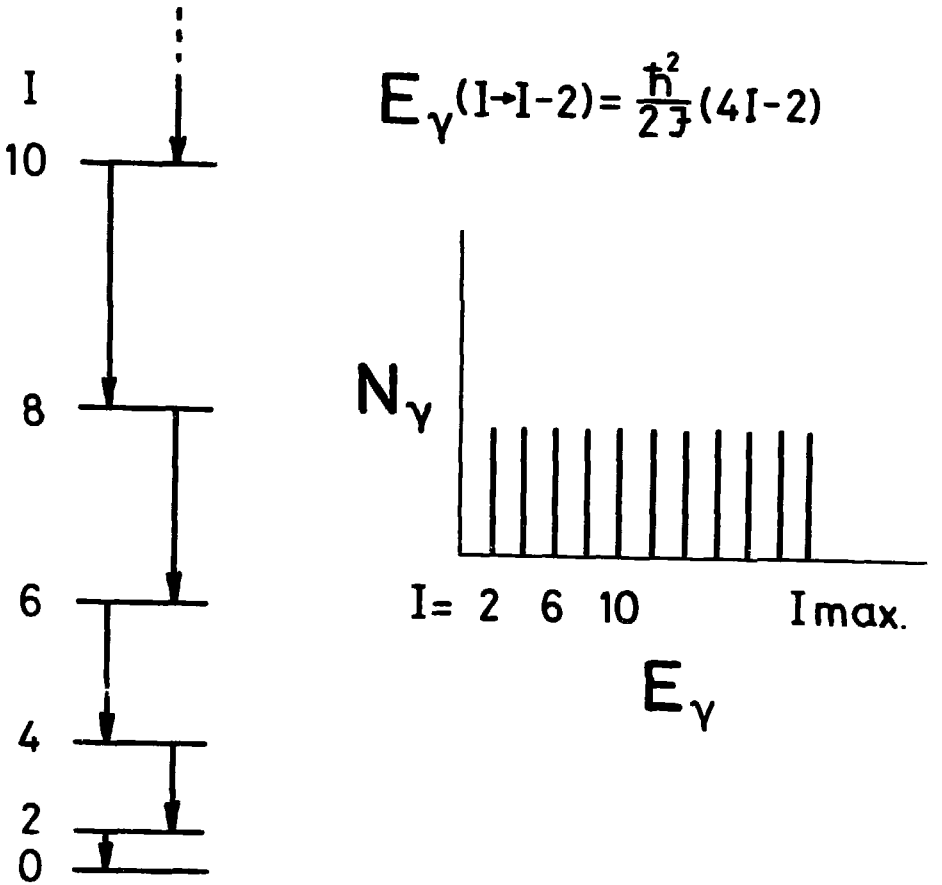

XBL 803-8762

Fig. 27

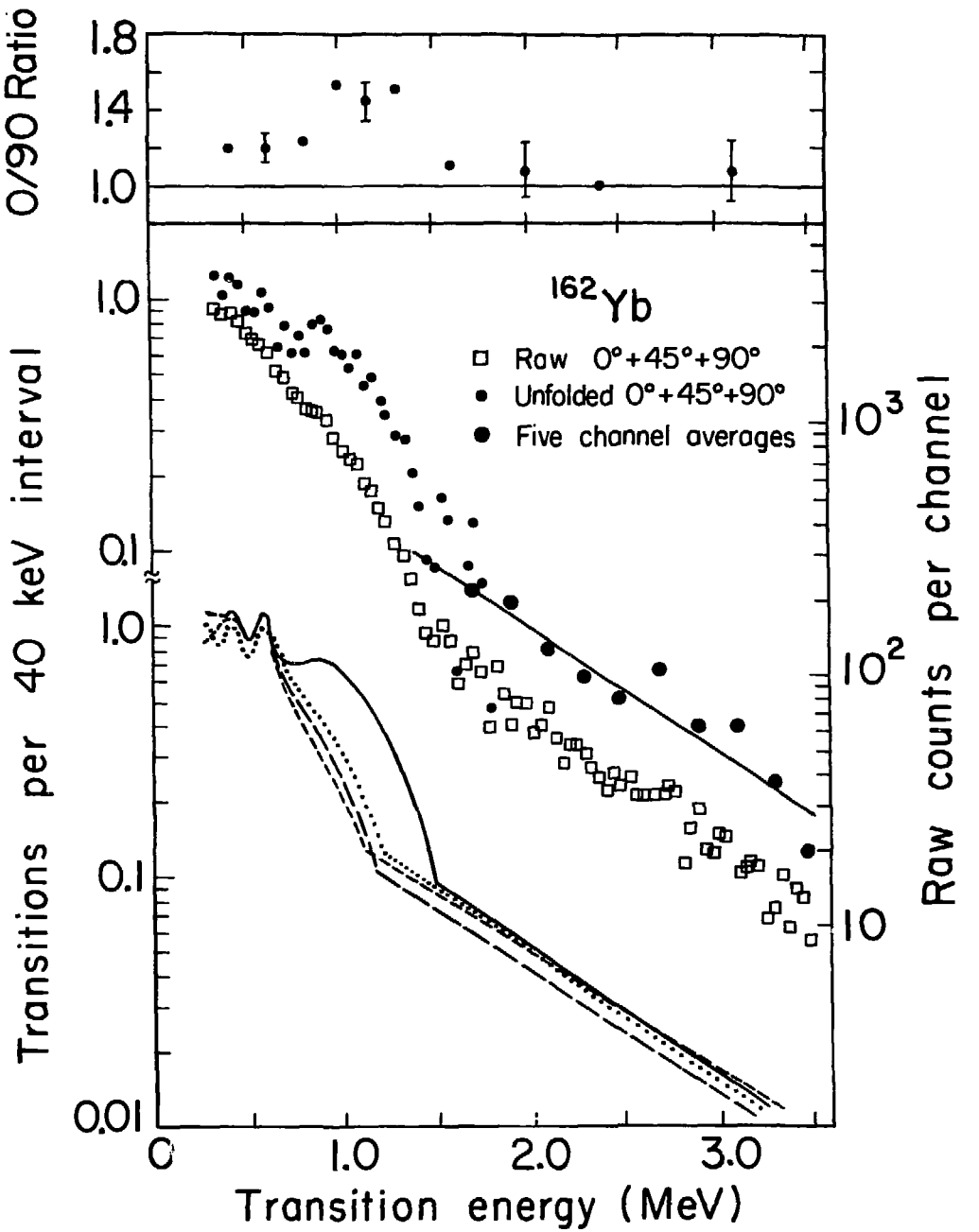

XBL 771-162A

Fig. 28

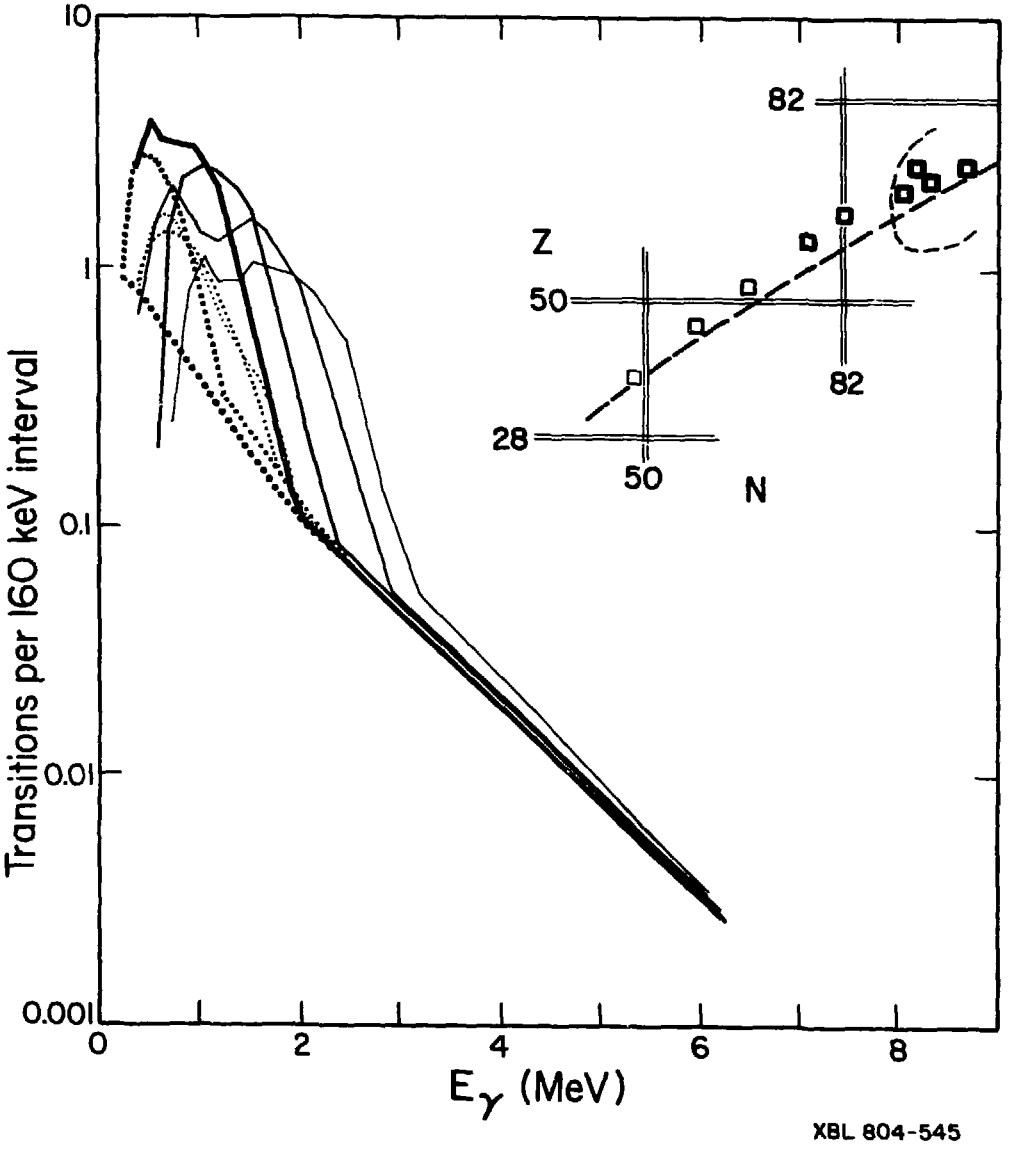
10
1
0.1
0.01
0.001
Transitions per 160 keV interval
0
2
4
6
8
E_γ (MeV)
82
Z
50
28
82
50
N
XBL 804-545

Fig. 29

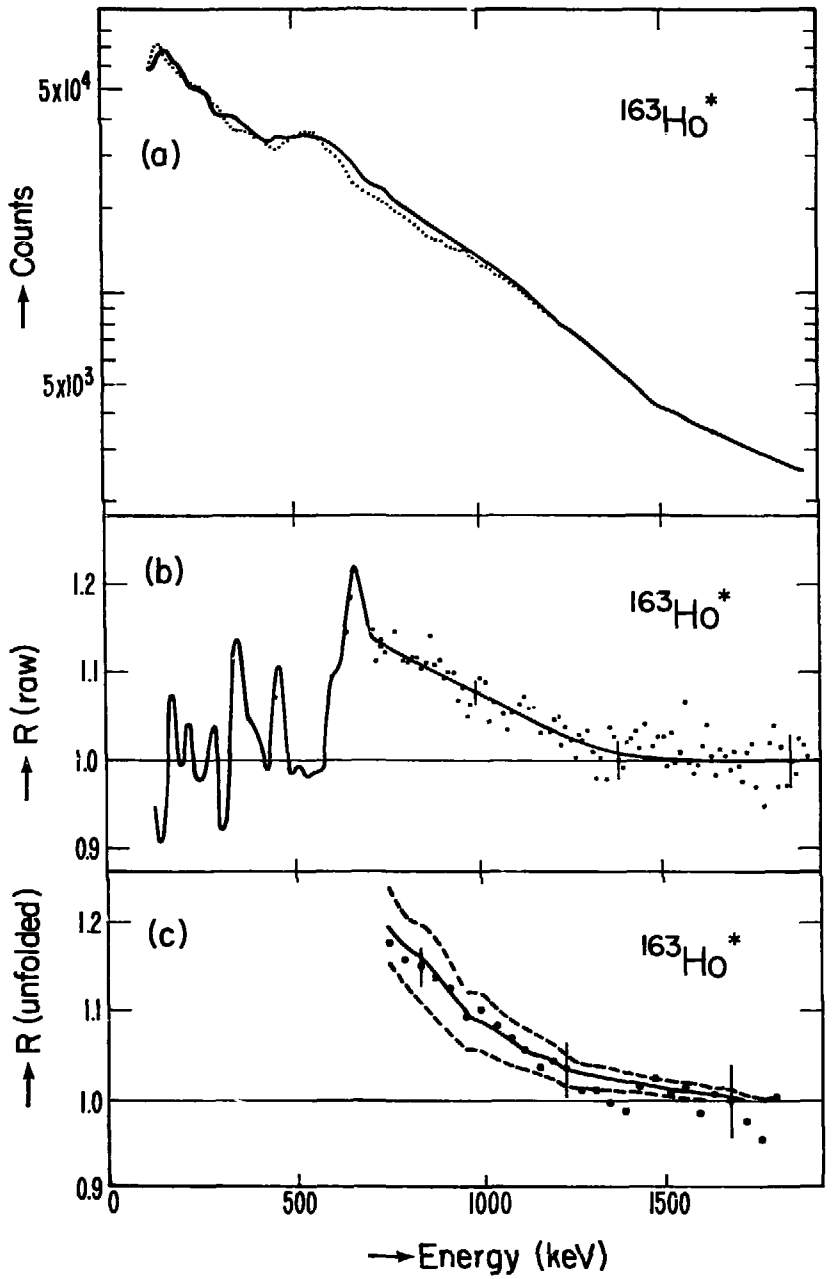

XBL 786-2560A

Fig. 30

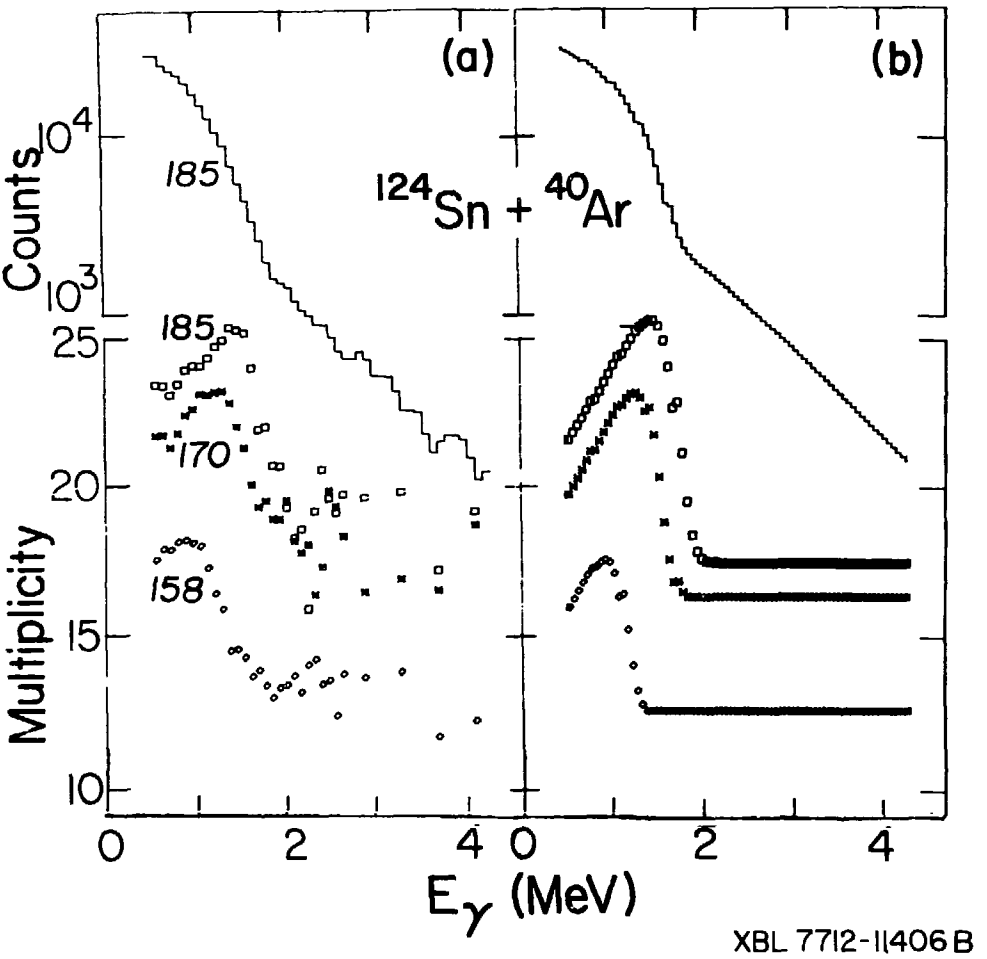
(a)
(b)
$^{124}Sn + ^{40}Ar$
Counts
10^4
10^3
185
185
170
158
Multiplicity
25
20
15
10
0
2
4
0
2
4
E_γ (MeV)
XBL 7712-11406B

Fig. 31

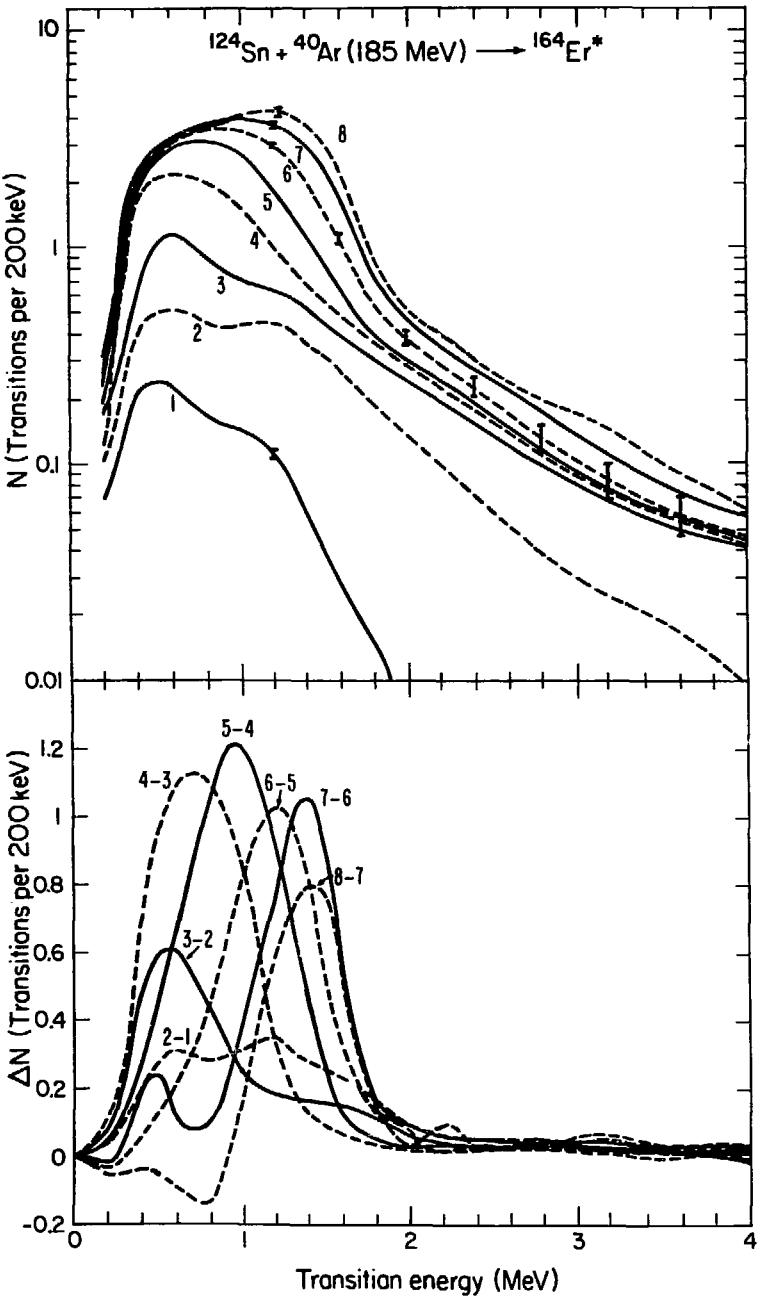

XBL 792-645A

Fig. 32

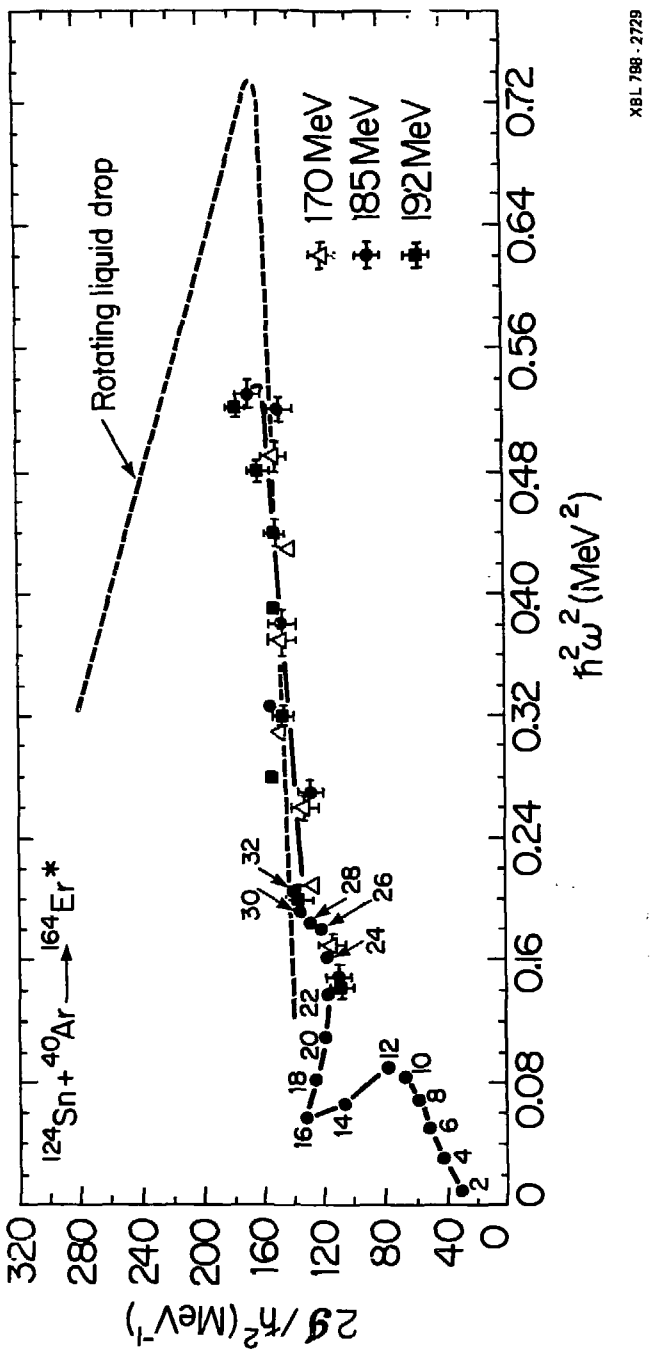

XBL 788-2729

Fig. 33

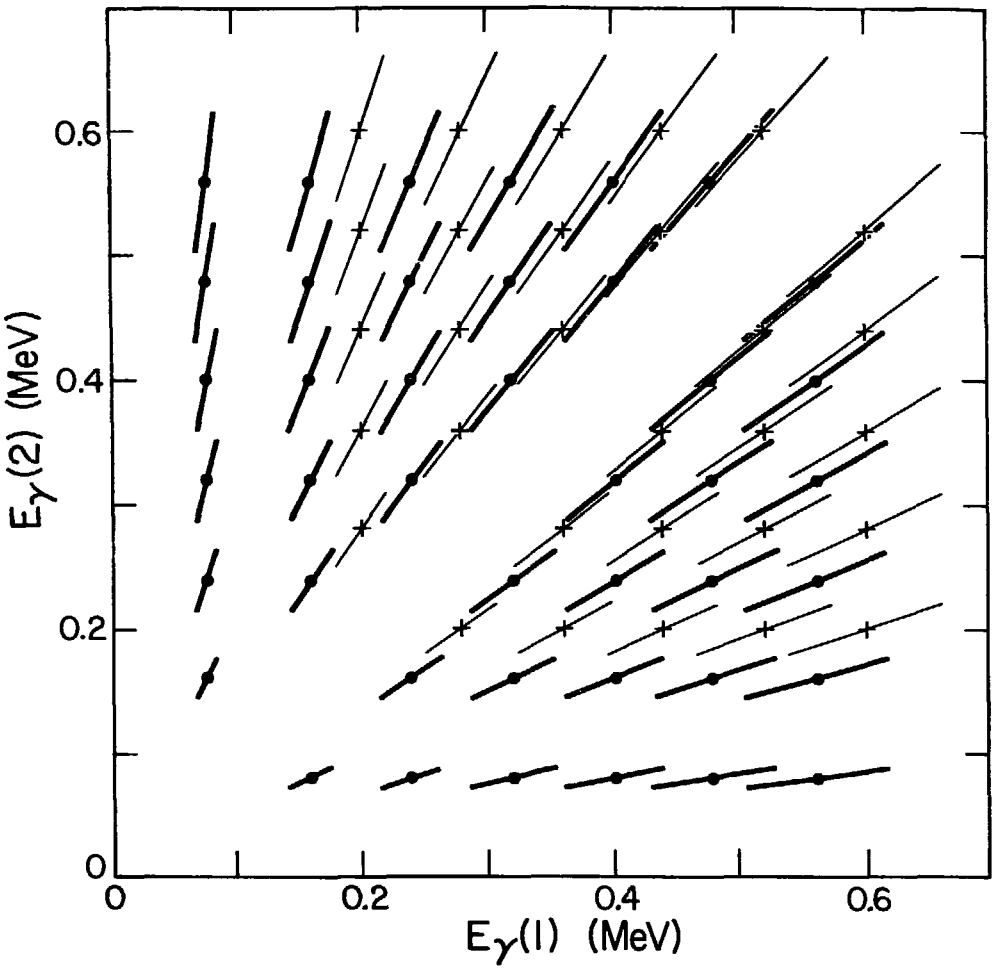

Fig. 34

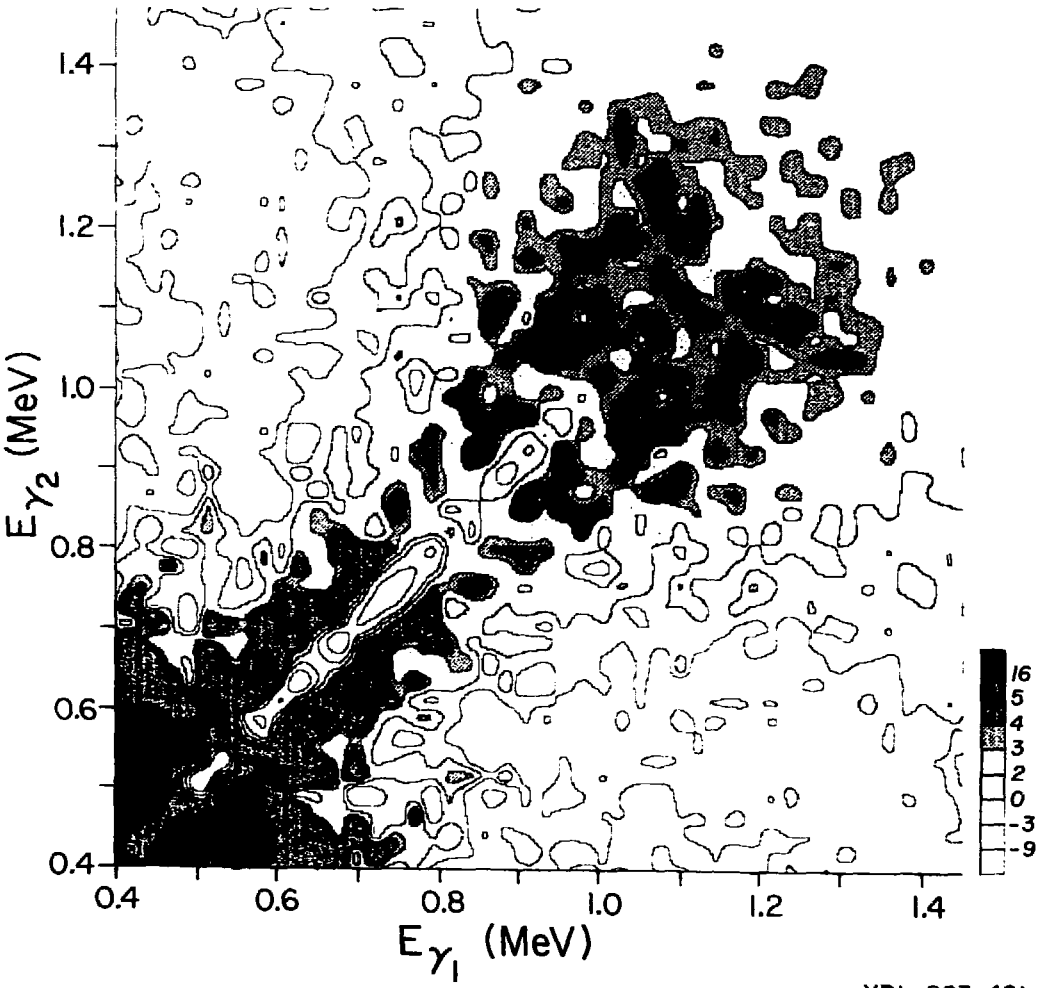
1.4
1.2
1.0
0.8
0.6
0.4
E_{γ_2} (MeV)
0.4
0.6
0.8
1.0
1.2
1.4
E_{γ_1} (MeV)
16
5
4
3
2
0
-3
-9
XBL 803-481

Fig. 35

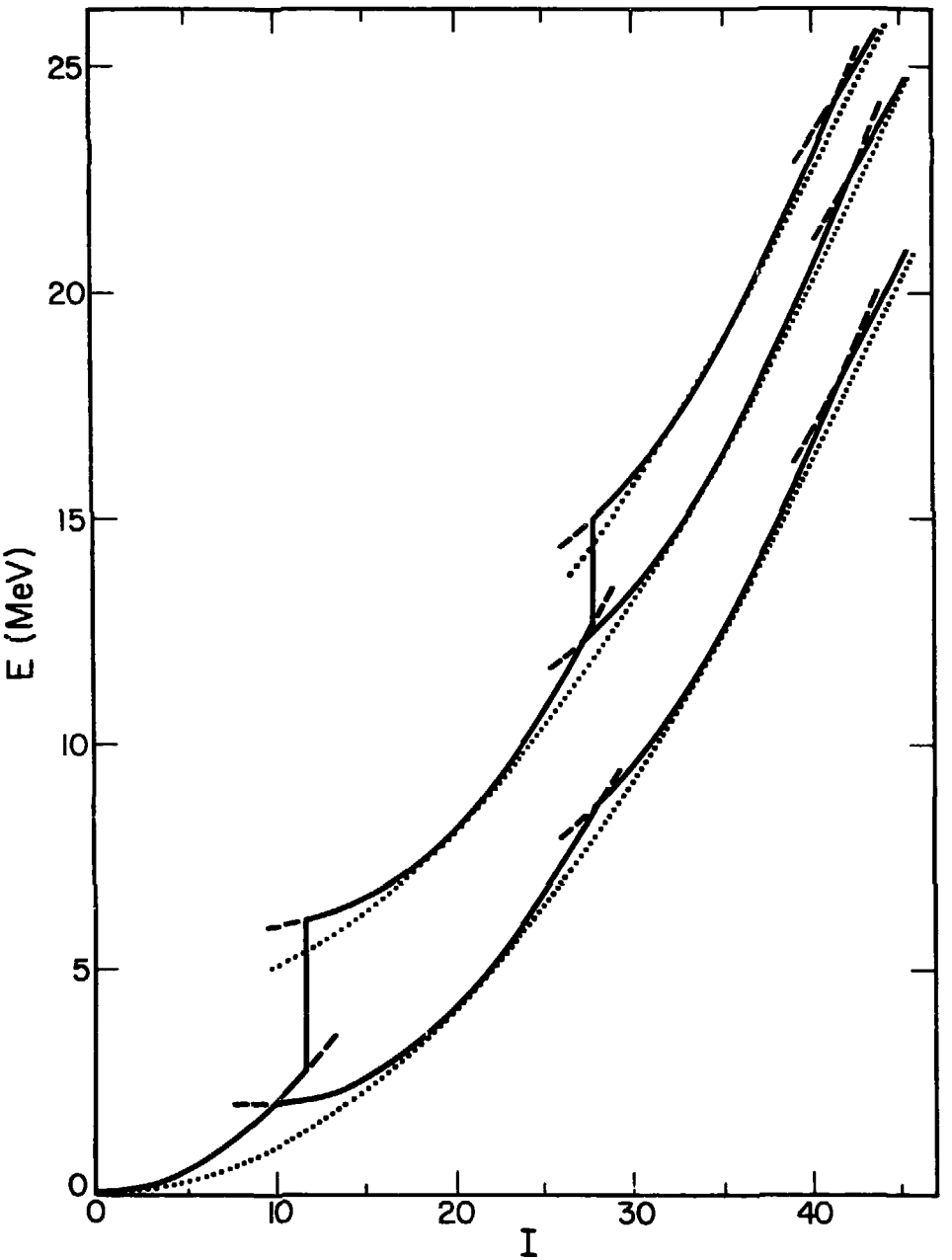

XBL 803-502

Fig. 36